INTERNATIONAL ATOMIC ENERGY AGENCY
UNITED NATIONS EDUCATIONAL, SCIENTIFIC AND CULTURAL ORGANIZATION

INTERNATIONAL CENTRE FOR THEORETICAL PHYSICS
34100 TRIESTE (ITALY) - P.O.B. 586 - MIRAMARE - STRADA COSTIERA 11 - TELEPHONE: 2240-1
CABLE: CENTRATOM - TELEX 460892-I

SMR/388 - 5

SPRING COLLEGE IN MATERIALS SCIENCE
ON
"CERAMICS AND COMPOSITE MATERIALS"
(17 April - 26 May 1989)

FIBER REINFORCED CERAMICS

Kenneth H.G. ASHBEE
Materials Science and Engineering
University of Tennessee
434 Dougherty Eng. Building
Knoxville, Tennessee 37996-2200
U.S.A.

FIBER REINFORCED CERAMICS

Trieste, 1989

PREAMBLE

"Strengthening with fibers has so many advantages - high strength, toughness, high-temperature strength, thermal stability, and cheap, light and chemically inactive materials for the fibers - that it seems certain to become the basis of engineering solids of the future. The main problems are technological. We have to develop ways of making and assembling the fibres cheaply by the ton and develop new methods of engineering design and fabrication to make best use of their properties. These developments will require great effort but the stakes are high." A. H. Cottrell, "Strong solids," Proc. Roy. Soc. A282, 2-9, (1963).

Fabrication of ceramic matrix composites involves high temprature treatment (sintering) and this introduces two complications. In some systems, Nicalon/SiC for example, a thin layer of non-crystalline material forms at the interface and effectively seals the fiber/matrix interface, thereby destroying the crack - stopping characteristics of a weakly bonded interface. Sdcondly, thermal and hence mechanical degradation of fibers usually occurs, leading to overall reduction in strength. The key to solving both problems lies in the development of fiber coatings and this, the development of fibers coatings, is the topic that I have selected for the ceramics part of my lectures.

One generic problem to be designed around with ceramic matrix composites is thermal expansion mismatch between fiber and matrix materials. This is a particularly important problem because of (a) the large temperature range through which engineering ceramics are required to cycle, and (b) the fact that very small thermal expansion mismatch leads to very large interfacial stresses.

Following the traditional practice of toughening ceramics by introducing mechanically more compliant materials, for example star into bricks and hair into pottery, attempts have been made to incoprorate metals into modern ceramics. One of the first attempts, by C. T. Forwood and A. J. Forty, Phil. Mag. 11, 1067-1071 (1965), exploited the separation of particles of gold within NaCl single crystals. The increase in toughness was found to be only marginal. This goal, of achieving toughness by making use of the higher fracture toughness of metals, has largely been abandoned in favor of the crack - stopping ability of weak interfaces with fibers more capable of high temperature performance than are the metals.

A big step forward came with the advent of Nicalon SiC continuous fiber (S. Yajima et al., Synthesis of continuous SiC fibers with high tensile strength," J. Amer. Ceram. Soc., 59, 324-327, (1976)). Synthesized from an organometallic precursor, polycarbosilane, Nicalon is an oxidation - resistant, high strength, fine - grained SiC fiber. The fiber manufacturing process begins with the dechlorination of dichlorodimethylsilane using molten metallic sodium. The dimethylpolysilane so formed is a solid polymer, and is further polymerized to polycarbosilane, purified and spun into fiber form. After exposure to ozone to promote cross-linking, the fiber is converted to silicon carbide by a sequence of heat treatments culminating at 1475-1675 K. The final overall chemical composition in wt % is Si 55, C 30, O 15. The average content of phases in wt % is typically β-SiC 60, non-crystalline SiO_2 30, non-crystalline carbon 10. The fiber density is 2.55 g cm-3.

FABRICATION OF POLYCRYSTALLINE CERAMIC COMPONENTS

The raw material from which conventional monolithic ceramics are fabricated is usually in the form of powder. Initial consolidation may be by simply packing the powder into a mold, by extruding an aqueous slurry or mixture of powder and organic binder, or by cold - pressing a compact. Sintering at elevated temperature may be with or without application of pressure.

In the case of fiber reinforced ceramics, the fibers and ceramic powder must first be blended together. If the fibers are short lengths, whiskers for example, adequate mixing may be achieved by tumbling. Continuous yarns and woven fabric can be impregnated with the ceramic powder by traversing through a slurry to produce a pre - preg tape or sheet. Pre - preg tape lends itself to filament winding, and pre - preg sheet to laminate stacking. In both cases, final consolidation and densification is achieved by hot pressing or hot isostatic pressing (HIP). Hot pressing is not without its problems, particularly in respect of inflicting mechanical damage at compressive contacts between fibers.

Continuous fiber reinforced ceramics are best fabricated by chemical vapor infiltration of a fiber preform. Although slow, chemcial vapor deposition (CVD) of solid material onto fibers in order to build up a matrix can be accomplished at relatively low temperatures, and it makes for a relatively stress - free composite. The vapor is usually an organic substance and several methods of infiltration are available, including (i) isothermal, (ii) temperature - gradient, (iii) pressure - gradient and (iv) forced - flow, thermal gradient permeation. Since it represents "state of the art" technology, the latter process is described below for a composite having as matrix material a ceramic with good thermal conductivity, specifically SiC.

The fiber preform is assembled inside a graphite holder, water-cooled around its sides and base as shown in Figure 1. The upper surface of the preform is located inside a furnace, and the reactant gas (usually a mixture of gases) is force-flowed through the base of the holder into the cold, unreactive lower part of the preform. When it reaches the hot zone, the gas decomposes and solid material is deposited onto the fibers hereabouts. Deposition progressively densifies and raises the thermal conductivity of the composite, causing the hot zone to move towards the cold zone. Eventually, the upper regions become impervious, the exiting gas changes from flowing vertically to flowing radially and is forced to find its way between the composite and the holder to the vents in the roof of the latter. For Nicalon fabric reinforced SiC, processing times of 18 to 24 hours, densities higher than 90% theoretical density and room temperature flexure strengths approaching 600 Mn m^{-2} have been reported.

ORIGINS OF TOUGHNESS

Experimentally, it is found that incorporation of fibers into ceramics increases the strain to failure. The onset of matrix cracking manifests itself by acoustic emission long before departure from linearity in the stress versus strain relationship and this, in turn, occurs long before overall failure of the composite.

Frictional resistance to fiber pull-out is reckoned to be an important source of toughness, and several methods have been devised to measure it. D. B. Marshall (J. Amer. Ceram. Soc., C259-260, (1984)) uses a microhardness indentor to displace individual fibers oriented perpendicular to a thin slab of composite. The normal force,

deduced from the hardness indentation left in the fiber, is

$$F = 2\pi Rt\tau$$

where τ is the frictional stress, t is the thickness of the slab and R is the fiber radius, and the frictional stress is

$$\tau = F^2/40\ uR^3E$$

where E is Young's modulus for the fiber material, and u is the fiber displacement. Using this method on surface-treated Nicalon/SiC composites, R. A. Lowden (M.S. thesis, University of Tennessee, 1988) finds values for τ at room temperature in the range 1-100 MN m-2.

The interfacial frictional stress between fiber and coating has also been measured by R. A. Lowden (M. S. thesis, University of Tennessee, (1988)) by vapor depositing a uniform length of coating in the central region of a single fiber, gripping the uncoated ends and tensile testing the fiber until segmentation of the coating by circumferential cracking ceases. This is illustrated in Figure 2. He then uses Aveston and Kelly's formula for the critical length of fiber in a creeping matrix, page 25 of composites notes, to estimate £.

Typical results for Nicalon fibers are τ~ 40 Mnm-2.

In all of these methods, interfacial stresses arising from Poisson contraction are ignored. Ceramics as a class of materials are characterized by having small values for Poisson's ration (~¼). Hence we are concerned with the difference between two small numbers, i.e. a small number, when considering Poisson contraction in ceramic matrix composites.

FIBER SURFACE COATINGS

Auger analysis of Nicalon fibers heated in argon reveals the presence of a surface film containing silicon and oxygen, Figure 3. In Nicalon/SiC composites, this film strongly bonds the fiber/matrix interface, with the result that the composite is no tougher than unreinforced SiC. Worse still, SIMS anlaysis of fibers extracted from Nicalon/SiC composites manufactured by methyltrichlorosilane vapor deposition processes, reveals that chlorine, presumably picked up from the precursor vapor, is concentrated in the surface layers. Chemical attack of the fiber by chlorides derived from the matrix vapor deposition process is another potentially embrittling mechanism.

To insulate Nicalon fiber from vapor deposited SiC, and thereby avoid both mechanical continuity attributed to the silicon- and oxygen- containing surface film and chemical attack by chlorine from the matrix precursor, it is advantageous to coat the fiber with pyrolytic carbon (Butler et al., J. Adhesion, 5, 161-178, (1973)). This practice, of carbon coating fibers with which to reinforce ceramics, has been widely used. There are several methods available, including pyrolysis of resin binders used to assemble fiber preforms, and thermal decomposition of organic material, usually methane since it contains no chlorine, introduced into the preform by vapor infiltration. The main limitations of pyrolytic carbon coatings are poor oxidation resistance and a tendency to over-lubricate the interface.

Other fiber coatings that have been experimented with include elemental silicon, silicon carbide, elemental boron, and boron nitride. In principal, silicon on Nicalon fibers should serve two useful purposes. It should interact with excess carbon and thereby prevent the formation and outgassing of carbon monoxide during high temperature service. It should also promote glass - forming reactions and hence provide for viscous flow and blunting at crack nuclei. Silicon carbide is conveniently deposited chlorine-free from a mixture of methylsilane and argon at 975 - 1275 K but, to date, has not yielded substantial improvements in mechanical properties. Elemental boron can be deposited from diborane/argon mixtures at 775 K. The glass-forming characteristics of boron make it an attractive candidate for the reasons outlined above for silicon. Boron nitride coatings have met with limited success in SiC fiber/zirconia and zirconium titanate matrix compoistes (B. Bender et al., Bull. Amer. Ceram. Soc., 65, 363-369, (1986)). Boron nitride coatings have been successfully deposited on Nicalon fibers using a diborane/ammonia mixture. The main problem with boron nitride is that it oxidizes at high temperature.

Nickel-coated carbon fiber has been available for a number of years and has been successfully incorporated into metal matrix composites. Attempts have been made to extend this technology to manufacture metal-coated fibers for use in ceramic systems, and here we cite the coating of Nicalon fiber with molybdenum by decomposition of molybdenum hexafluoride.

In all of this, what we most want to know is how weak or strong the interfacial region needs to be for optimum properties. Elastically soft coatings lead to radial compression at the interface whereas elastically stiff coatings lead to radial tension; the latter can be sufficiently large to cause interfacial debonding. This reasoning appears to indicate that stiff, and not soft coatings best serve the quest for crack arrest at fiber interfaces.

The immediate future will see the emergence of a reliable database for the tensile properties of ceramics and ceramic matrix composites. This will require the refinement of tensile testing techniques. Compared with more conventional engineering materials, the tensile properties of ceramics are far more sensitive to experimental variables such as surface perfection and test-piece alignment. In respect of the latter, ultra fine self-alignment, achieved through hydraulic displacement of a ring of pistons carried by the tensile grip and in contact with the connecting rod of the mechanical testing machine, is rapidly gaining in popularity. Further development of high temperature techniques to replace the strain gage technology used to measure displacement in tensile testing at more modest temperature, is also needed.

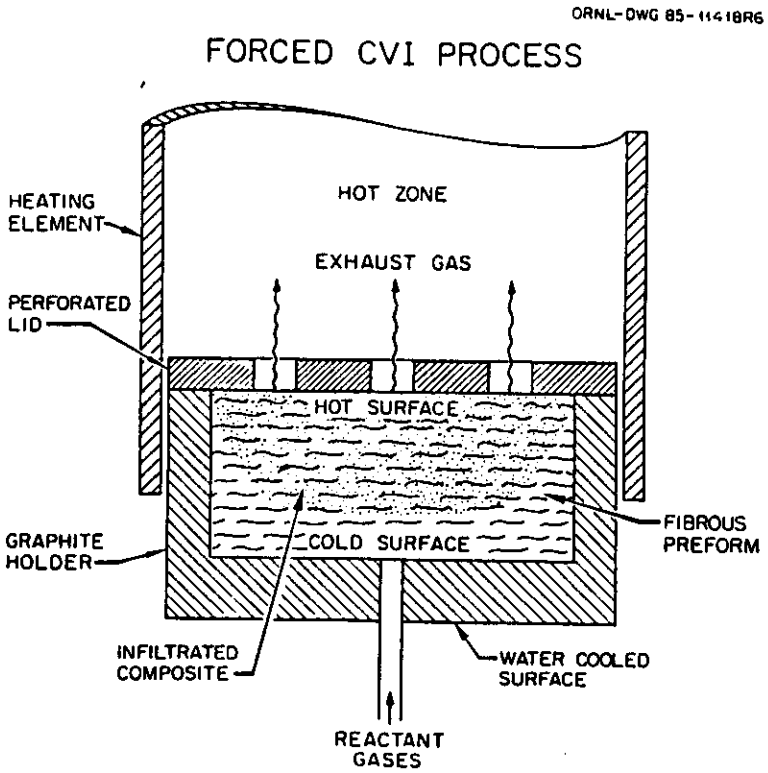

Figure 1

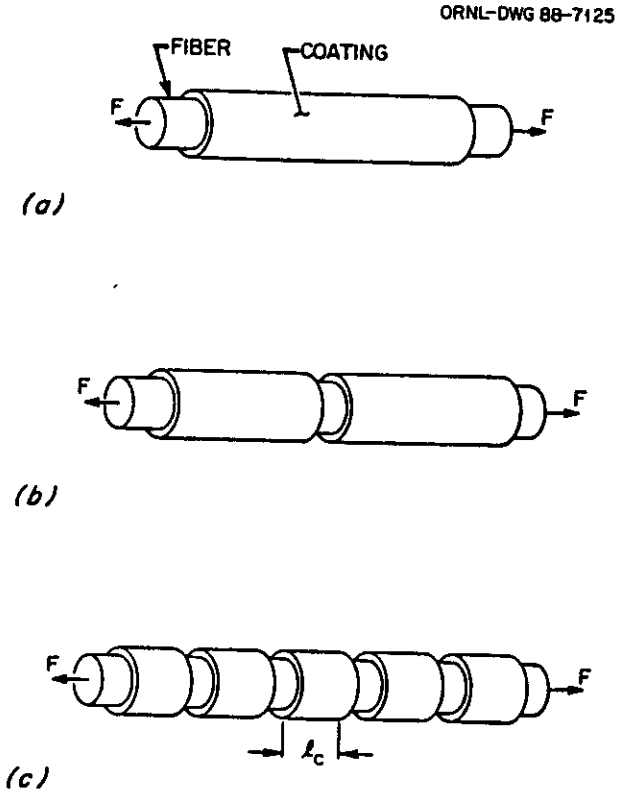

Figure 2

ELEMENT PROFILES BY AUGER ELECTRON SPECTROSCOPY INDICATE THAT THE SURFACE FILM IS PRIMARILY COMPOSED OF SILICON AND OXYGEN

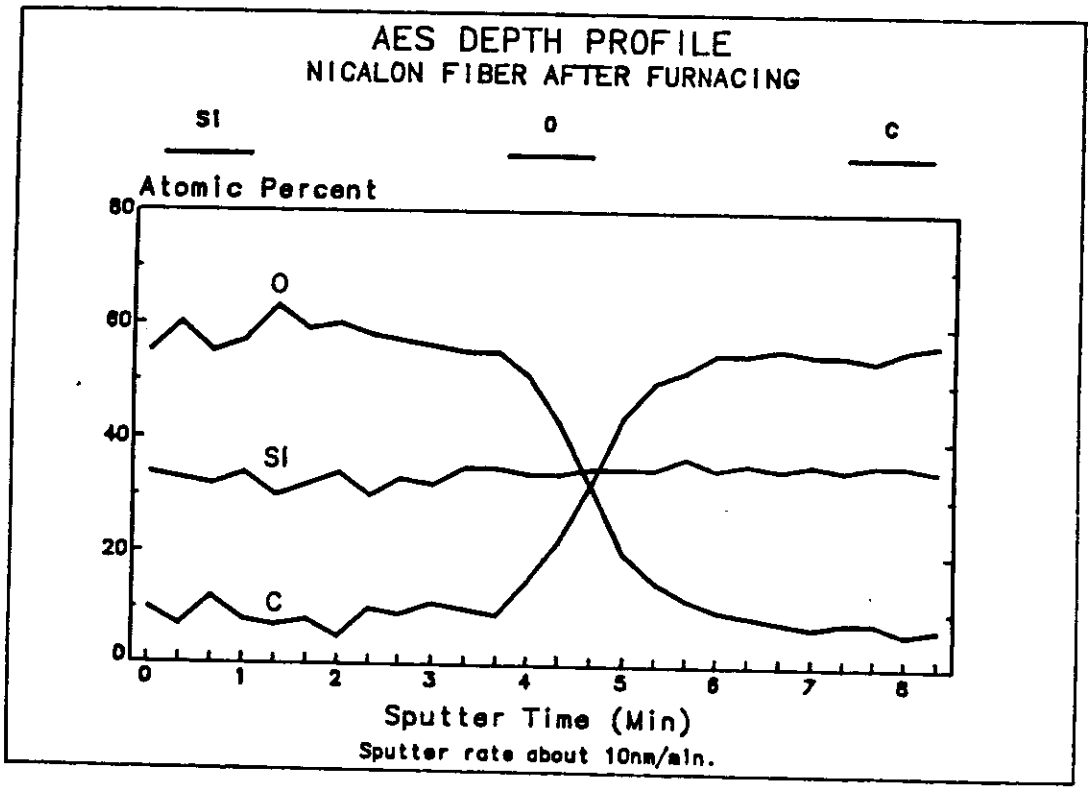

Figure 3

Specific modulus and specific strength

Young's modulus: density

$$\frac{E(Nm^{-2})}{\varrho(kgm^{-3})}$$

longitudinal velocity of sound

$$\sqrt{\frac{E}{\varrho}}$$

specific modulus

UTS: weight

$$\frac{UTS(Nm^{-2})}{\varrho(kgm^{-3})g(ms^{-1})} = L_m$$

suspended length

L_m

1

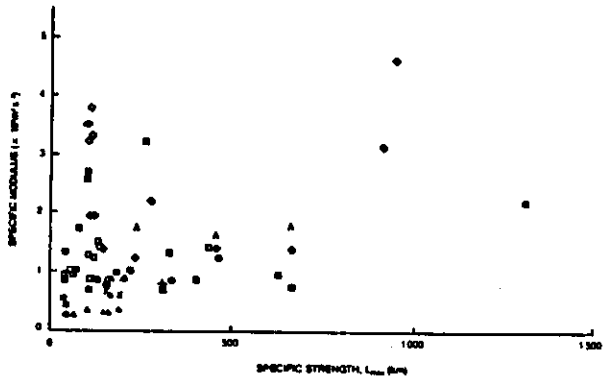

Figure 1.1. Specific modulus (velocity²) versus specific strength (L_{max}) for several fibers. For comparison, data points for some more conventional materials are also included. □ – SiC + – silicon – Si_3N_4 . . – Kevlar, X – nextel, ■ – fiberfrax, ▲ – glass, ◇ – carbon, ◆ – BeO, A – boron, ⊡ – AlN, • – alumina, ⬬ – beryllium, ● – iron. Figure compiled by S. M. Joslin.

arrangement of atoms more important than bonding in determining strength

Fiber diameters

~ 10μm

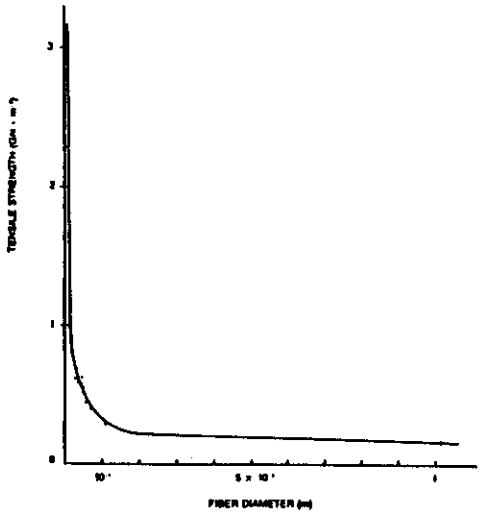

Figure 1.4. Strength of glass fibers. Data points taken from Table V of A. A. Griffith [7].

size effect in glass

carbon fiber

rayon

polyacrilonitrile PAN

pitch

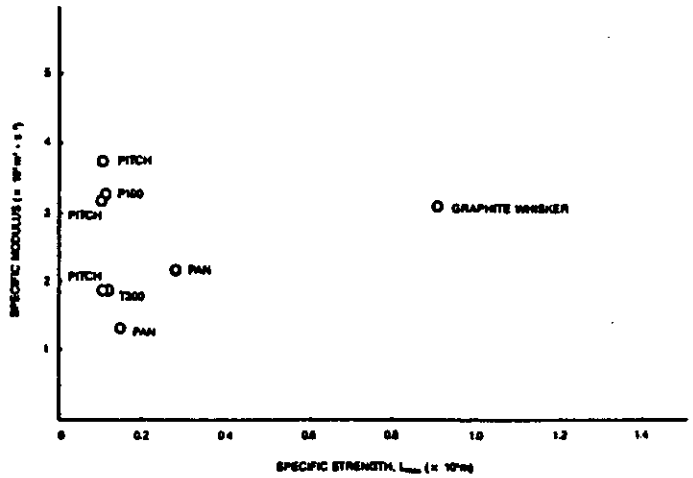

Figure 1.5. Specific modulus versus specific strength for different carbon fibers. Data compiled by S. M. Joslin.

ighly oriented polymer fibers

olyethylene

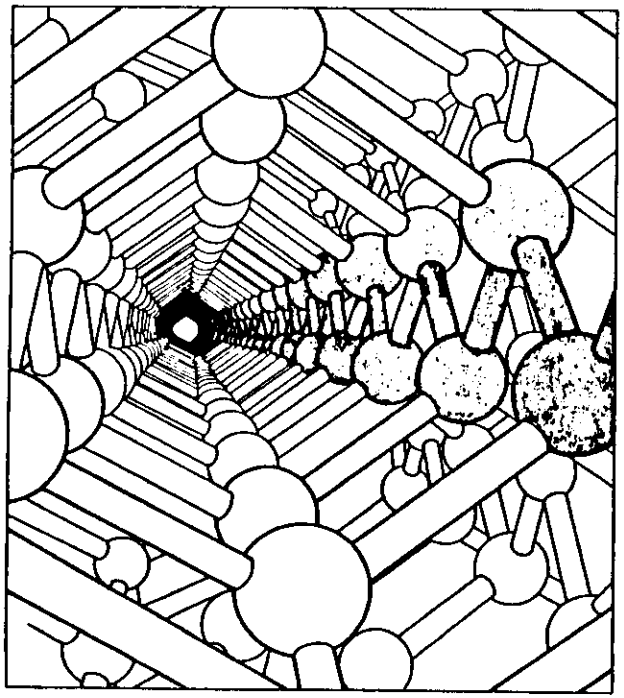

Figure 1.6. Diamond structure viewed along [110]. After L. Pauling and R. Hayward, *The Architecture of Molecules*, W. H. Freeman, San Francisco (1964).

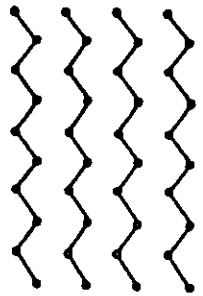

Figure 1.7. Crystal structure of polyethylene (CH_3-CH_2-). General view showing zig-zag chains of carbon atoms. After C. W. Bunn, "The Crystal Structure of Long-Chain Normal Paraffin Hydrocarbons. The 'shape' of the $>CH_2$ group," *Trans. Faraday Soc.*, 35:428–491 (1939).

cold drawn

extruded

spun

aramid fiber ropes

ceramic whiskers

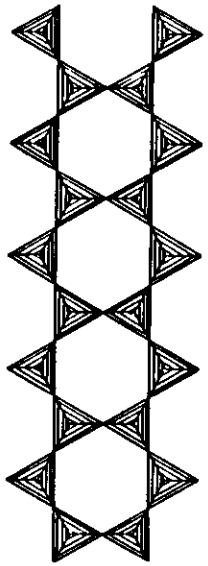

Figure 1.8. Two-dimensional chain structure of corner-sharing $[SiO_4]^{4-}$ tetrahedra.

asbestos

silicon carbide

sapphire

Fiber loadings (viz. fiber volume fractions)

close packing of identical parallel cylinders

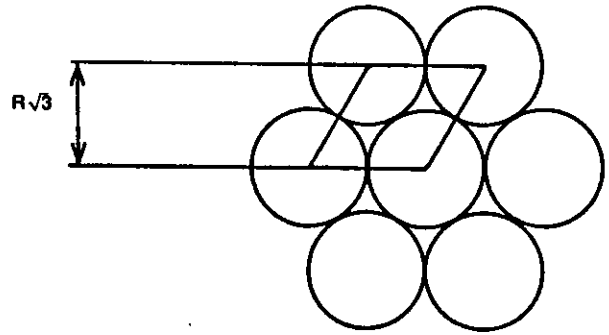

Figure 1.9.

$$\eta = \frac{\pi}{2\sqrt{3}}$$

$$= 0.9069$$

Law of mixtures for modulus of uniaxial composites

$$E_l = E_{fiber}\,\eta + E_{matrix}\,(1 - \eta)$$

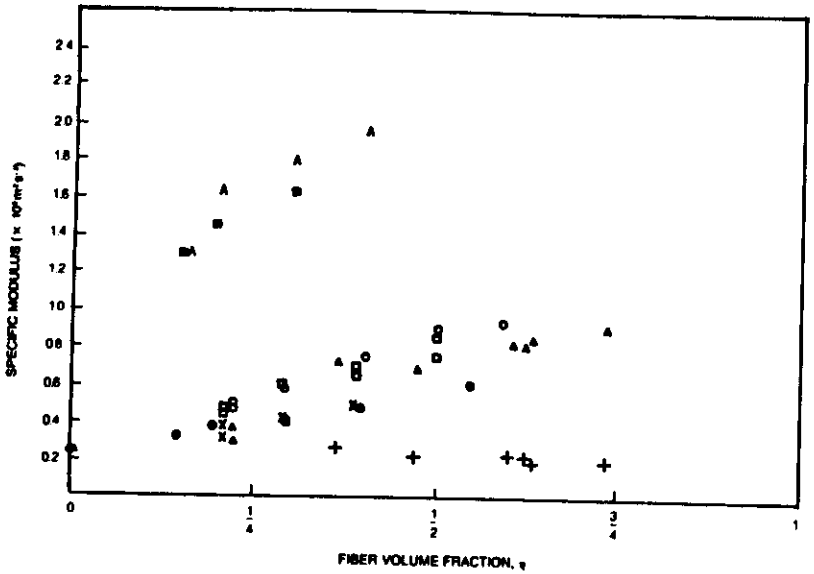

Figure 1.10. Rule of mixtures relationships between axial specific modulus and fiber volume fraction (η) for uniaxial composites. □ – B-aluminum, X – SiC(p)-aluminum, △ – graphite-epoxy, + – W–aluminum, ○ – C-glass, ▲ SiC(w)-aluminum, ● – SiC-tungsten, ■ – graphite-aluminum, ▲ – graphite-magnesium. Figure compiled by S. M. Joslin.

modulus advantage of metal matrix

eryllium

luminum–lithium alloys

must exploit anisotropy

stresses ↑ as $\frac{E}{\varrho}$ ↑

frequencies ↑ as $\sqrt{\frac{E}{\varrho}}$ ↑

beware of low thru thickness modulus

submarine hulls

thin laminate/honeycomb core sandwich structures

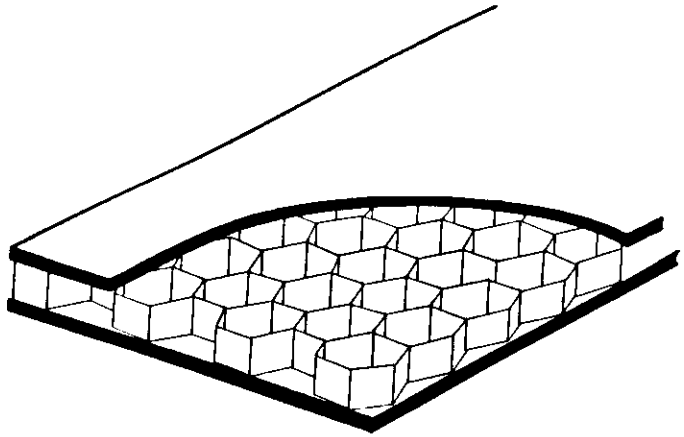

Figure 1.11. The construction of a honeycomb laminate.

effect of voids on modulus

$$x_{\text{effective}} = x(1 - 3V)$$

$$\mu_{\text{effective}} = \mu(1 - 2V)$$

Flywheels

$$\frac{J}{m^3} = \frac{Nm}{m^3} = \frac{N}{m^2}$$

ultracentrifuge

annular reinforcement versus radial reinforcement

$$\sigma = \varrho v^2$$

Composite masts—how high can a tree grow?

$$l < \pi \sqrt{\frac{EAk^2}{W}}$$

Automobile driveshafts

$$f = \frac{n \sqrt{\frac{E}{\varrho}}}{2l}$$

deflection of a beam in weightless environment

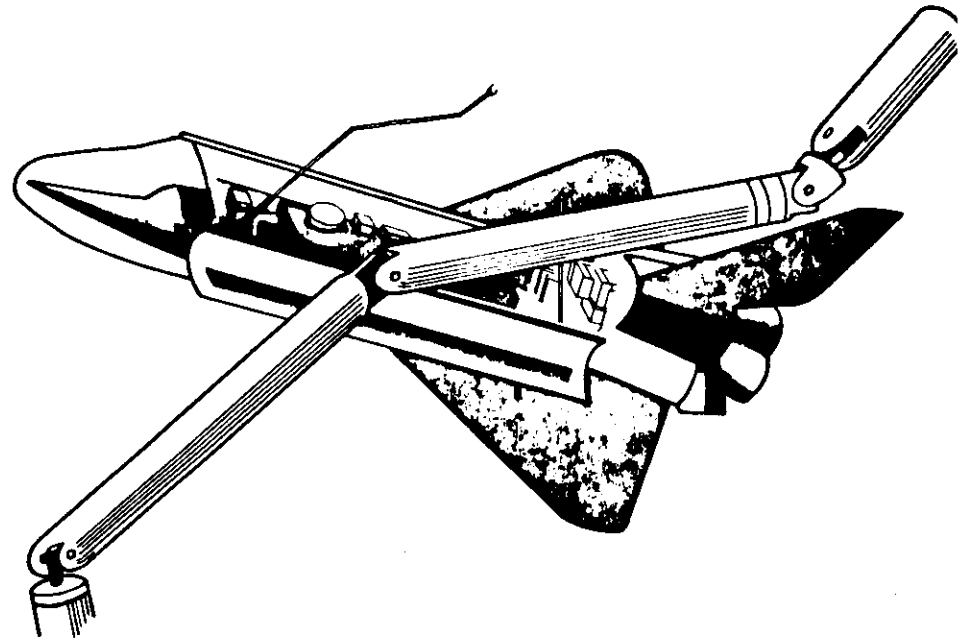

Figure 6.11. NASA's space shuttle manipulator arm.

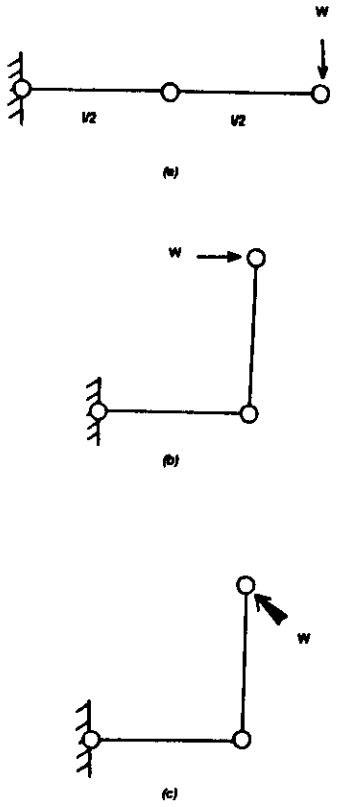

Figure 6.12. Deployment of the space shuttle manipulator arm. (a) Arms fully extended. Both arms loaded in bending. (b) Forearm at right angles to upper arm. Both arms loaded in bending. (c) Forearm at right angles to upper arm. Forearm loaded in bending, upper arm loaded in torsion.

$$\frac{\delta_{\text{on Earth}}}{\delta_{\text{in space}}} = \frac{3}{8}$$

Pre-pregs

resin flow rate versus time

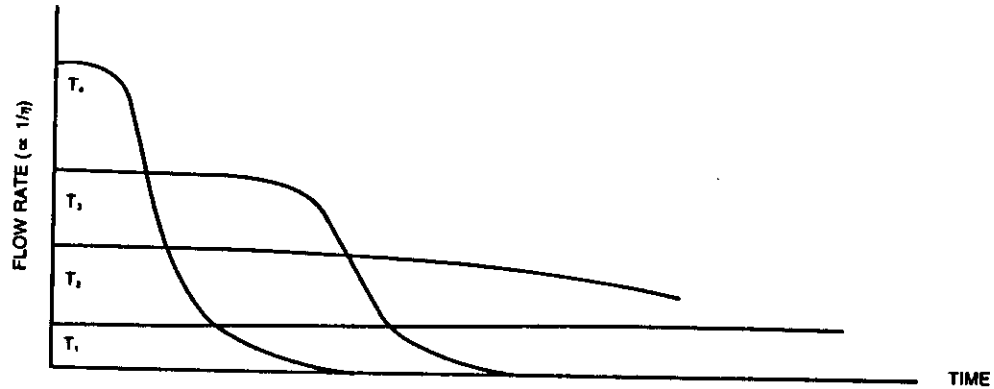

Figure 2.7. Isothermal flow rate curves for resin drainage during prepreg manufacture. $T_1 > T_2 > T_3 > T_4$.

$$\int \frac{1}{\eta}\, dt$$

liquid infiltration

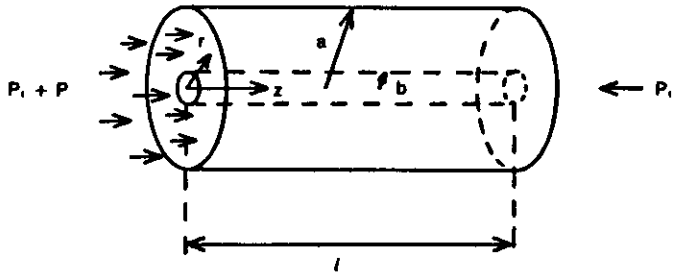

Figure 2.16.

Poiseulle flow

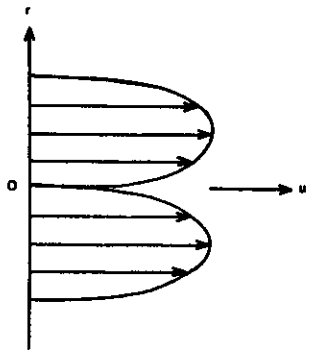

Figure 2.17. Distribution of velocity of liquid flowing through a channel that contains a stationary fiber along its axis.

$$\frac{\pi P}{8\eta l}$$

Powder preforms

Hand lay-up

Spray-up

Press molding

film stacking

Vacuum bag

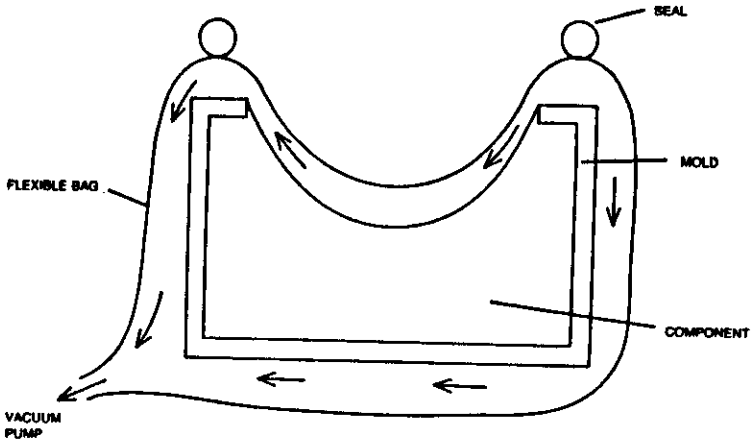

Figure 2.8. Vacuum bag molding.

utoclave

sin transfer (viz. liquid molding)

Filament winding

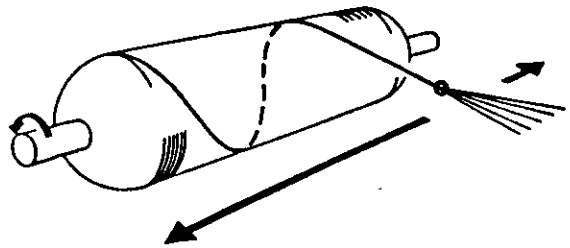

Figure 2.9. Helical (lathe-type) filament winder.

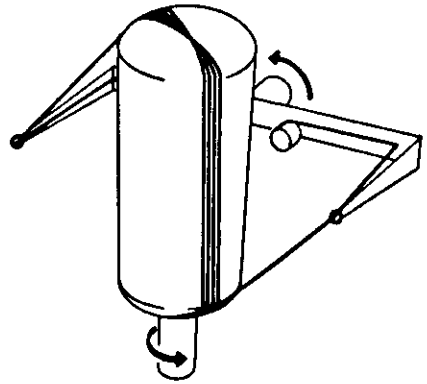

Figure 2.10. Polar (whirling arm) filament winder.

geodesic paths

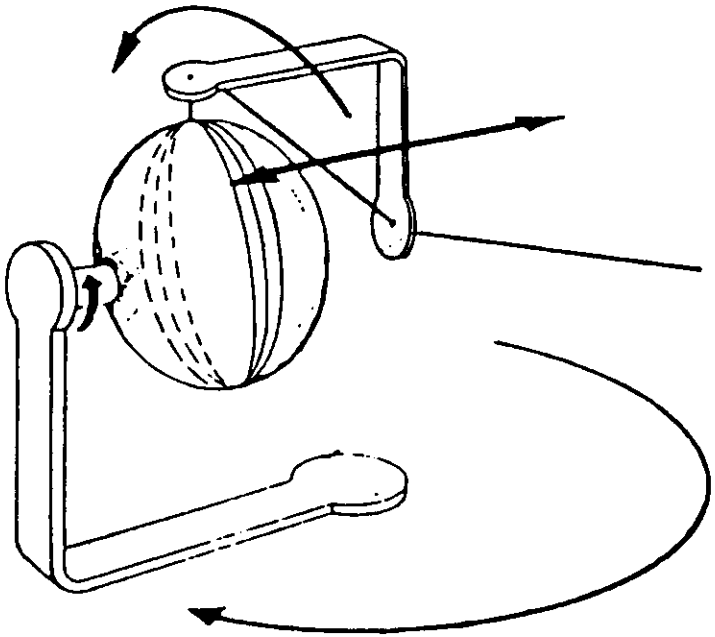

Figure 2.21.

winding pressure on mandrel

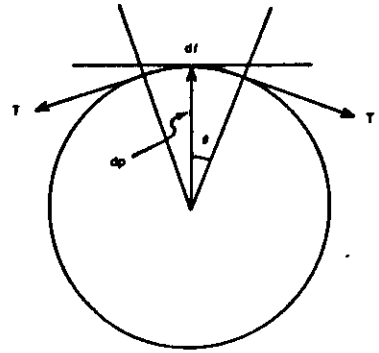

Figure 2.18.

$$\frac{T}{d^2} \ln\left(\frac{d_2}{d_1}\right)$$

bursting pressure of filament wound pressure vessels

$$\frac{\pi\sigma}{4} \frac{(d_1 - d_1)}{d_1}$$

ultrusion

imp bonding

llforming

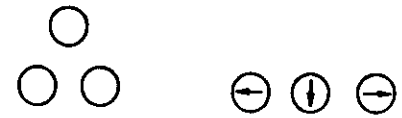

Figure 2.11. Illustrating relative fiber displacements during uniaxial compression molding.

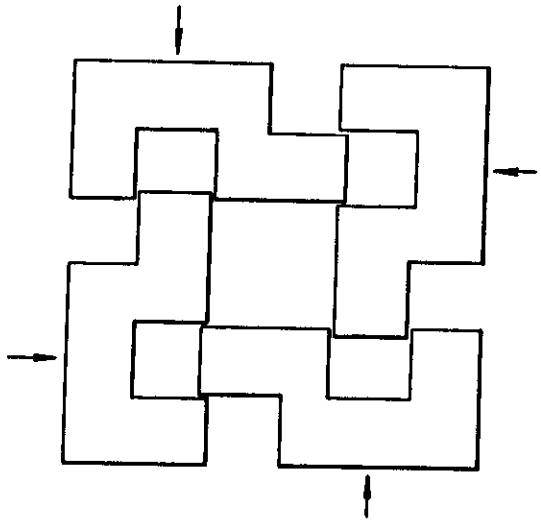

Figure 2.12. Bi-dimensional compression molding device.

Three-dimensional weaves

< 100 > orthogonal weave

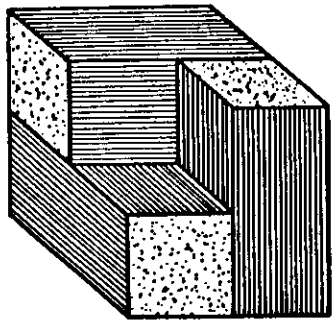

Figure 2.13. < 100 > orthogonal weave.

$$\eta = \frac{3}{4}$$

< 111 > weave (viz. 4D weave)

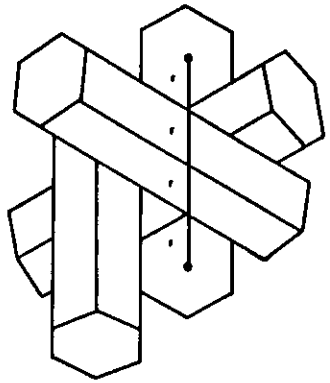

Figure 2.14. Projection along one of the fiber directions of a < 111 > three-dimensional weave.

$$\eta = 1 - \frac{\sqrt{3}}{4}$$

carbon/carbon composites

3D hybrid composites

self-lubricating bearings

Figure 2.15. Self-lubricating, three-dimensionally reinforced composite. Threads which outcrop the upper surface are PTFE (shaded). All others are reinforcing fibers.

$$t = \frac{r^2}{\alpha}$$

$$\frac{l_{critical}}{r} = \frac{\sigma}{\tau}$$

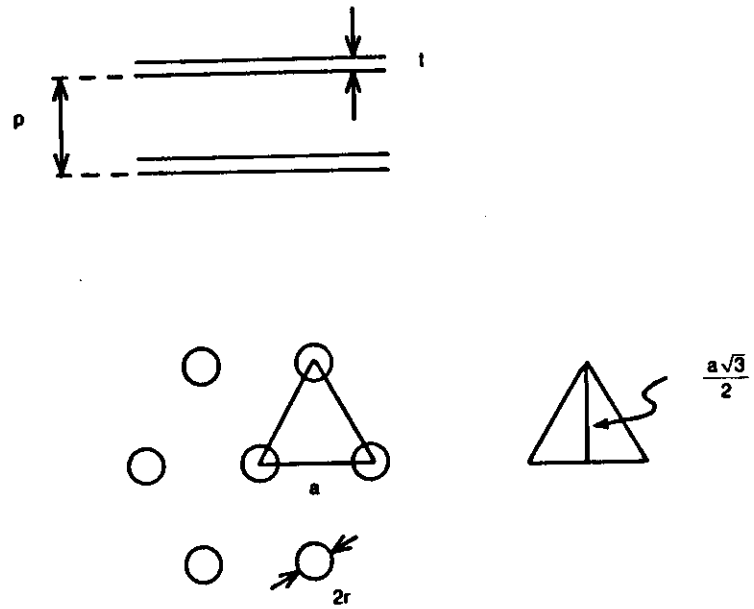

Figure 2.19.

$$\frac{d'}{d} = 2(1.105\sqrt{\alpha} - \alpha)\ \frac{\gamma'}{(1-\alpha)\gamma}$$

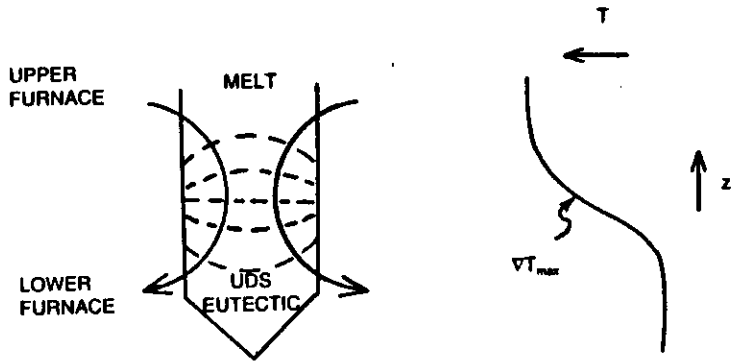

Figure 2.20.

$$\nabla^2 T = 0$$

Anisotropy of stress

Electrical conductivity

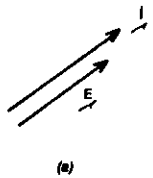

(a)

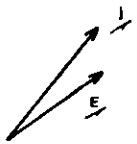

(b)

Figure 3.1.

$$\underline{j} = \sigma \underline{E}$$

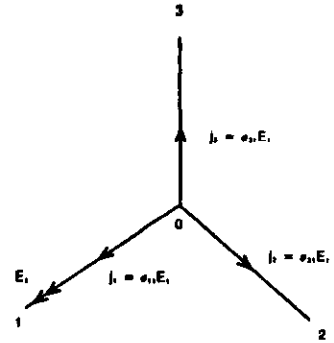

Figure 3.2.

Matrix representation of second rank tensors

$$j_i = \sigma_{ij} E_j$$

thermal conductivity

$$\frac{\partial h_i}{\partial t} = -k_{ij} \frac{\partial T}{\partial x_j}$$

stress

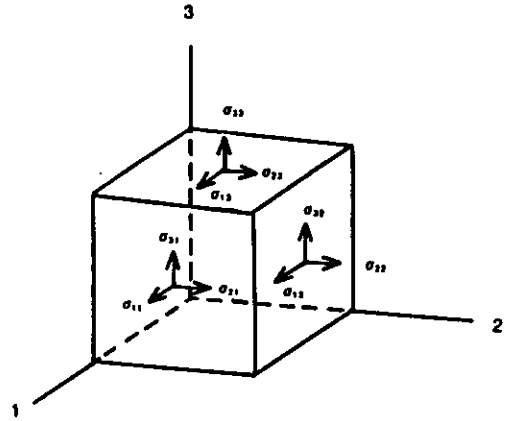

Figure 3.3. The forces on a unit cube in a homogeneously stressed solid.

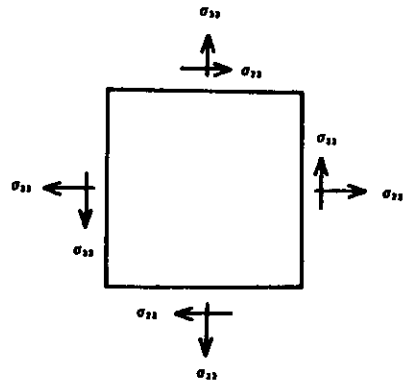

Figure 3.4.

$$p_i = \sigma_{ij} l_j$$

Transformation laws

$$T'_{ij} = a_{ik} a_{jl} T_{kl}$$

$$T_{ij} = a_{ki} a_{lj} T'_{kl}$$

stress is a symmetrical tensor

$$\sigma_{ij} = \sigma_{ji}$$

principal axes

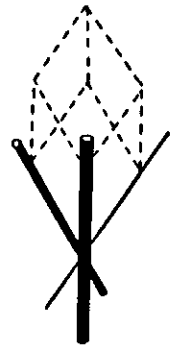

Figure 3.8. Three different gage wires obliquely oriented with respect to each other.

Equations for rotation about a principal axis

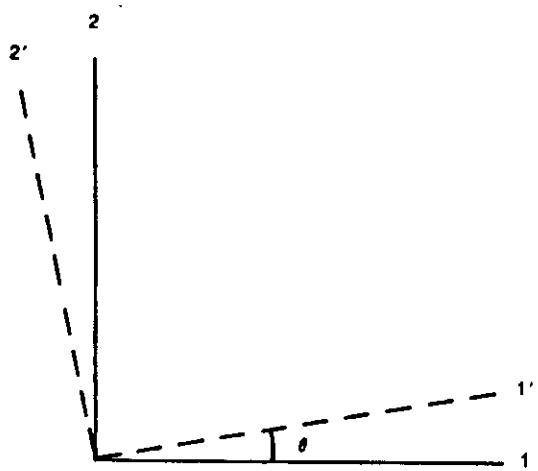

Figure 3.5.

$$\sigma'_{11} = \frac{1}{2}(\sigma_1 + \sigma_2) - \frac{1}{2}(\sigma_2 - \sigma_1)\cos 2\theta$$

$$\sigma'_{22} = \frac{1}{2}(\sigma_1 + \sigma_2) + \frac{1}{2}(\sigma_2 - \sigma_1)\cos 2\theta$$

$$\sigma'_{12} = \frac{1}{2}(\sigma_2 - \sigma_1)\sin 2\theta$$

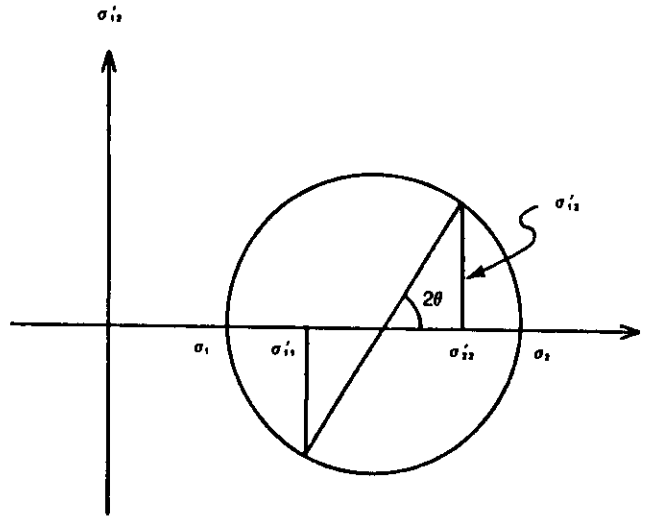

Figure 3.6. The Mohr circle.

maximum $\sigma'_{12} = \frac{1}{2}(\sigma_2 - \sigma_1)$

$$S_{ij}x_ix_j = 1$$

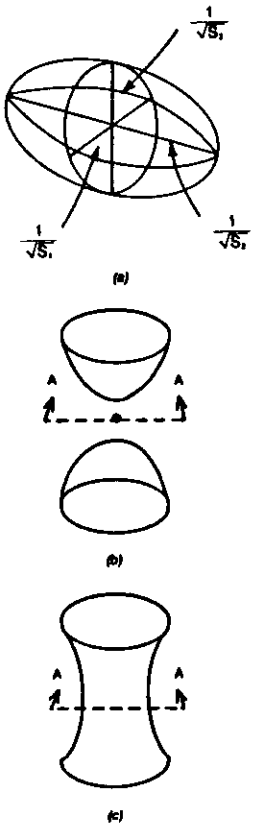

Figure 3.7. Representation quadrics for second rank tensors. (a) All three principal properties positive, (b) two negative and one positive (section A-A is an imaginary ellipse, and the other two sections, lying in the plane of the paper are hyperbolas), (c) two positive and one negative (section A-A is a real ellipse). The case of all three principal properties negative gives an imaginary ellipsoid.

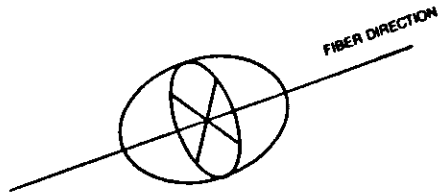

Figure 3.10. Representation quadric for a uniaxial composite.

stress ellipsoid

$$\frac{1}{\sqrt{\sigma_1}}, \frac{1}{\sqrt{\sigma_2}}, \frac{1}{\sqrt{\sigma_3}}$$

Neumann's principle

conductivity has higher symmetry than the laminate symmetry

magnitude of a tensor property

$$|\sigma| = \sigma_{ij}l_il_j$$

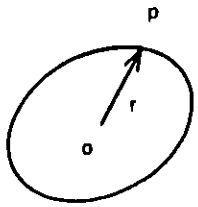

Figure 3.11.

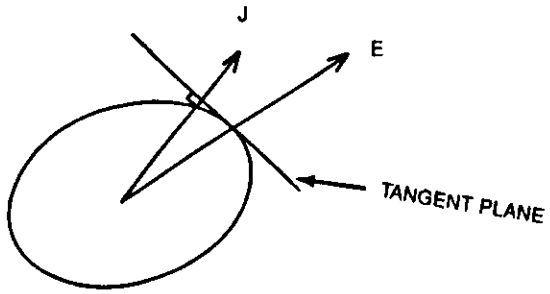

Figure 3.12.

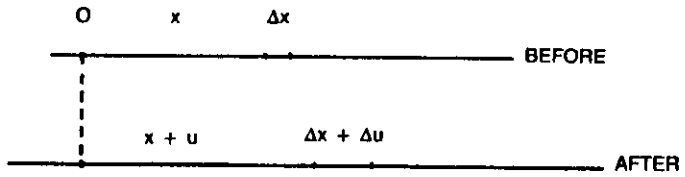

Figure 3.13.

strain is the derivative of displacement

$$e = \frac{du}{dx}$$

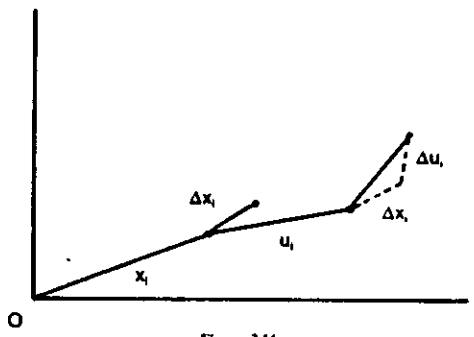

Figure 3.14.

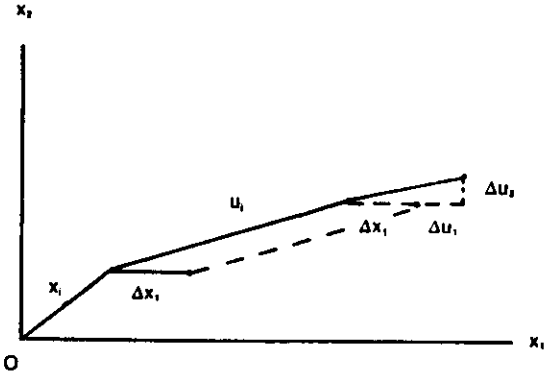

Figure 3.15.

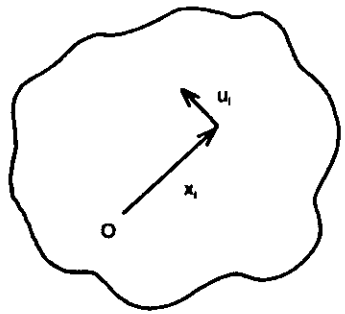

Figure 3.16.

$$\epsilon_{ij} = \frac{1}{2}(e_{ij} + e_{ji})$$

rotation

$$\omega_{ij} = \frac{1}{2}(e_{ij} - e_{ji})$$

strain is a symmetrical second rank tensor

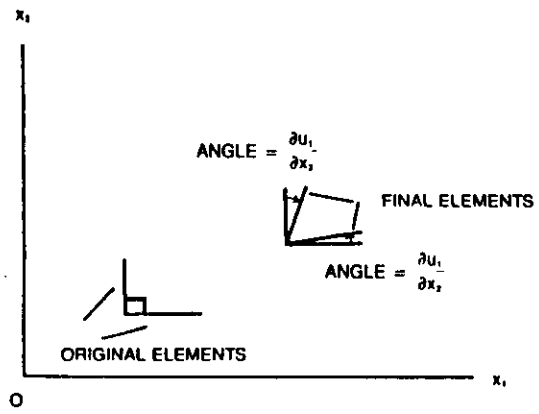

Figure 3.17.

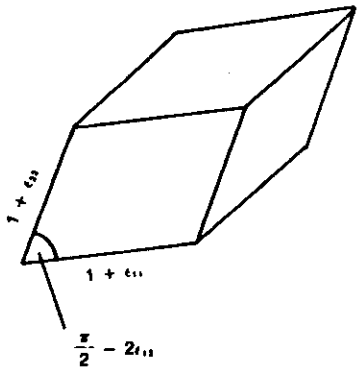

Figure 3.18.

principal strains

engineering strains

Mohr circle

simple shear is pure shear plus a rotation

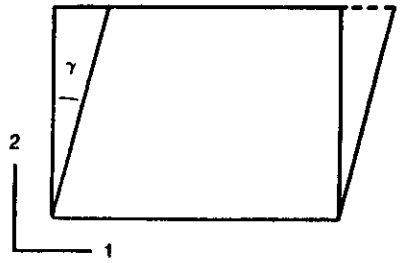

Figure 3.19.

$$[e_{ij}] = \begin{bmatrix} 0 & \gamma & 0 \\ 0 & 0 & 0 \\ 0 & 0 & 0 \end{bmatrix}$$

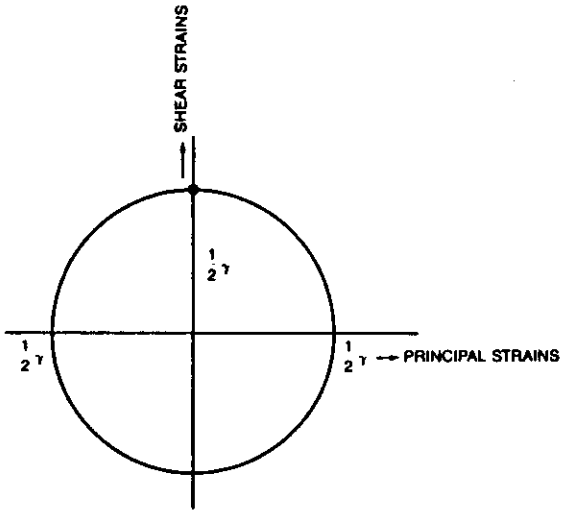

Figure 3.20.

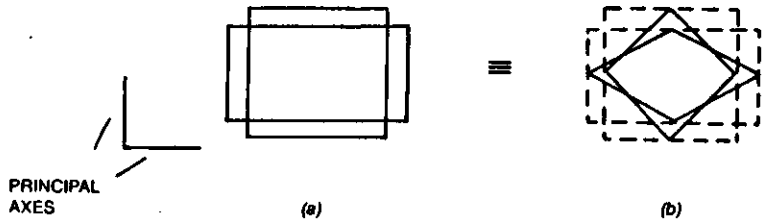

Figure 3.21. Deformation of a square to a rectangle. (a) Sides of square parallel to principal axes. (b) Sides of square at 45° to principal axes.

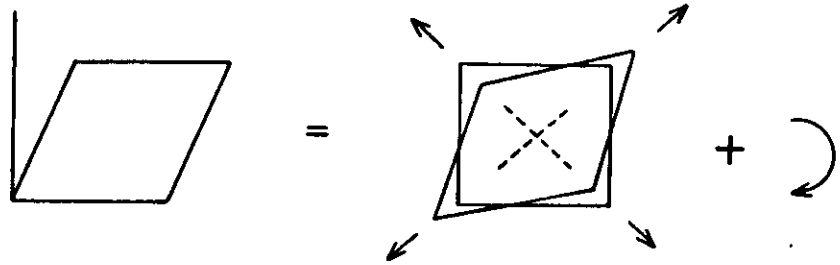

Figure 3.22. Simple shear is pure shear plus a rotation. The broken ±45° lines represent fiber orientations that would resist shear.

strain due to thermal expansion is a matter tensor

$$\epsilon_{ij} = \alpha_{ij} \Delta T$$

Holes in plates

bolt holes, cut-outs

Inglis calculation

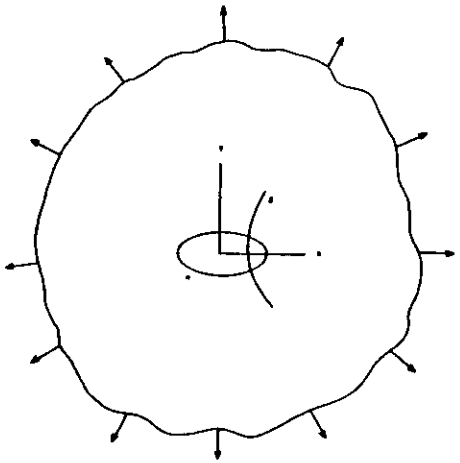

Figure 4.1.

elliptic holes

orthogonal curvilinear co-ordinates

$f_1(x,y) = \alpha$, a constant:

$f_2(x,y) = \beta$, another constant

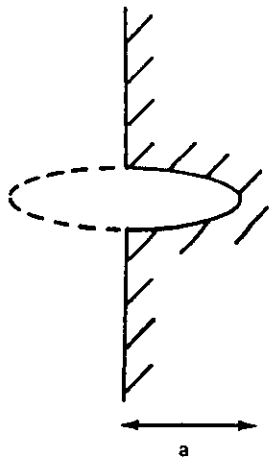

Figure 4.3. Showing the geometrical equivalence of a surface crack (depth a) to an elliptic hole (length $2a$).

uniaxial tension perpendicular to a crack

$$\sigma_{\alpha\alpha} = \frac{\sigma}{2}(1 - \cos 2\beta)$$

$$\sigma_{\beta\beta} = \frac{\sigma}{2}(1 + \cos 2\beta)$$

$$\sigma_{\alpha\beta} = -\frac{\sigma}{2}\sin 2\beta$$

stress concentration at the edge of a crack

$$\sigma_{aa} = \sigma\left(1 + 2\sqrt{\frac{a}{\varrho}}\right)$$

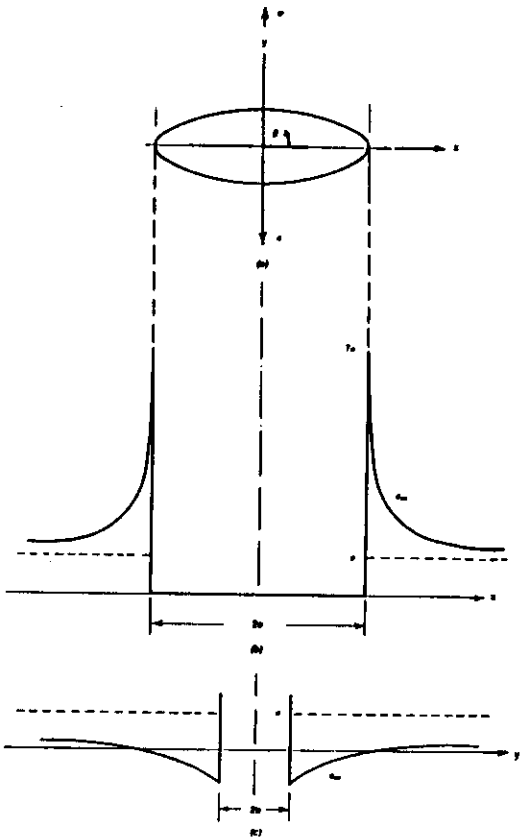

Figure 4.2.

circular hole

$$\sigma_{aa} = 3\sigma$$

Holes in anisotropic plates

Airy stress function

functions of a complex variable

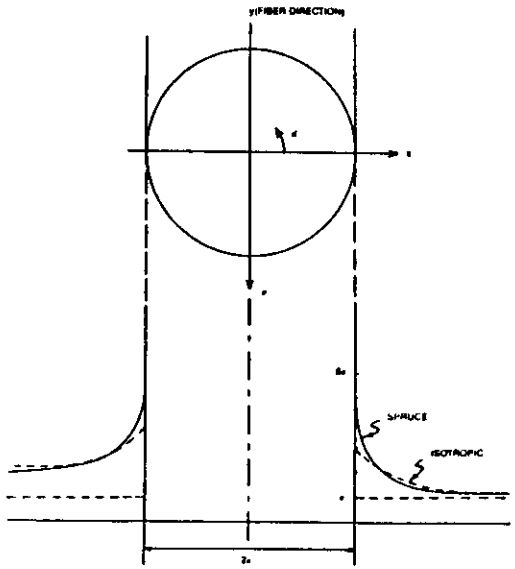

Figure 4.4. Distribution of σ_{yy} along the x-axis ($\beta = 0$). Stress is applied in the fiber direction ($\beta = \pi/2$).

stress amplification of up to 9 compared with 3 in an isotropic plate

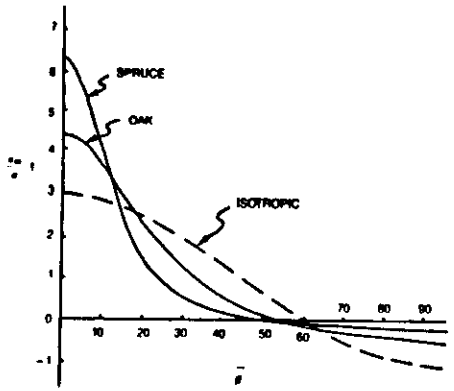

Figure 4.5. Distribution of circumferential stress ($\sigma_{\alpha\alpha}$ in Inglis' notation) around the edge of a circular hole. Tensile stress σ applied in the fiber direction ($\beta = \pi/2$).

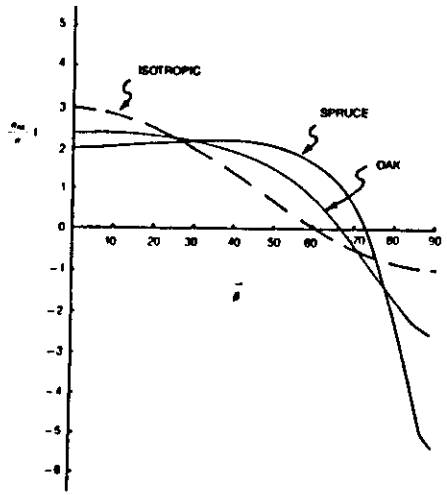

Figure 4.6. Distribution of circumferential stress $\sigma_{\alpha\alpha}$ (Inglis' notation) around the edge of a circular hole. Tensile stress applied in the transverse direction ($\beta = 0$).

tress concentration is highly localised

$0.15r$

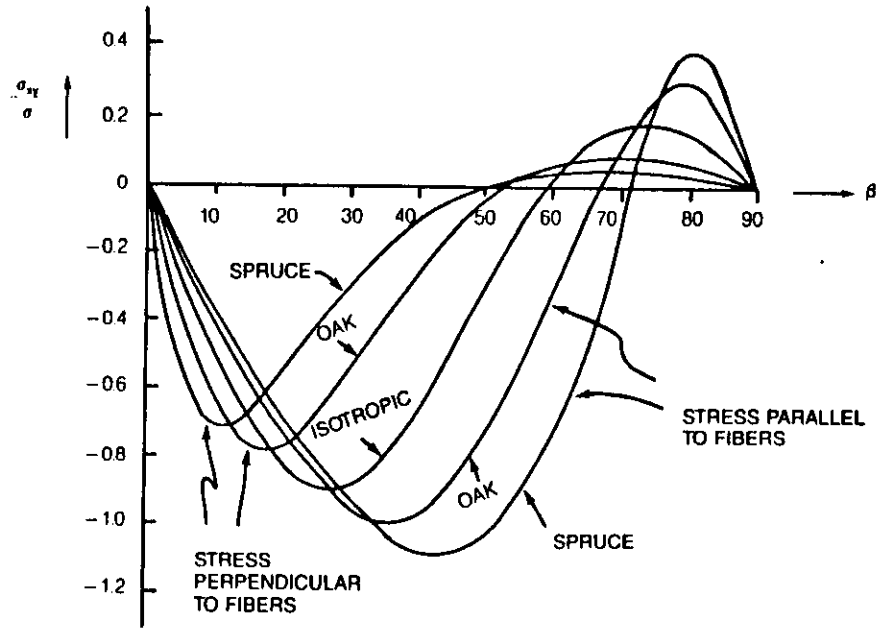

Figure 4.7. Distribution of shear stress σ_{xy} around the edges of a circular hole. Tensile stress applied parallel to $\beta = \pi/2$.

Free edge effect (viz. shear stress transverse to fibers in uniaxial composite containing hole)

If hole is small, composite withstands larger stress than predicted above

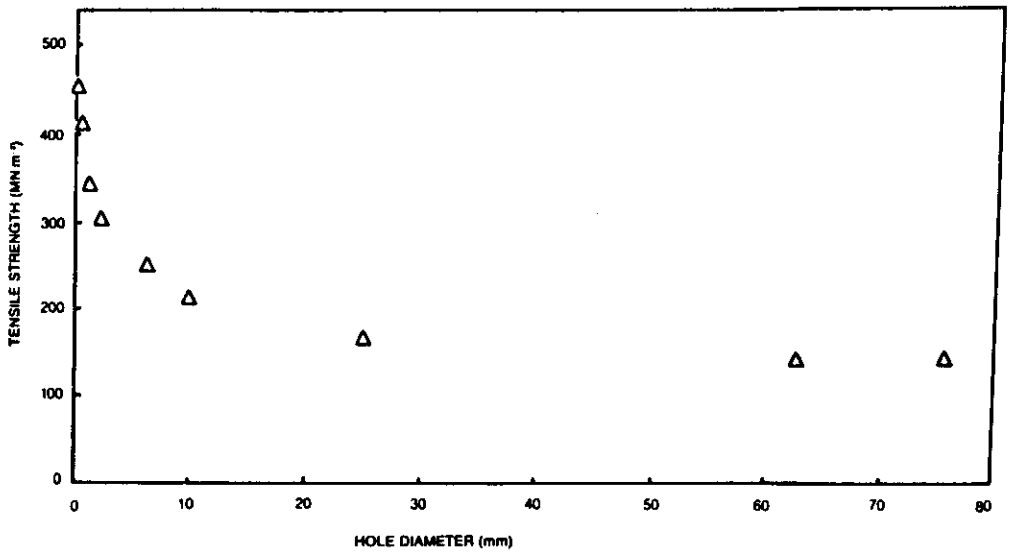

Figure 4.8. Variation of tensile strength with size of circular hole in a $[0/\pm 45]_{2s}$ carbon fiber/epoxy resin laminate. (Data taken from Tables 1 and 2 of M. E. Waddoups, J. R. Eisenmann and B. E. Kaminski, "Macroscopic Fracture Mechanics of Advanced Composite Materials," *J. Composite Materials*, 5:446–454 (1971)).

make generous use of doublers

Failure sites at holes in uniaxial composites subjected to axial and transverse tension and compression

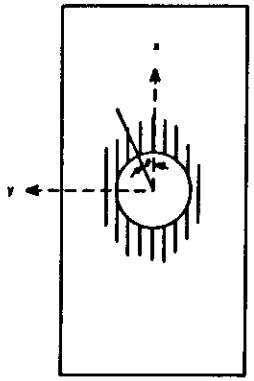

Figure 4.9.

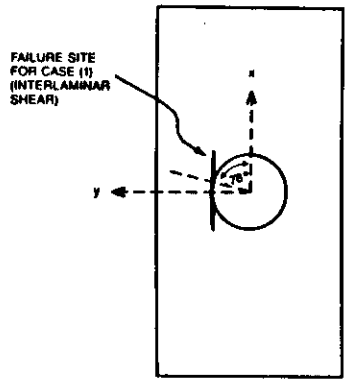

Figure 4.10.

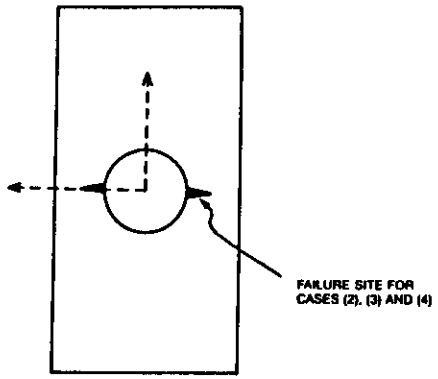

Figure 4.11.

Anisotropy of elasticity

Hooke's law

$$\epsilon = s\sigma$$

ompliance s

$$\sigma = c\epsilon$$

tiffness c

$$\epsilon_{ij} = s_{ijkl}\sigma_{kl}$$

$$\sigma_{ij} = c_{ijkl}\epsilon_{kl}$$

ny one component of strain is proportional to *all* of the components of stress

coupling

(a)

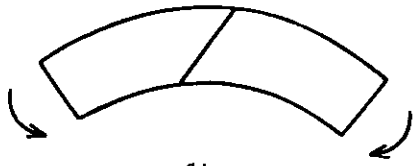

(b)

(c)

Figure 5.1. (a) Uniaxial stress generates longitudinal and transverse strains, and three shears. (b) Bending produces shears and twists. (c) Twisting produces bending as well as shears.

effect of longitudinal stiffness on torsional stiffness

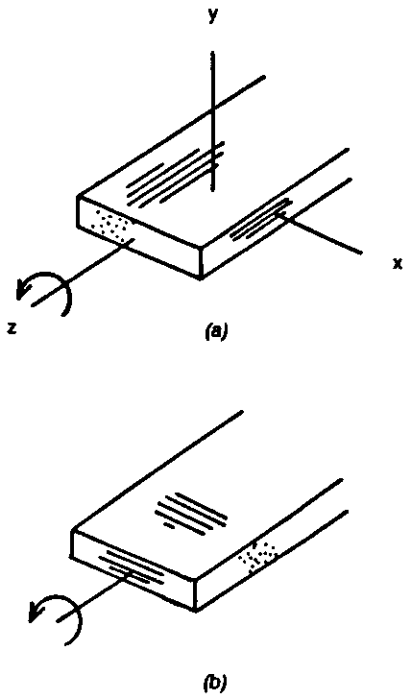

Figure 5.2. Illustrating the effect on torsional stiffness of axial stiffness of a fan blade (after K. T. Kedward).

compliance and stiffness are fourth rank tensors

$$31 - 81$$

6561 coefficients involved when transforming axes

but since stress and strain are symmetrical 81 reduces to 36

Two-suffix (or matrix) notation

$$\begin{bmatrix} \sigma_{11} & \sigma_{12} & \sigma_{31} \\ & \sigma_{22} & \sigma_{23} \\ & & \sigma_{33} \end{bmatrix}$$

$$\begin{bmatrix} \sigma_1 & \sigma_6 & \sigma_5 \\ & \sigma_2 & \sigma_4 \\ & & \sigma_3 \end{bmatrix}$$

6×6 array $= 36$ numbers for compliance, and a different 36 for stiffness

$$\epsilon_i = s_{ij}\sigma_j$$

$$\sigma_i = c_{ij}\epsilon_j$$

however, since each array is symmetrical about leading diagonal, 36 reduces to 21

most laminates possess symmetry of the kind possessed by orthorhombic crystals, so the 36 is further reduced to 9

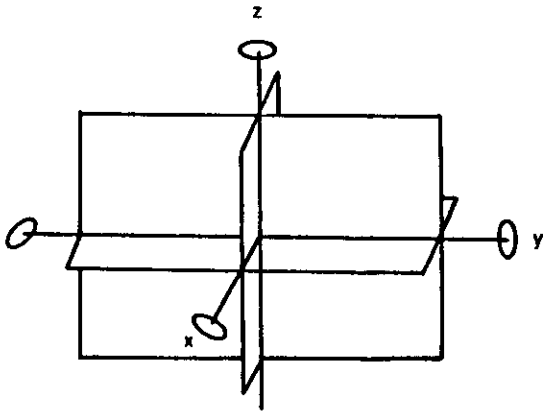

Figure 7.1.

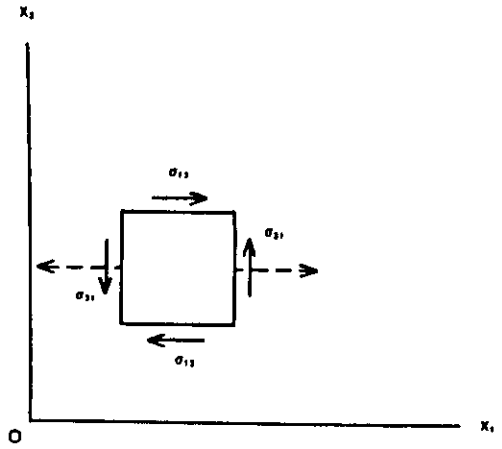

(a)

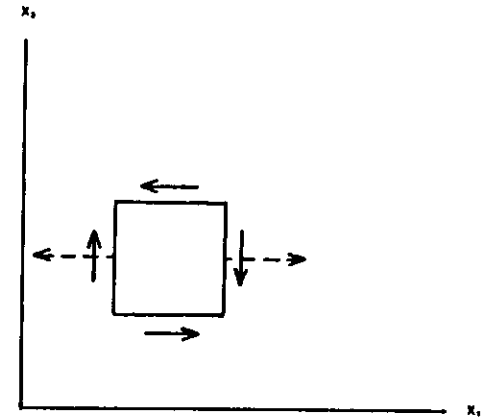

(b)

Figure 5.3. (a) Illustrating the extension e_{11} (broken arrows) produced by shear stress σ_{21}. Notice the convention that the σ_{12} and σ_{21} furthest from the origin point into the first quadrant for positive shear stress. (b) Reversal of shear stresses by operation of two-fold symmetry.

$$s_{ij} = \begin{bmatrix} s_{11} & s_{12} & s_{13} & 0 & 0 & 0 \\ & s_{22} & s_{23} & 0 & 0 & 0 \\ & & s_{33} & 0 & 0 & 0 \\ & & & s_{44} & 0 & 0 \\ & & & & s_{55} & 0 \\ & & & & & s_{66} \end{bmatrix}$$

$$s_{11} = \frac{1}{E_1}; \quad s_{21} = -\frac{\nu_{21}}{E_2} = -\frac{\nu_{12}}{E_1}$$

$$s_{31} = -\frac{\nu_{31}}{E_3} = -\frac{\nu_{13}}{E_1}; \quad s_{22} = \frac{1}{E_2}$$

etc.

major and minor Poisson's ratio

ν_{12}

ν_{13}

rotation about a principal axis

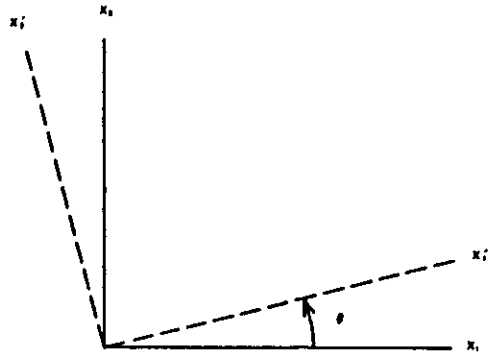

Figure 5.4

$$s_{11}' = s_{11}m^4 + (2s_{21} + s_{66})n^2m^2 + s_{22}n^4 = \frac{1}{E_1'}$$

$$s_{22}' = s_{11}n^4 + (2s_{21} + s_{66})n^2m^2 + s_{22}n^4 = \frac{1}{E_2'}$$

$$s_{21}' = (s_{11} + s_{22})n^2n^2 + s_{21}(m^4 + n^4) - s_{66}m^2n^2 = \frac{\nu_{21}'}{E_2'}$$

etc.

where

$$m = \cos\theta$$

$$n = \sin\theta$$

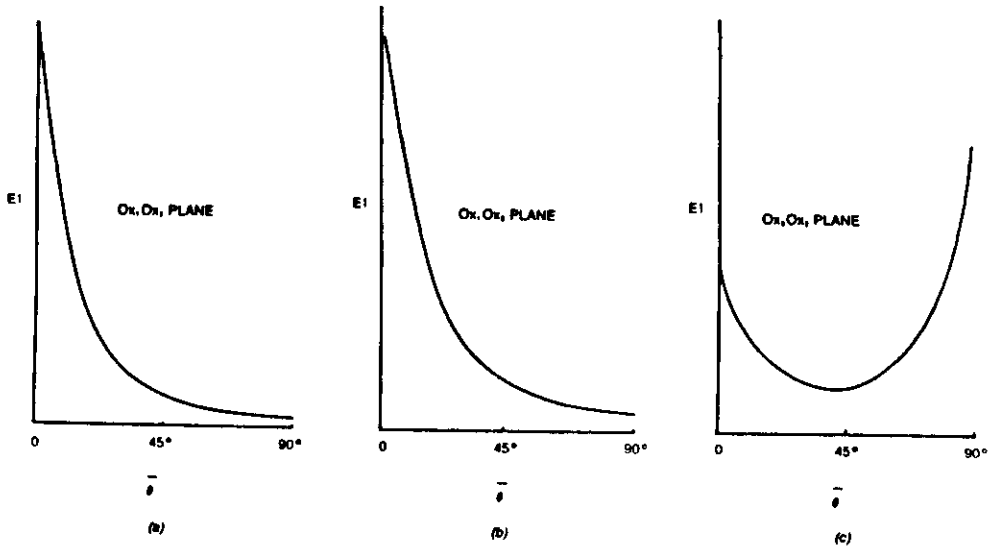

Figure 5.5. Effect of fiber direction on Young's modulus. Rotation (a) in the $Ox_1 Ox_2$ plane, (b) in the $Ox_1 Ox_3$ plane, (c) in the $Ox_2 Ox_3$ plane.

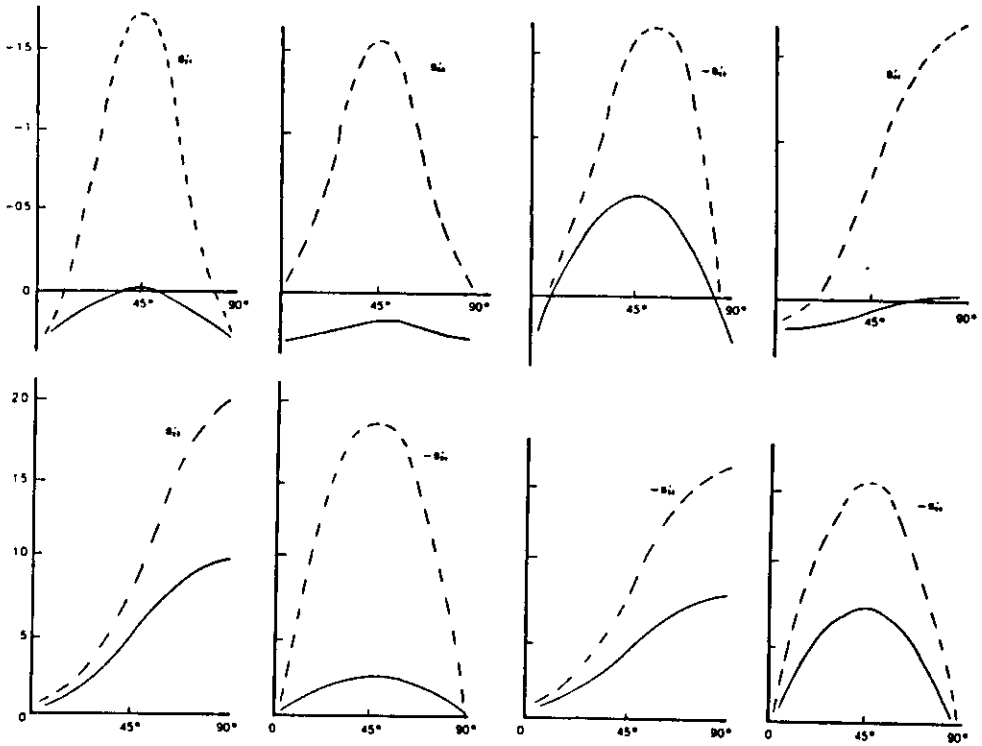

Figure 5.6. s'_{ij} for rotations in the $Ox_1 Ox_2$ plane. [0° = grain (fiber) direction, 90° = transverse direction]. s'_{ij} unit = 10^{-3} m^{2}N^{-1}. —— hard wood, ------ soft wood.

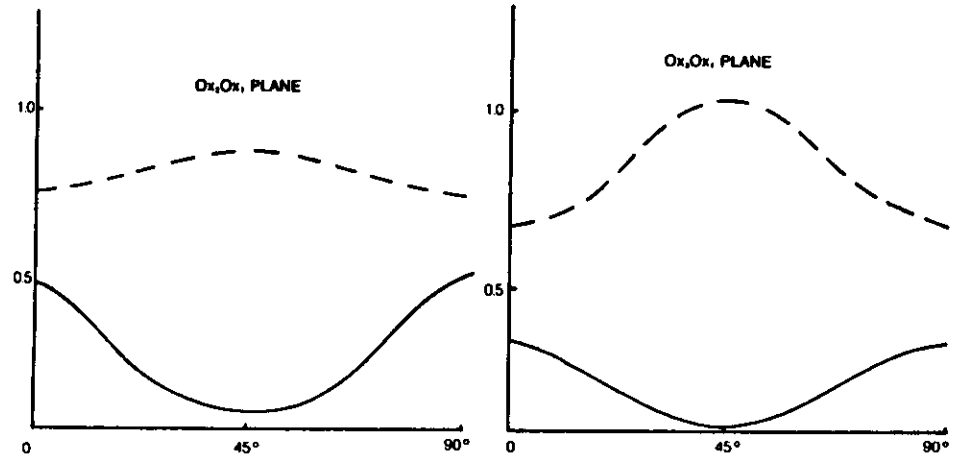

Figure 5.7 Variations of G'_{ij} with fiber direction for an elastically strong uniaxial composite (full lines) and an elastically weak uniaxial composite (broken lines). Units = GNm^{-1}. After R. F. S. Hearmon [24].

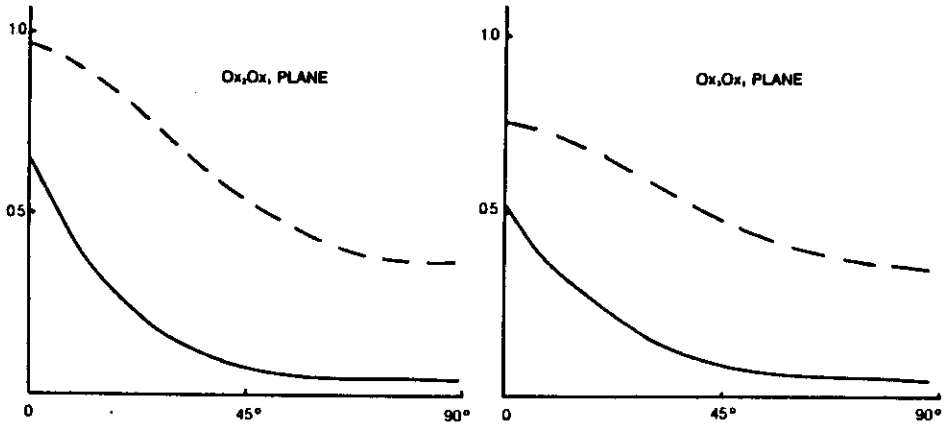

Figure 5.8. Variations of G'_{ij} with fiber direction for strong and weak composites. Units = GNm^{-1}. After R. F. S. Hearmon [24].

four "new" coefficients

s'_{61}

s'_{62}

s'_{63}

s'_{64}

Coupling between shear and extension

B_{12}

concept of "pure" and "free" modulus

$\pm\theta$

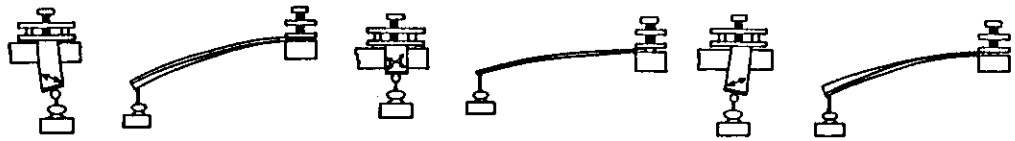

Figure 5.9. Illustrating coupling between shear and extension. After R. F. S. Hearmon [24].

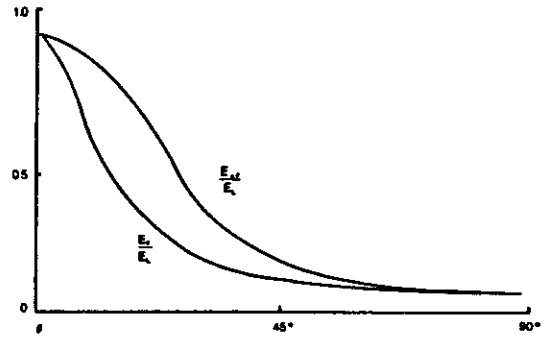

Figure 5.10. Variation of the axial Young's modulus with orientation angle for single ply and symmetric ($\pm\theta$) laminates.

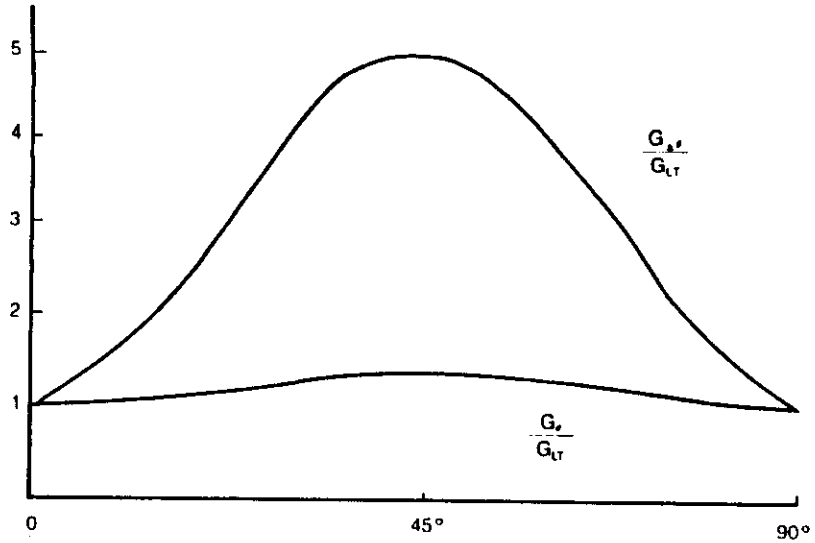

Figure 5.11. Variation of shear modulus with orientation angle for single ply and symmetric $(\pm\theta)$ laminates.

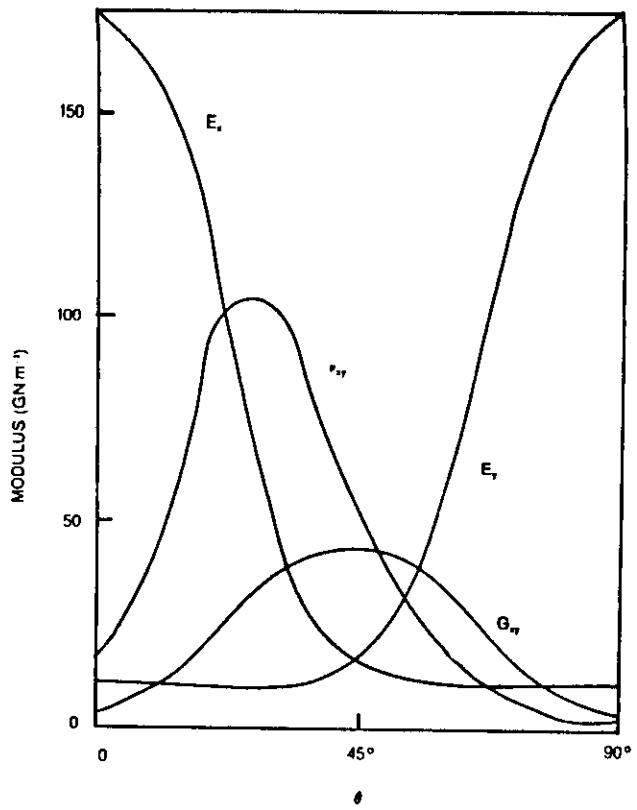

Figure 5.12. Laminate elastic constants for symmetric $(\pm\theta)$ HM-graphite/epoxy laminates.

Orthotropic laminates

orthogonal anisotropic plates (viz. orthotropic plates)

[0/90]

main axes of stiffness

generally and specially orthotropic plates

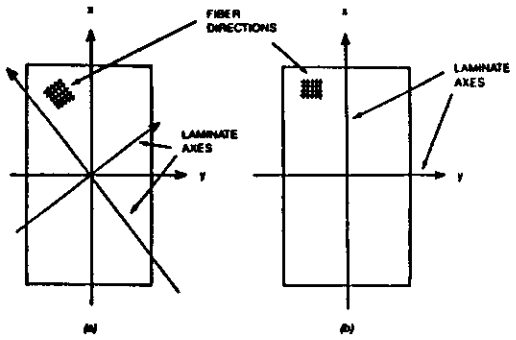

Figure 6.1. (a) Generally-orthotropic plate, (b) specially-orthotropic plate.

Hooke's law

$$\epsilon_x = s'_{11}\sigma_x + s'_{12}\sigma_y + s'_{16}\tau$$

$$\epsilon_y = s'_{21}\sigma_x + s'_{12}\sigma_y + s'_{66}\tau$$

$$\gamma = s'_{61}\sigma_x + s'_{62}\sigma_y + s'_{66}\tau$$

four independent components of compliance

$s_{11}, s_{22}, s_{12}, s_{66}$

rotation about a principal axis

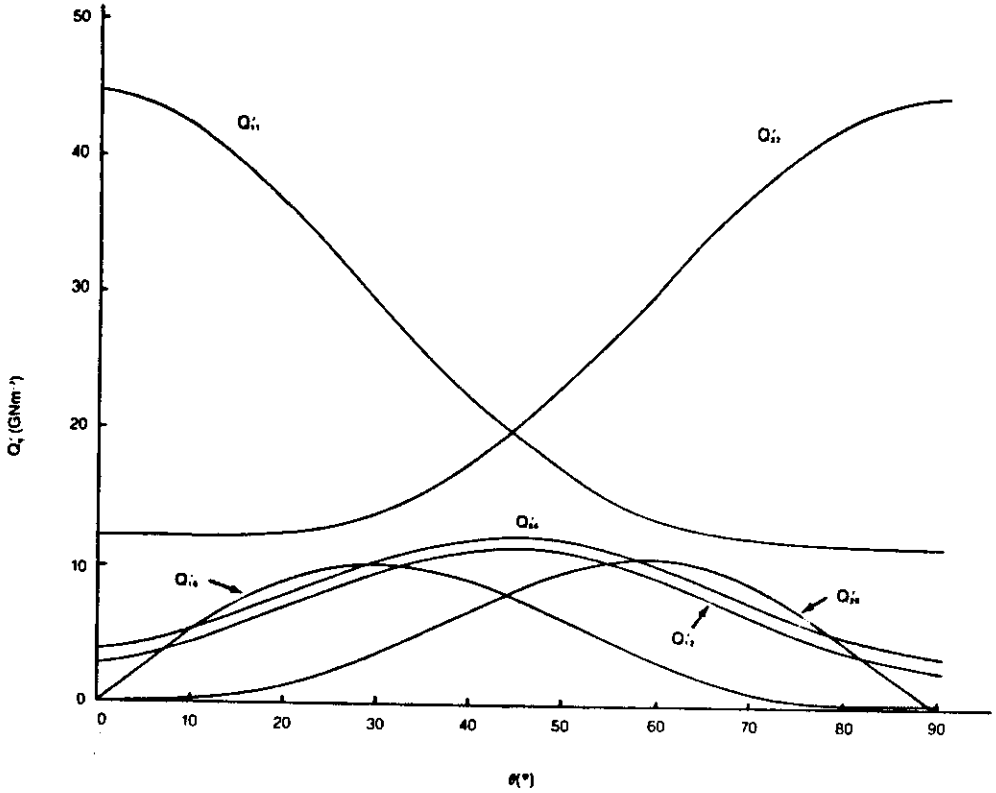

Figure 6.2. Q'_{ij} ($= c'_{ij}$) for glassfiber reinforced epoxy resin ($\eta = 1/2$). Rotation in the Ox_1, Ox_2 plane. 0° = fiber direction, 90° = transverse direction [after S. B. Dong, UCLA (1986)].

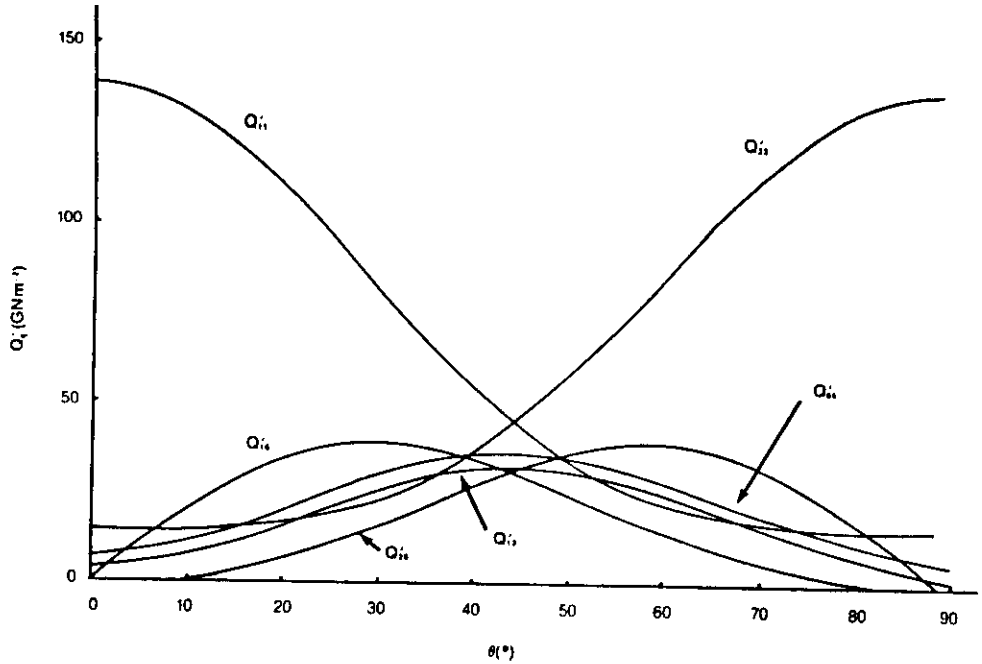

Figure 6.3. Q'_{ij} ($= c'_{ij}$) for carbon fiber reinforced epoxy resin ($\eta = 1/2$). Rotations in the Ox_1, Ox_2 plane. 0° = fiber direction, 90° = transverse direction [after S. B. Dong, UCLA (1986)].

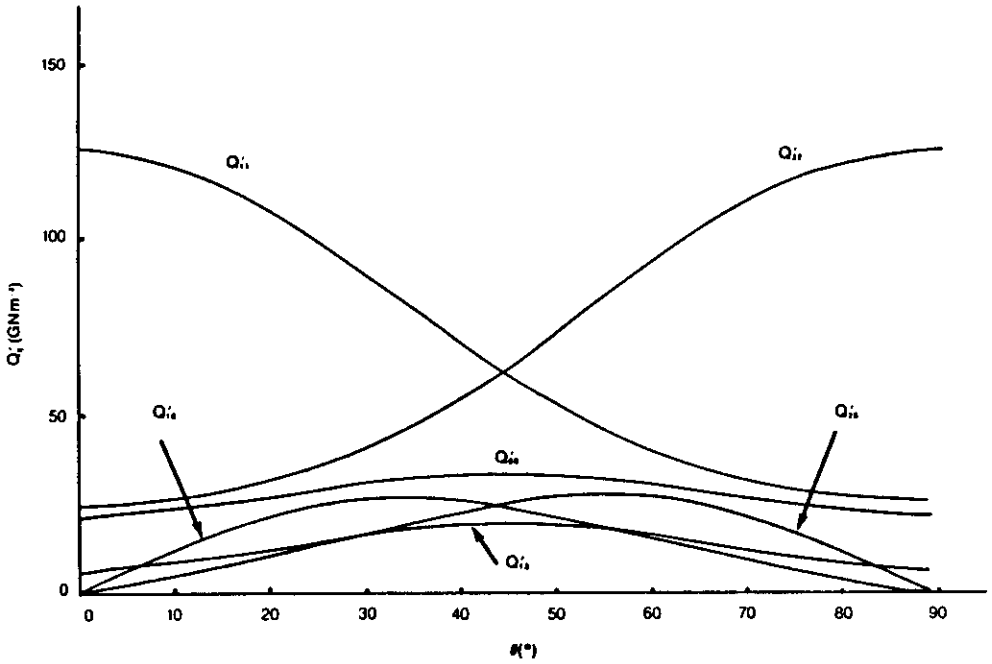

Figure 6.4. Q'_{ij} (= c'_{ij}) for carbon fiber reinforced aluminum (η = 2/5). Rotations in the Ox_1 Ox_2 plane. 0° = fiber direction, 90° = transverse direction [after S. B. Dong, UCLA (1986)].

bending moments

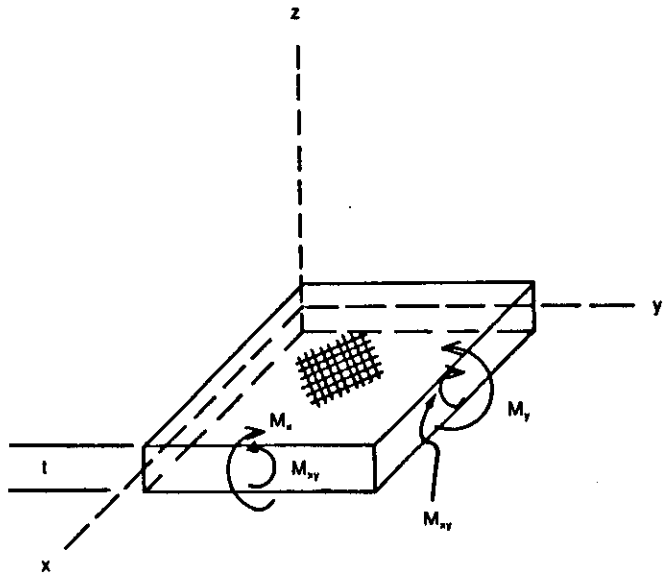

Figure 6.5. Bending moments in an element of orthotropic laminate.

$$M_x = \int_{-\frac{t}{2}}^{\frac{t}{2}} \sigma_x z\,dz$$

$$M_y = \int_{-\frac{t}{2}}^{\frac{t}{2}} \sigma_y z\,dz$$

$$M_{xy} = \int_{-\frac{t}{2}}^{\frac{t}{2}} \tau z\,dz$$

differential equation for buckling load

$$\frac{t^3}{12}\left\{ c'_{11}\frac{\partial^4 w}{\partial x^4} + 4c'_{16}\frac{\partial^4 w}{\partial x^3 \partial y} + (2c'_{12} + 4c'_{66})\frac{\partial^4 w}{\partial x^2 \partial y^2} + 4c'_{26}\frac{\partial^4 w}{\partial x \partial y^3} + c'_{22}\frac{\partial^4 w}{\partial y^4} \right\} - P = 0$$

$$\text{cf. } \nabla^4 w = \frac{P}{D}$$

Constitutive equation for orthotropic laminates

$$\begin{bmatrix} N \\ M \end{bmatrix} = \begin{bmatrix} A & B & \epsilon^0 \\ B & D & \kappa \end{bmatrix}$$

normal strains

ϵ^0

plate curvatures

κ

fiber cross-overs

resin-rich material

modulus measured in tension differs from that measured in bending

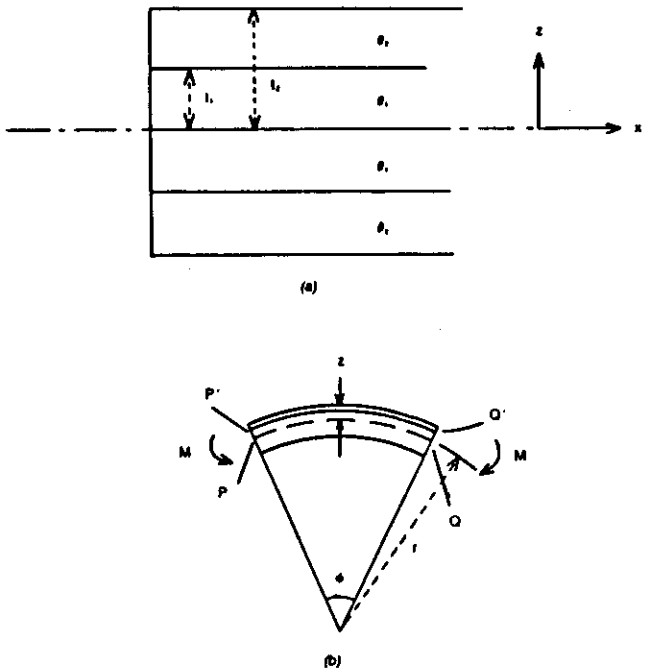

Figure 6.7.

$$E_x = \frac{E_{\theta_1} + E_{\theta_2}}{2}$$

$$E_x = \frac{E_{\theta_1} + E_{\theta_2}}{8}$$

coupling

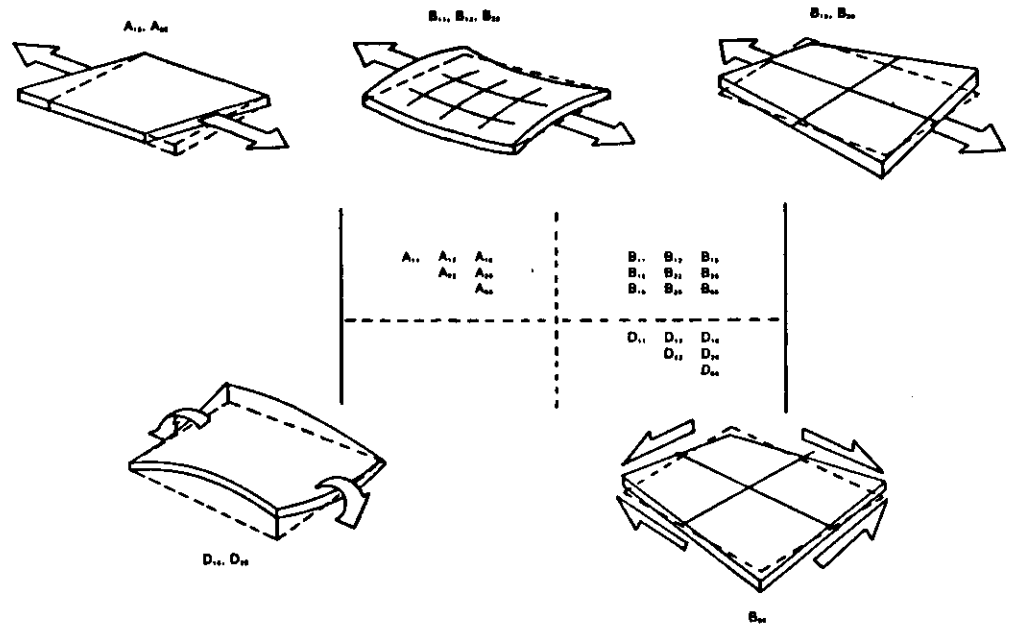

Figure 6.8. Illustrating coupling phenomena for orthotropic laminates.

A_{16} relates σ_1(i.e. σ_x), ϵ_6(i.e. ϵ_{xy})

B_{26} relates σ_2(i.e. σ_y), ϵ_6(i.e. ϵ_{xy})

M_2(i.e. M_y), κ_6(i.e. κ_{xy})

etc.

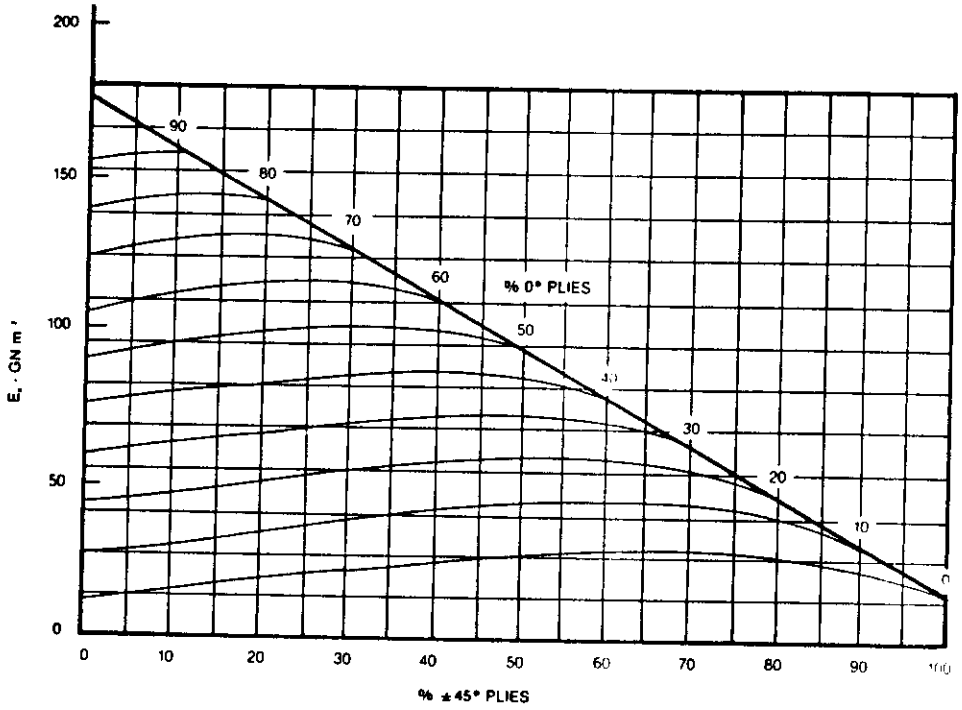

Figure 6.9 Longitudinal modulus (E_x) for $[0/\pm 45/90]_s$ carbon fiber/epoxy resin laminates.

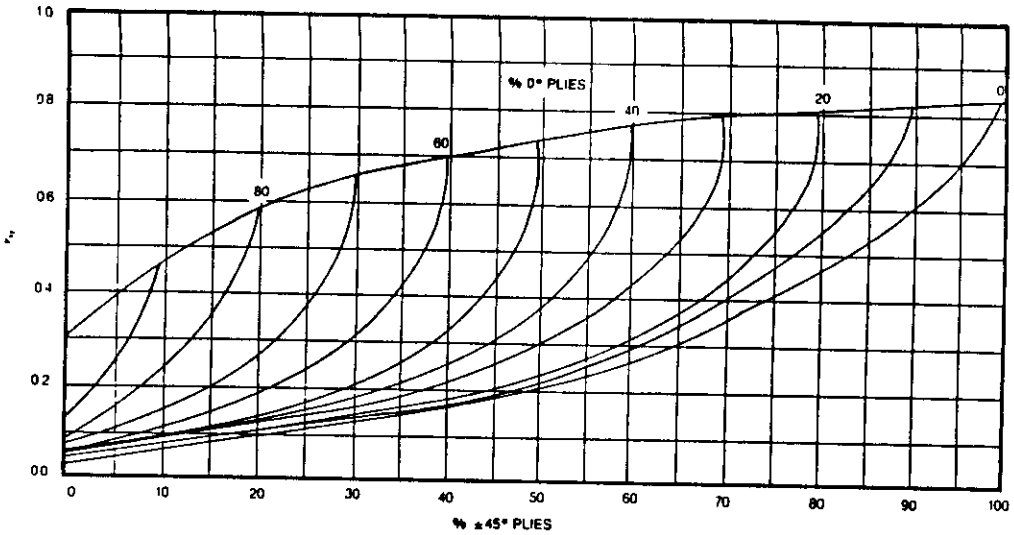

Figure 6.10 Major Poisson's ratio for $[0/\pm 45/90]_s$ carbon fiber/epoxy resin laminates.

$[0_i/\pm 45_j/\pm 90_k]_s$

Laminate code

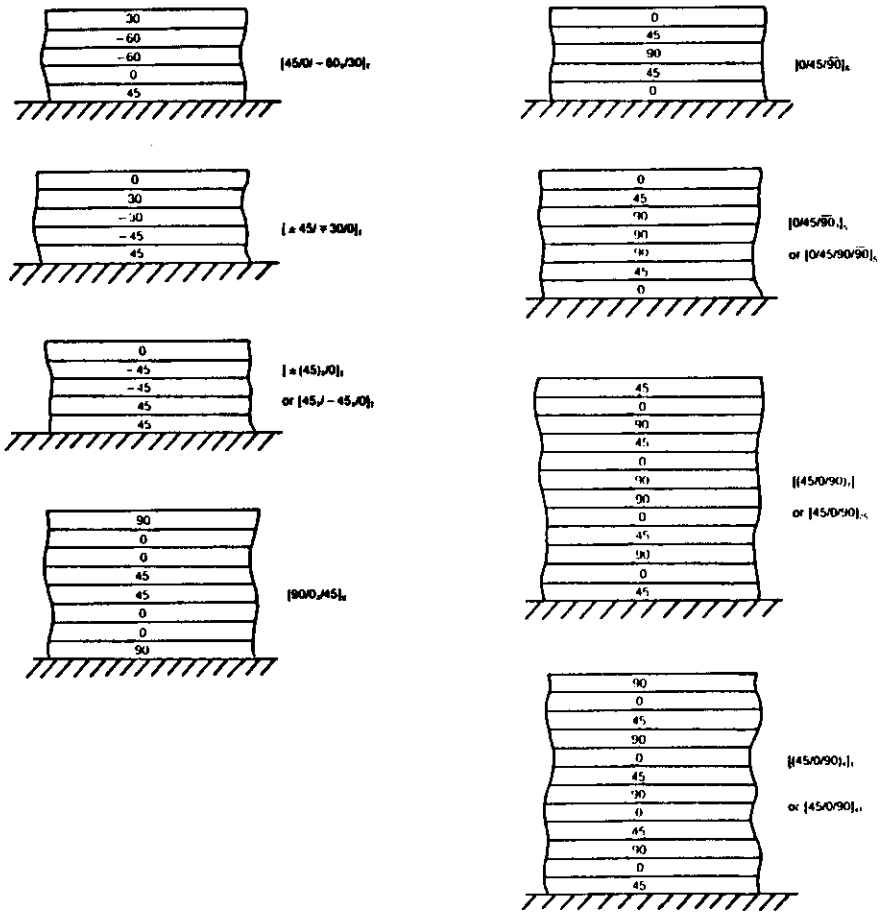

Figure 6.13. Examples of laminate sequences (after K. T. Kedward).

Thermal expansion

small *uniform* temperature change ΔT

homogeneous deformation

$$\varepsilon_{ij} = \alpha_{ij}\Delta T$$

coefficients of expansion α_{ij}

symmetrical second rank tensor

$$\begin{bmatrix} \alpha_{11} & \alpha_{12} & \alpha_{13} \\ & \alpha_{22} & \alpha_{23} \\ & & \alpha_{33} \end{bmatrix}$$

orthorhombic symmetry

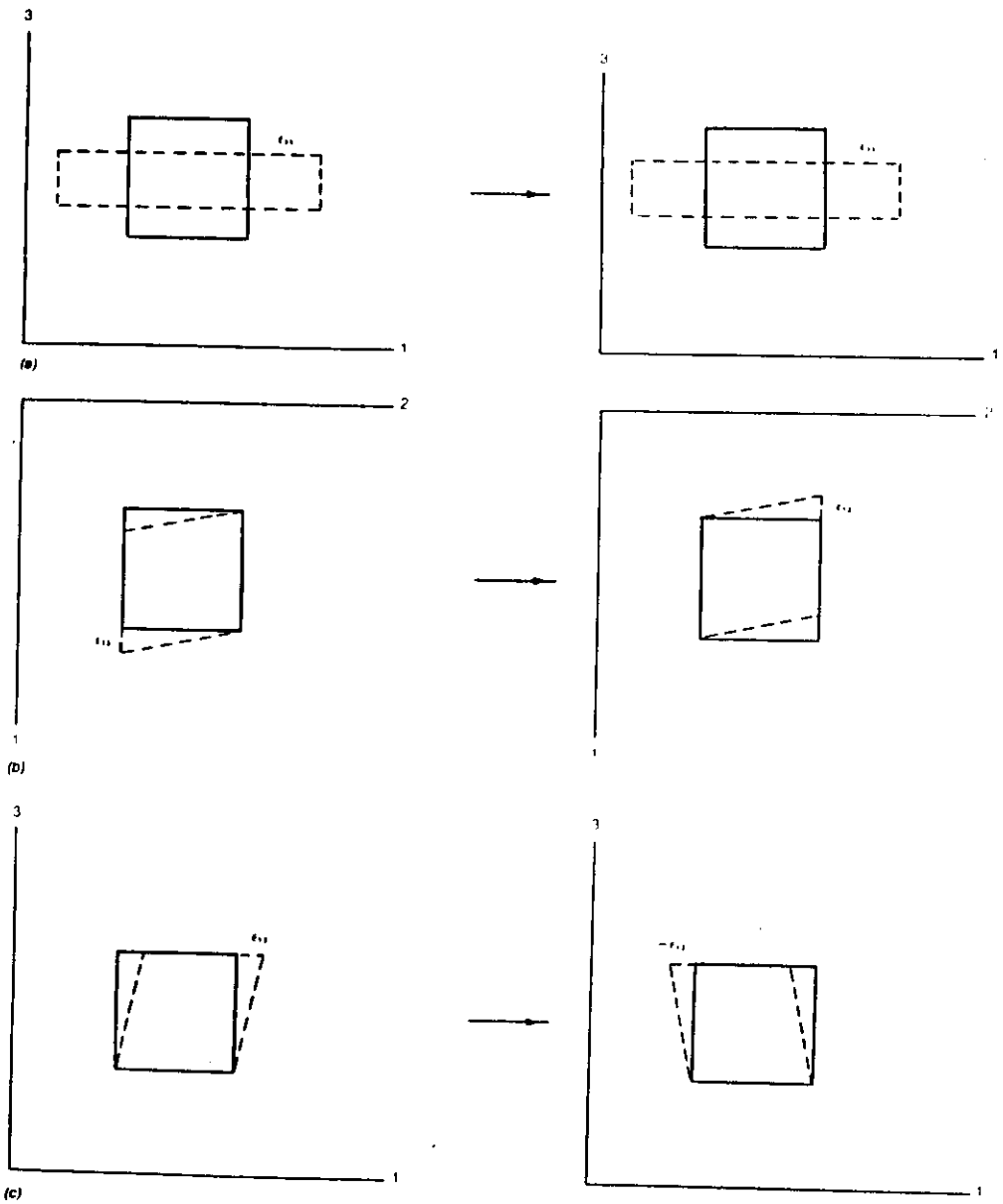

Figure 7.2. (a) ε_{11}, ε_{33} similar to ε_{11}, (b) ε_{12}, (c) ε_{23} similar to ε_{12}

$$\begin{bmatrix} \alpha_{11} & 0 & 0 \\ & \alpha_{22} & 0 \\ & & \alpha_{33} \end{bmatrix}$$

three coefficients

Isotropic fibers (glass) in an isotropic matrix (resin)

$$\alpha_{11} = \frac{E_f\alpha_f\eta + E_m\alpha_m(1-\eta)}{E_f\eta + E_m(1-\eta)}$$

$$\alpha_{22} = (1+\nu_m)\alpha_m(1-\eta) + (1+\nu_f)\alpha_f\eta - \alpha_{11}[\nu_f\eta + \nu_m(1-\eta)]$$

uniaxial composites:

glass/epoxy ($\eta = 1/2$)

$\alpha_{11} = 58 \times 10^{-6}K^{-1}$

$\alpha_{22} = 2 \times 10^{-6}K^{-1}$

high modulus carbon/epoxy ($\eta = 3/5$)

$\alpha_{11} = -1.8 \times 10^{-6}K^{-1}$

$\alpha_{22} = 28.8 \times 10^{-6}K^{-1}$

Carpet plot

$[0/\pm 45/90]_s$

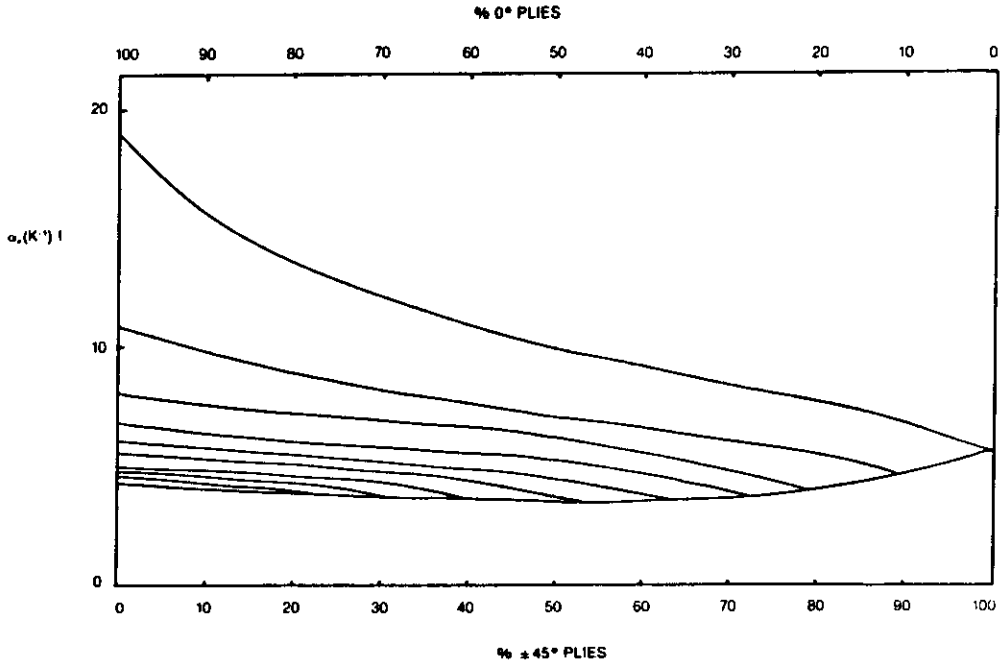

Figure 7.3. Linear coefficient of thermal expansion α_x for $[0/\pm 45/90]_s$ boron fiber/epoxy laminates.

Warping due to thermal expansion

need symmetrical and *balanced* laminate

Conditions for zero thermal expansion

sphere → ellipsoid

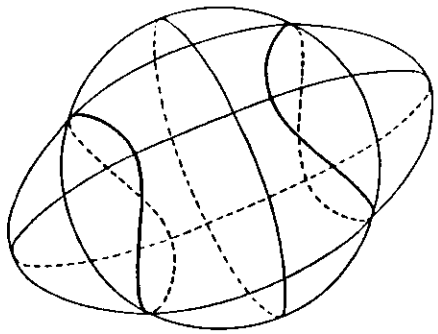

(a)

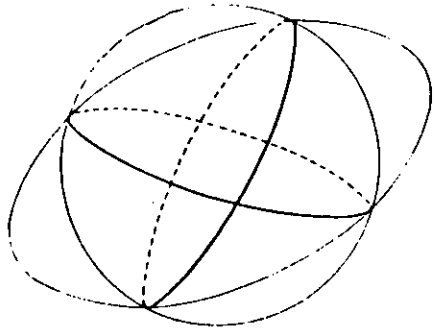

(b)

Figure 7.4. (a) Illustrating the general case of non-planar loops of intersection between a sphere and the ellipsoid to which it deforms. (b) The special case where one principal strain is zero.

lines that do not change their lengths

lines which end up as radii to the loops of intersection, may have come from other radii within the sphere

if one principal strain is zero, the loops of intersection are circles and we now have planes of zero expansion

two conditions for this

$$\epsilon_1\epsilon_2 \leq 0$$

$$\epsilon_3 = 0$$

Printed circuit boards

wave soldering

260°C

multi-layer circuit boards (MLB)

plated-through holes

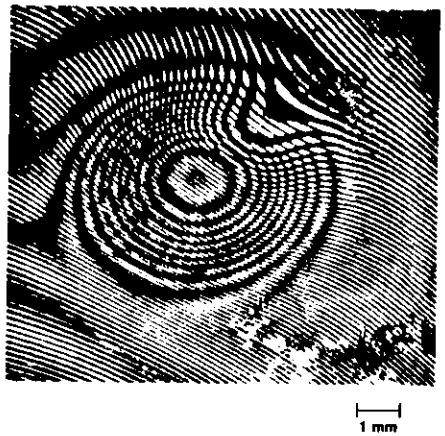

Figure 7.5. Development of the displacement field around a plated-through hole in a multi-layer circuit board during a 3 s soldering operation (after D. A. Tessell).

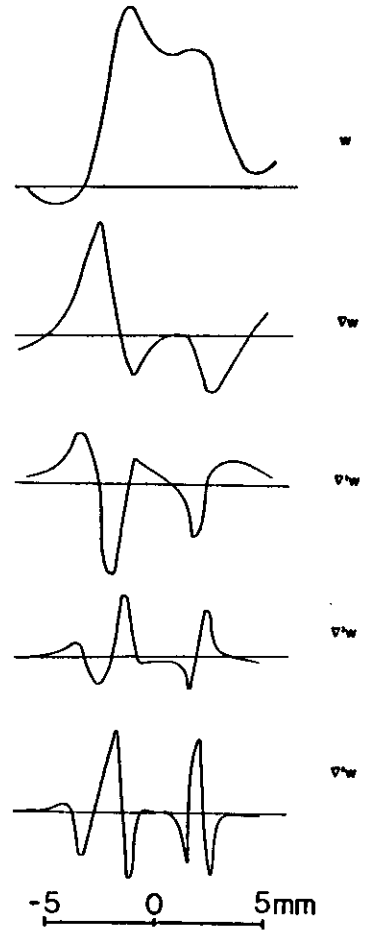

Figure 7.6. Normal displacement w across a diameter of the pattern of interference fringes seen in Figure 7.5, and the first four differentials of w.

ermal cycling of metal matrix and ceramic matrix composites

Fracture and fracture mechanics

Fundamental criticisms of critical stress and critical strain to failure criteria

Griffith's solution to the dilemma

"if the system can pass from the unbroken to the broken condition by a process involving a continuous reduction in overall *work done*, then the equilibrium state must be one in which fracture has occurred"

$$\frac{\partial}{\partial c}\,\Delta W_{\text{overall}} \leq 0$$

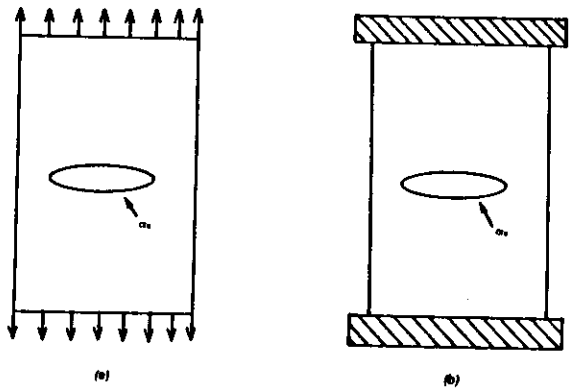

(a) (b)

Figure 8.1.

constant forces

$$\frac{1}{2}\int_0^{2\pi}\frac{u_a}{h}\ \sigma_{aa}d\beta + \frac{1}{2}\int_0^{2\pi}\frac{u_a}{h}\ \sigma_{ab}d\beta$$

plate *gains* energy

$$\Delta W_{\text{material}} = \frac{(p+1)\pi c^2\sigma^2}{8\mu}$$

strain energy density equals half the work done

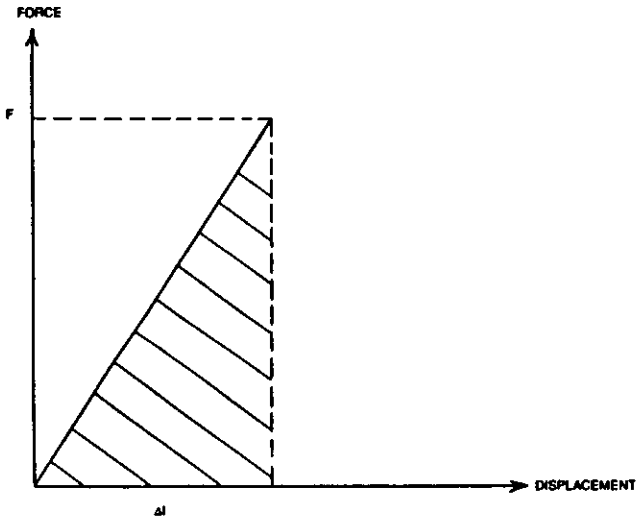

Figure 8.2.

$$(p+1)\pi c\sigma^2 = 16\mu\gamma$$

tensioned between fixed grips

plate *loses* energy!

external forces do no work since they don't move

$$(p+1)\pi c\sigma^2 = 16\mu\gamma$$

Griffith strength

$$\sigma = \sqrt{\frac{2E\gamma}{(1-\nu^2)\pi c}} \qquad \text{plane strain}$$

$$\sigma = \sqrt{\frac{2E\gamma}{\pi c}} \qquad \text{plane stress}$$

critical Griffith crack length

NDE

Statistical concepts

Weibull

"risk of fracture"

$$\phi(\sigma) = \left(\frac{\sigma}{\sigma_0}\right)^M$$

Two statistical distributions pertaining to fiber bundles

listribution of fiber strength

listribution of fiber slack

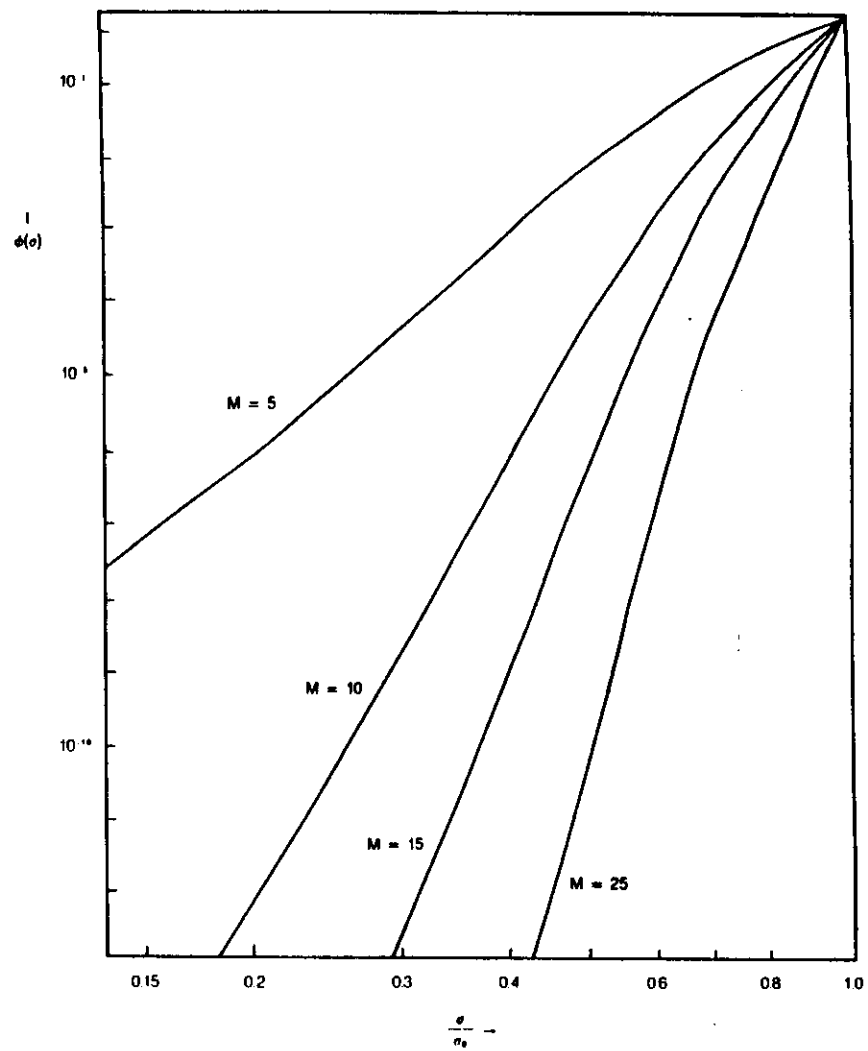

Figure 8.4.

$$\frac{\partial}{\partial c}\left[\frac{-(p+1)\pi c^2\sigma^2}{8\mu} + 4c\gamma\right] = 0$$

Irwin

strain energy release rate $\mathcal{G}$

$$\mathcal{G} = 2\gamma$$

LEFM

$$\Delta u = \frac{\mathcal{K}_I}{\sqrt{2\pi}}\sqrt{r}\,\frac{8(1-\nu^2)}{E}$$

stress intensity factor $\mathcal{K}$

$$\mathcal{G}_I = \frac{\mathcal{K}_I}{E}(1-\nu^2)$$

fracture toughness

toughest laminates are the symmetric cross-plies

thermoplastics are tougher than thermosets

where does the strain energy (that is released during fracture) come from?

in a composite, where (mainly in the fibers or mainly in the matrix) is the strain energy stored?

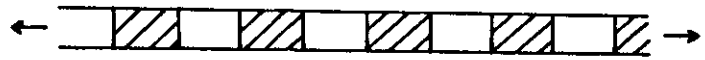

(a)

Figure 8.5a. Maxwell element.

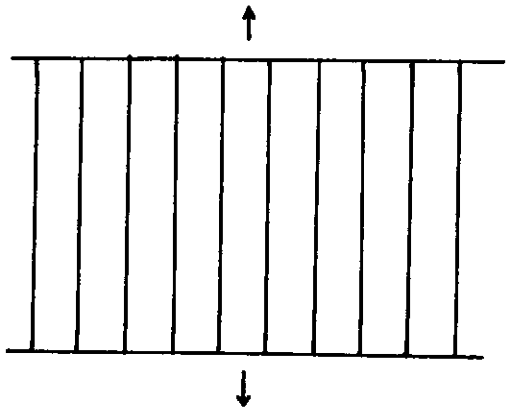

(b)

Figure 8.5b. Voight element.

and where in the case of an adhesive joint?

Origins of toughness

$$\mathcal{G} = 2(\gamma + \gamma_{plastic})$$

The meaning of toughness is possession of some physical mechanism(s) for rendering cracks non-disastrous

Polymers – configurational entropy, crack-bridging by pulled-out molecules

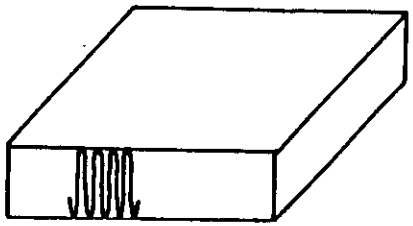

Figure 8.6. Illustrating a polymer lamella single crystal. In polyethylene, the fold length contains about 100 carbon atoms.

metals – dislocation generation, multiplication and entanglement

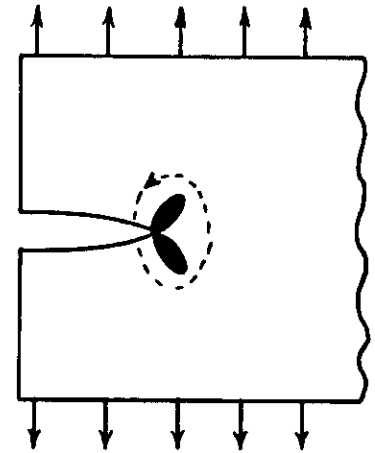

Figure 8.7. The yielded zone, ahead of a crack, responsible for the toughness of metals.

ceramics—free space

fiber reinforced materials—matrix mechanisms, fiber pull-out

Figure 8.36. Fiber pull-outs and sockets created during tensile fracture of glass fiber reinforced epoxy resin (after A. Kelly).

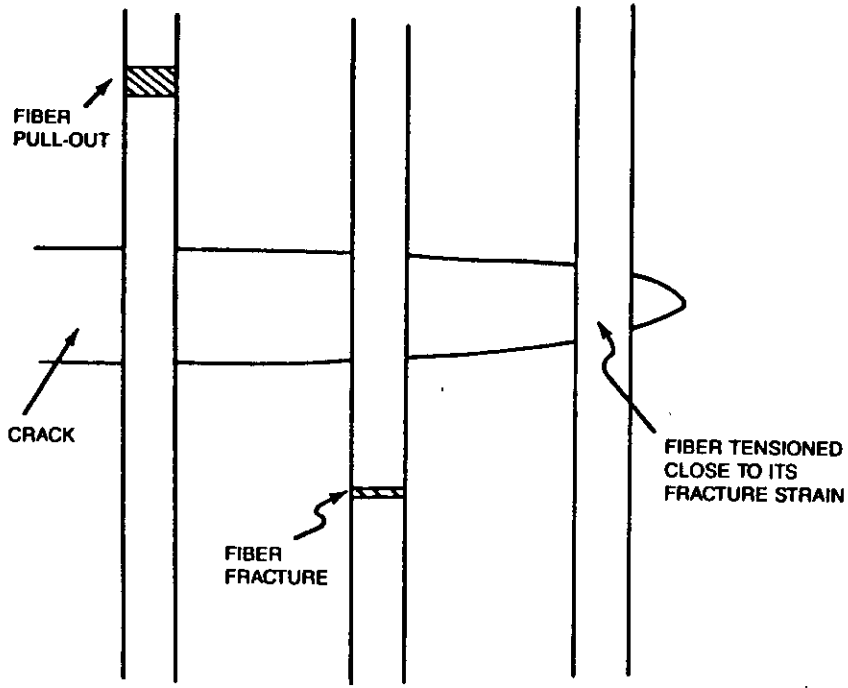

Figure 8.37. Fibers bridging a crack.

$$P = P_f \frac{\sin h\sqrt{a}\, x}{\sin h\sqrt{a}\, \frac{l}{2}}$$

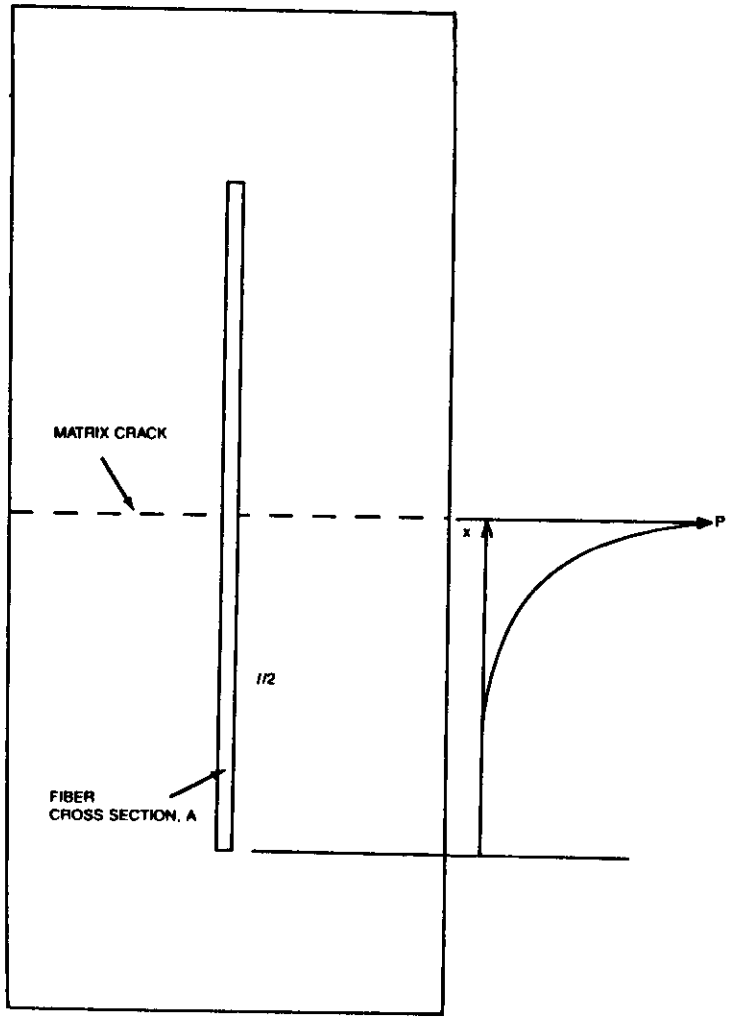

Figure 8.11. Illustrating fiber pull-out.

rubber toughened epoxies

metal toughened ceramics

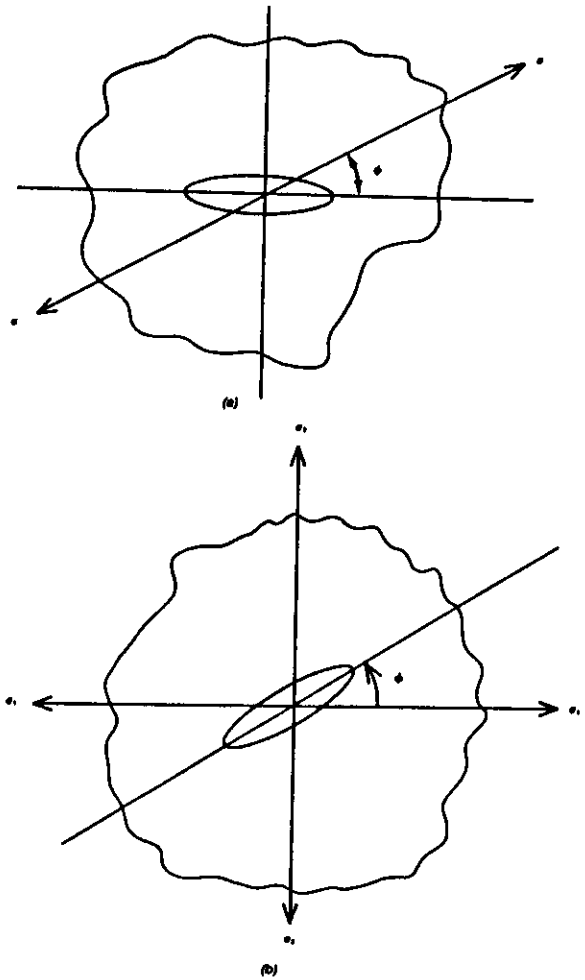

Figure 8.13.

$$\sigma_{\alpha\alpha} = \frac{(\sigma_1 + \sigma_3)\sinh 2\alpha_0 + (\sigma_1 - \sigma_3)[e^{2\alpha_0}\cos 2(\phi - \beta) - \cos 2\phi]}{\cosh 2\alpha_0 - \cos 2\beta}$$

stress criterion is differentially related to Griffith's energy criterion

$$\sigma = 2\frac{dU}{dA}$$

as soon as it has any shear acting on it, a crack changes direction

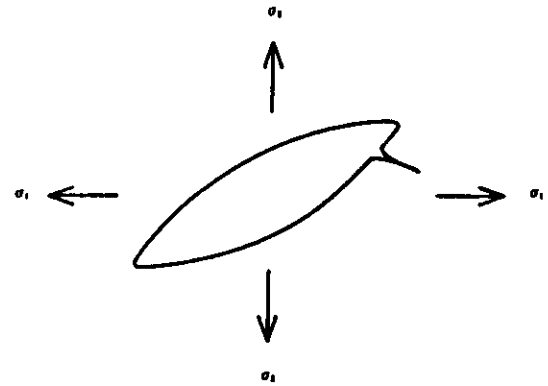

Figure 8.16. Crack propagation from the surface of an elliptic hole (pre-existing crack) in a plate subjected to biaxial stress.

wo fracture criteria

(i) $3\sigma_2 + \sigma_1 > 0$, fracture if $\sigma_1 > K$ and $\phi = 0$

(ii) $3\sigma_2 + \sigma_1 < 0$, fracture if $(\sigma_1 - \sigma_3)^2 + 8K(\sigma_2 + \sigma_3) = 0$

$$\text{and } \cos 2\phi = -\frac{1}{2}\frac{(\sigma_1 - \sigma_3)}{(\sigma_2 + \sigma_3)}$$

cture in torsion

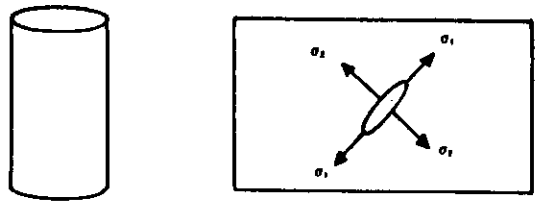

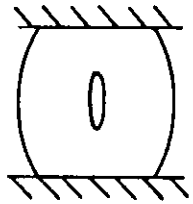

Figure 8.30. (a) Brittle failure in torsion. (b) Longitudinal failure in uniaxial compression between unlubricated platens. (c) Fiber buckling modes in uniaxial composite subject to uniaxial compression parallel to the fiber direction.

compresson strength is eight times tensile strength

fracture in pure shear with superposed hydrostatic pressure

bi-stability of fracture under combined tension and shear

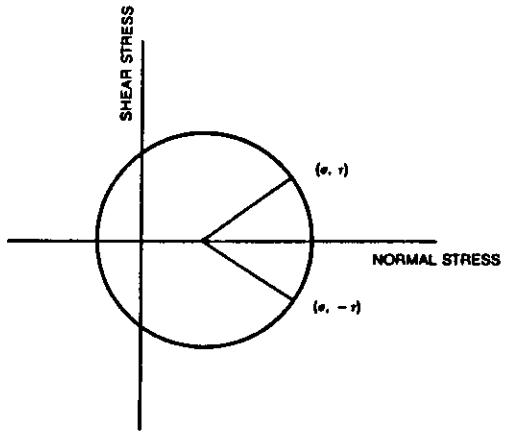

Figure 8.32.

$G \propto \sigma^2 + \tau^2$

fracture modes, I, II, III

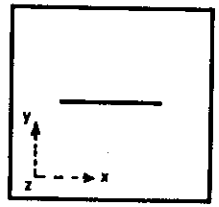

(a)

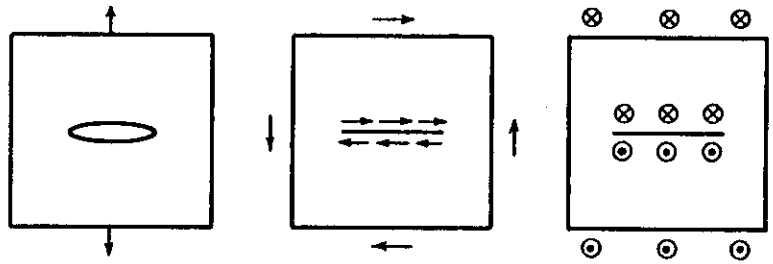

(b)

Figure 8.9. (a) Plate containing a crack, (b) the crack in (a) could be opened by any of the three systems of forces shown here.

fracture surface energy is different for modes I, II, III

rustrated atoms

Drowan's failure envelope

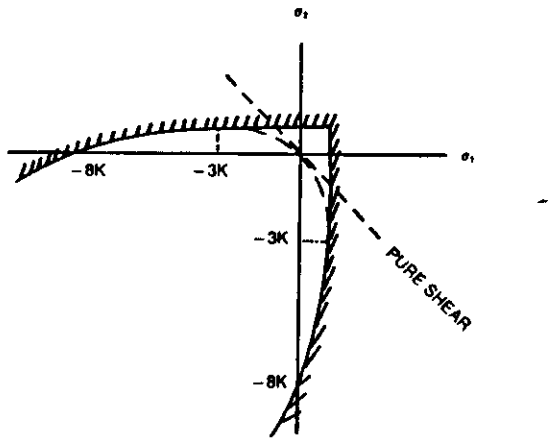

Figure 8.17. Failure envelope for the propagation of a Griffith crack in two-dimensional stress fields. Note that the envelope is open in the compression-compression quadrant.

o physical justification for *closed* failure envelopes

Figure 8.18. Cone extracted from a Hertzian crack in quartz (after J. W. Heavens).

fracture in strongly inhomogeneous stress fields

Auerbach's law

$$\frac{P_c}{r} = \text{constant}$$

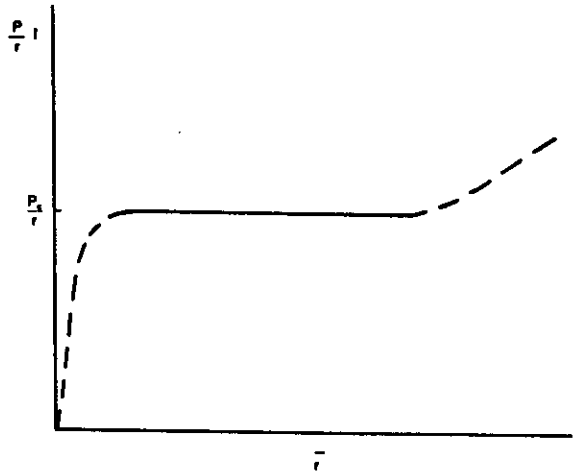

Figure 8.19. Relationship between normal force P and radius r of a spherical indentation.

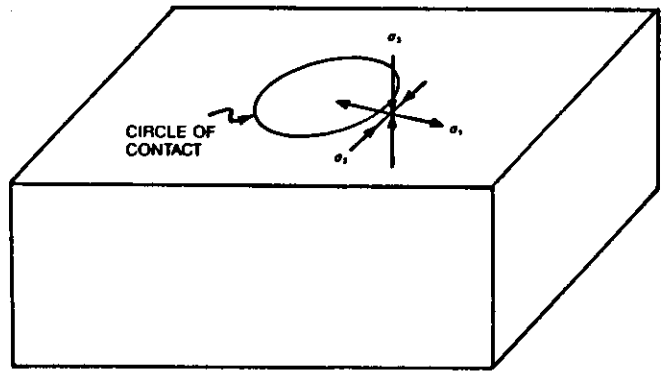

(a)

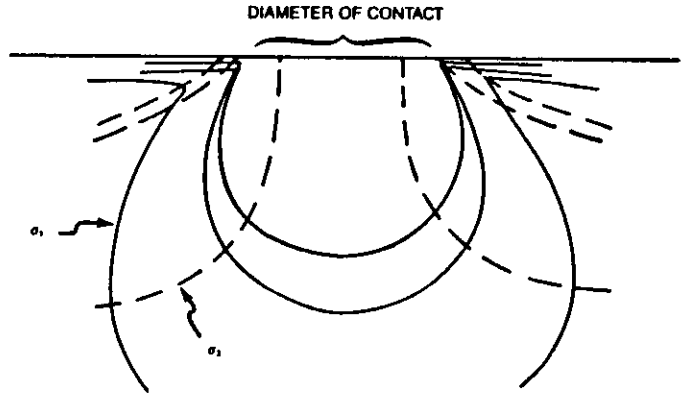

(b)

Figure 8.20. (a) Hertzian stress field. Directions of principal stress just outside circle of contact. (b) Full lines are contours of constant σ_1. Broken lines indicate the direction of σ_3.

pact damage

fficient of restitution

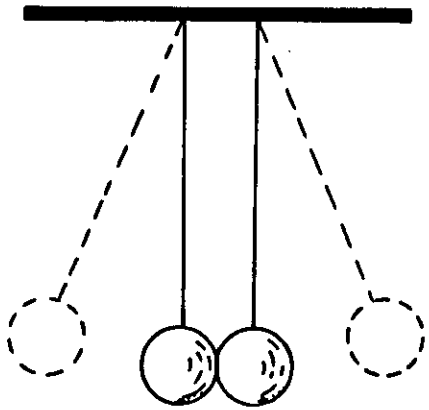

Figure 8.23. Newton's coefficient of restitution experiment.

$$U - V = e(v - u)$$

yield beneath a Hertzian indenter

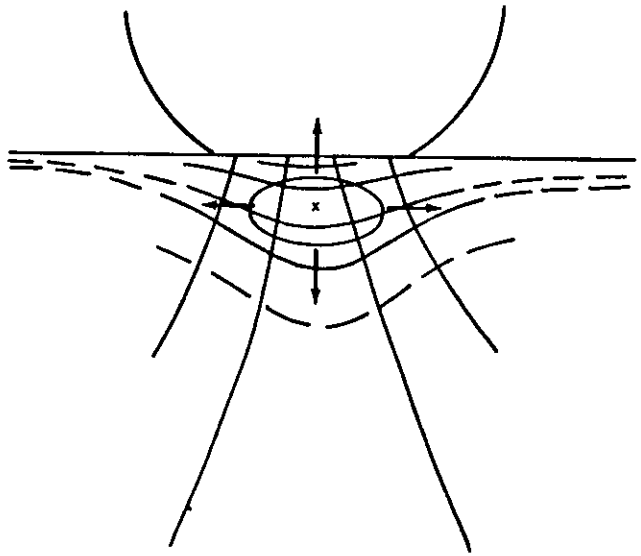

Figure 8.24. Modification of the Hertzian stress field by yield beneath the indentor. Continuous lines denote contours of constant compressive stress, broken lines contours of constant tensile stress.

densification beneath a Hertzian indenter

delamination beneath a Hertzian indenter

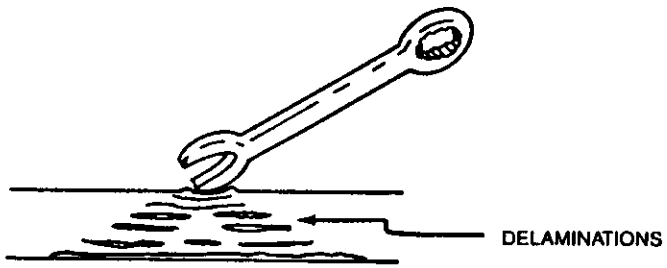

Figure 8.25. Internal delamination damage. The impacted surface may reveal no sign of the damage. The far surface may show signs of damage but is often inaccessible.

reduction in in-plane compression strength after impact

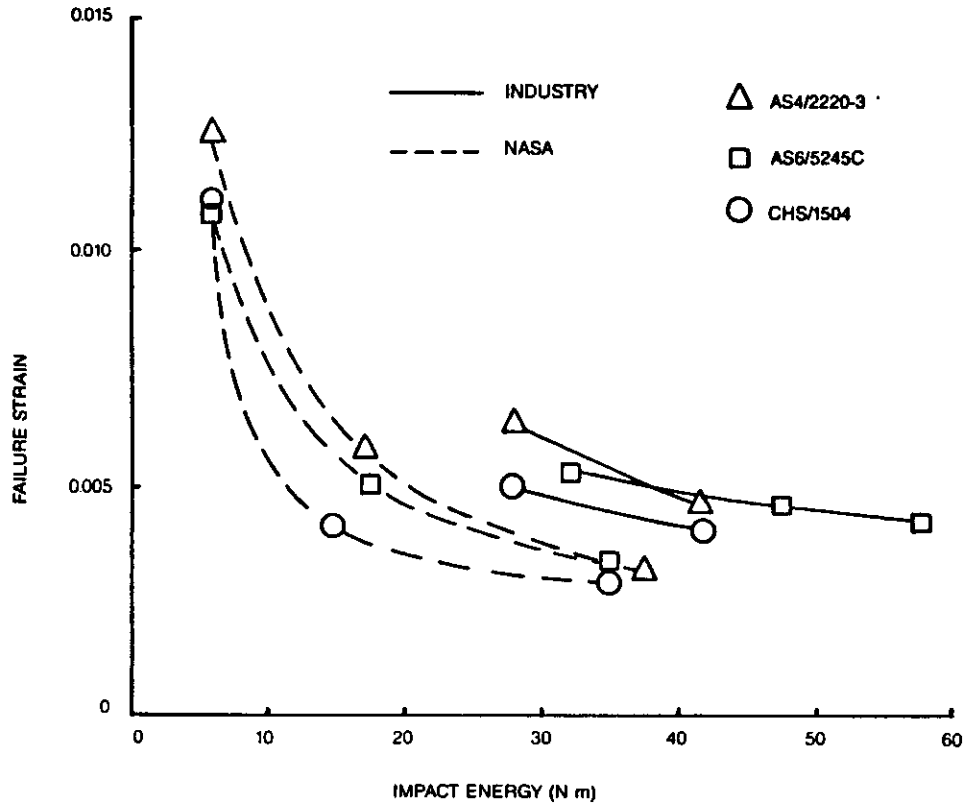

Figure 8.26. In-plane compressive strain to failure after impact (after J.C. Halpin).

stitching

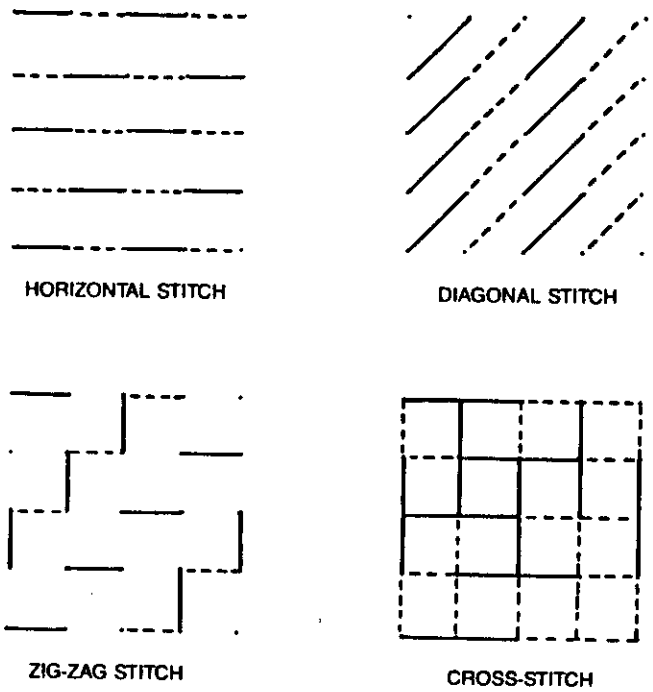

Figure 8.27. Examples of stitching patterns used to guard against delamination by impact.

impact at ballistic velocities

Erosion

cavitation

water erosion

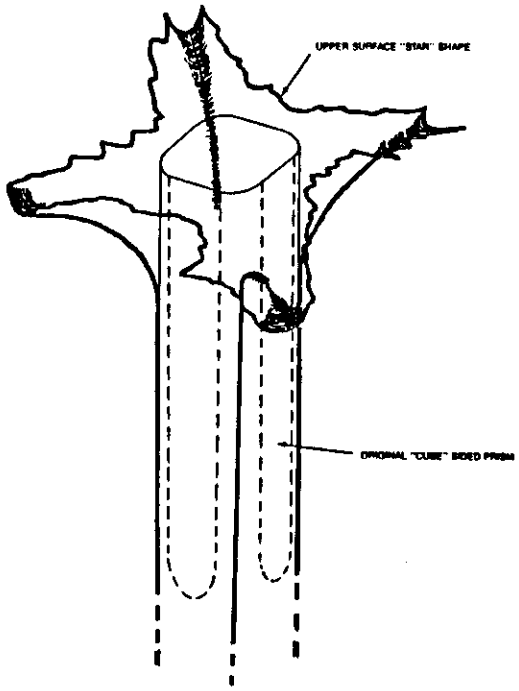

Figure 8.28. Illustrating cavity erosion.

hammering

solid particle erosion

Ablation

fiber creasing in carbon/carbon composites

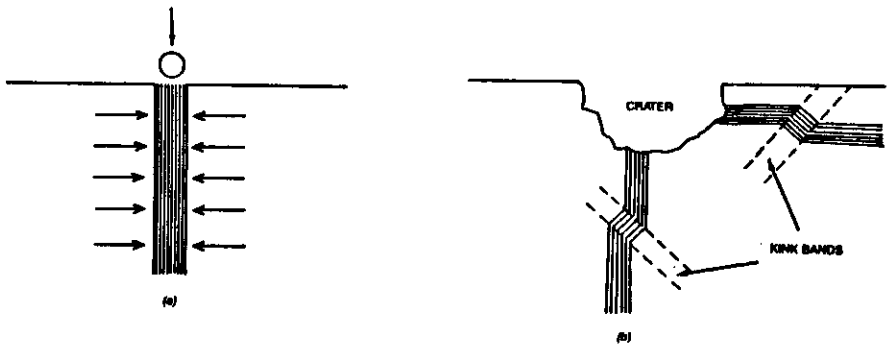

Figure 8.29.

stress cracking in polymers

sub-critical crack growth

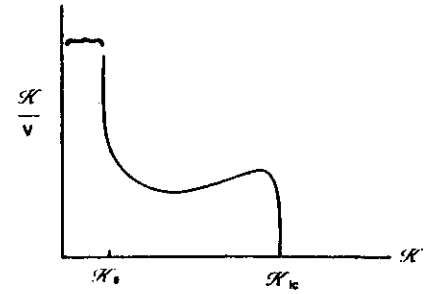

Figure 8.33. Graphical representation of the integral $\int \frac{\mathscr{K}}{V} d\mathscr{K}$.

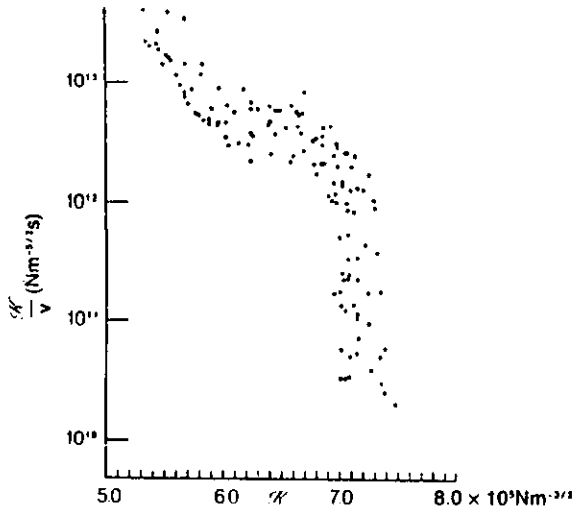

Figure R.34.

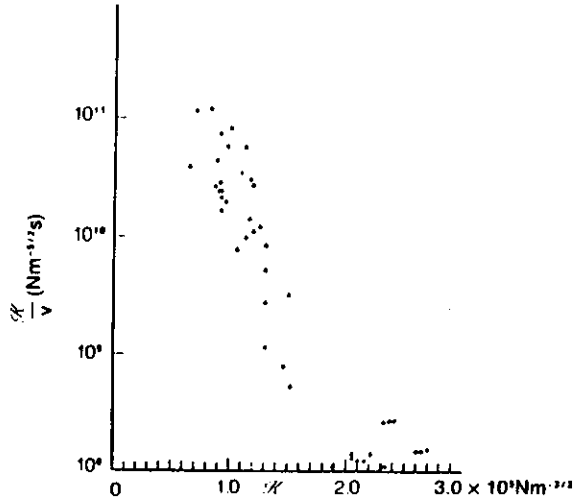

Figure R.35. $\mathscr{K}/v$ versus $\mathscr{K}$ data for mode III fracture of soda lime glass (after D.A. Tossell).

$$\mathscr{K} = \sigma(\pi a)^{1/2}$$

$$t = \frac{2}{\pi\sigma^2}\int_{\mathscr{K}_0}^{\infty}\frac{\mathscr{K}}{v}\,d\mathscr{K}$$

Airy stress functions

$$\sigma_{xx} = \frac{\partial^2 \chi}{\partial y^2}; \qquad \sigma_{yy} = \frac{\partial^2 \chi}{\partial x^2}$$

$$\sigma_{xy} = \sigma_{yx} = -\frac{\partial^2 \chi}{\partial x \partial y}$$

two-dimensional stresses

loaded cantilever beam

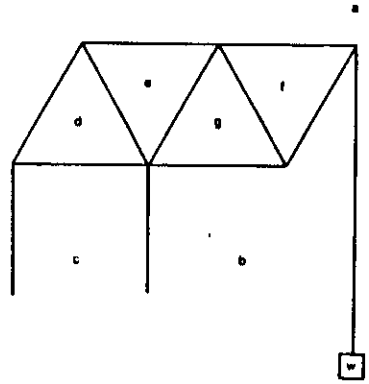

Figure 9.1. Loaded cantilever beam.

$$\int_a^a \sigma_{yy}\,dx = W$$

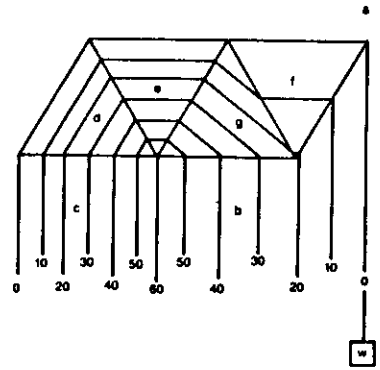

Figure 9.2. Contours of constant χ in the air between the members of Figure 9.1.

ensioned cross-bow

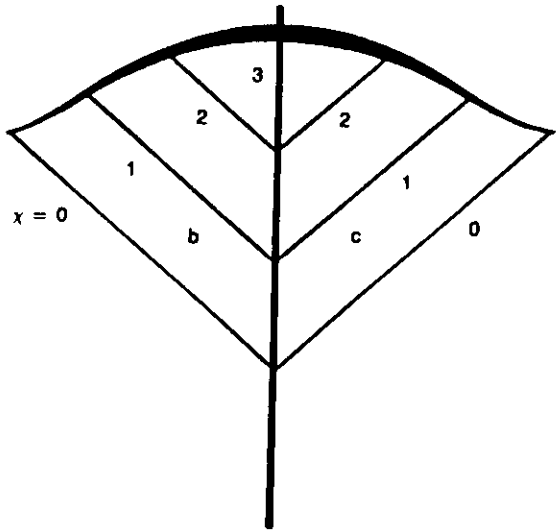

a

Figure 9.3. Tensioned cross-bow.

a

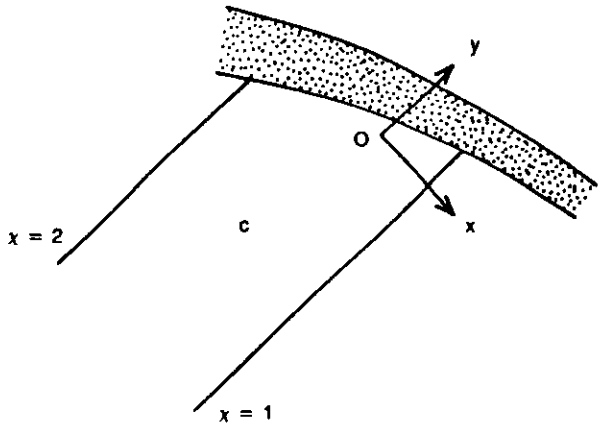

Figure 9.4. Detail from Figure 9.3. Axis Oy is parallel to the χ contours.

$$M_{OP} = \chi_0 - \chi_P$$

curved beam subjected to bending moment tending to straighten it

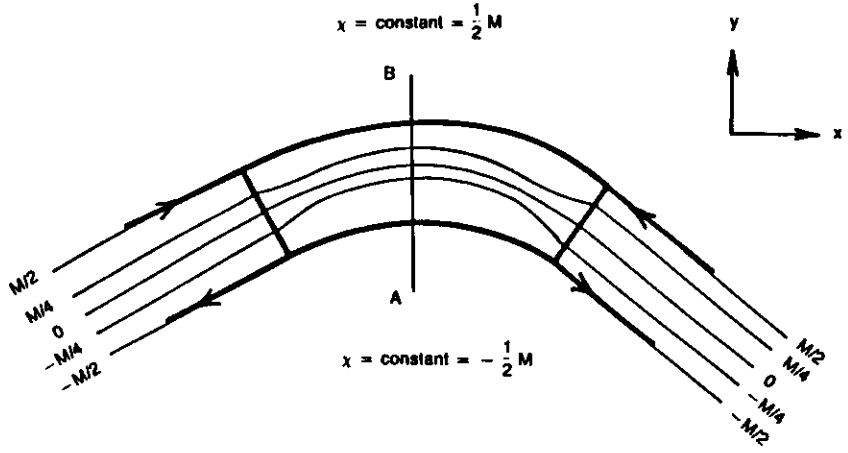

Figure 9.5. χ-map for a uniformly curved beam with a uniform bending moment M tending to straighten it.

$$\sigma_{zz} = \left(\frac{h}{4r_o}\right)\sigma^{\text{[illegible]}}$$

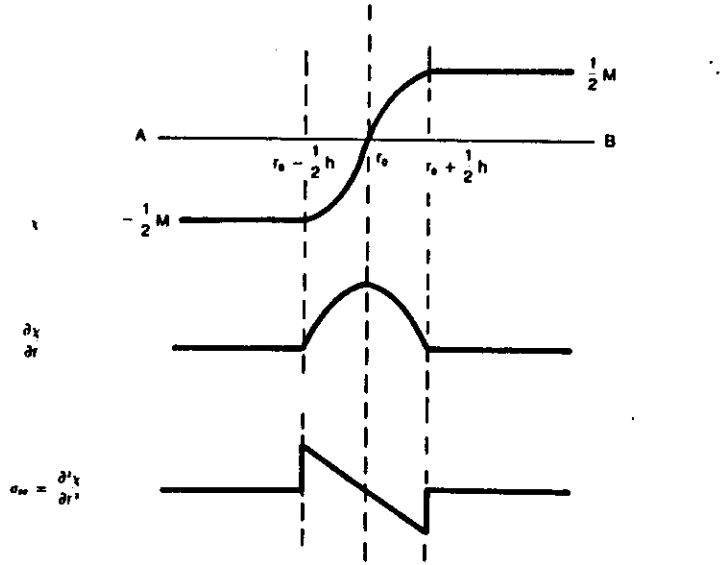

Figure 9.6. Variation through the thickness at AB in Figure 9.5 of χ and its first and second differentials.

thru thickness tensile strength

4%

(a)

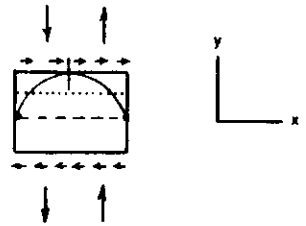

(b)

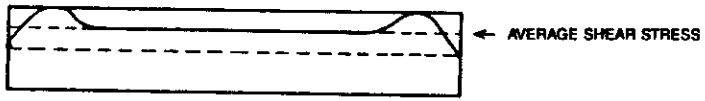

(c)

Figure 9.9 Longitudinal distribution of interlaminar shear stress.

stribution of mid-plane shear stress

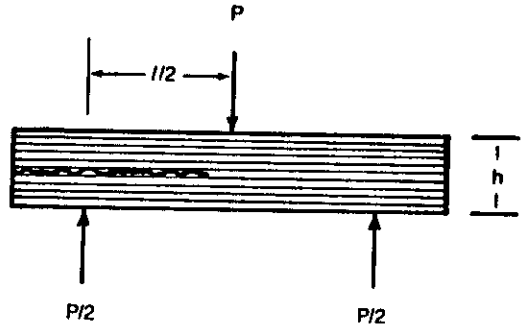

Figure 9.10. ASTM D-2344 short beam shear test-piece $l/h = 4$.

$$\tau = \frac{3P}{4bh}, \text{ where } \frac{l}{h} = 4$$

Airy stress function in the air for deep three point bending

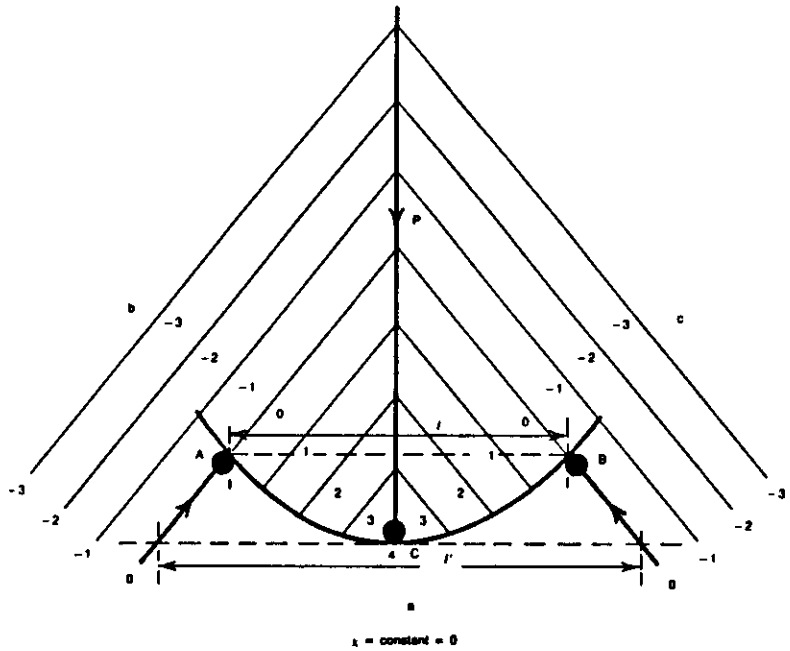

Figure 9.11. Airy stress function in the air χ-diagram for deep three-point bending (χ-scale arbitrary).

$$M = \frac{Pl'}{4} \cdot \text{where } l' > l$$

apparent dependence of interlaminar shear strength on fiber volume fraction

Delamination

$$a > b > c$$

theory of propagation of shear cracks

$$\frac{b}{\varrho} = \left(\frac{\tau_{\text{critical}}}{2\tau_0} \right)$$

transition to fast delamination

$$dG \sim \frac{(2ab\,db + b^2 da)\tau_0^2}{\mu}$$

junction of delaminations

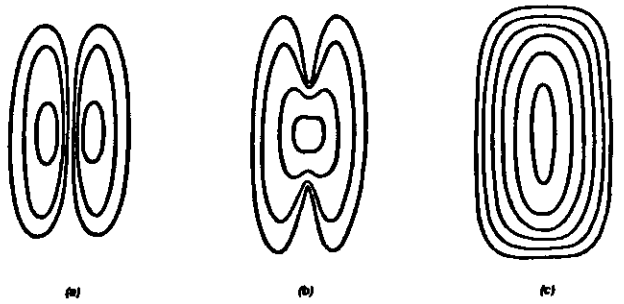

Figure 9.12. Showing the junction of two delaminations meeting side by side in the same plane.

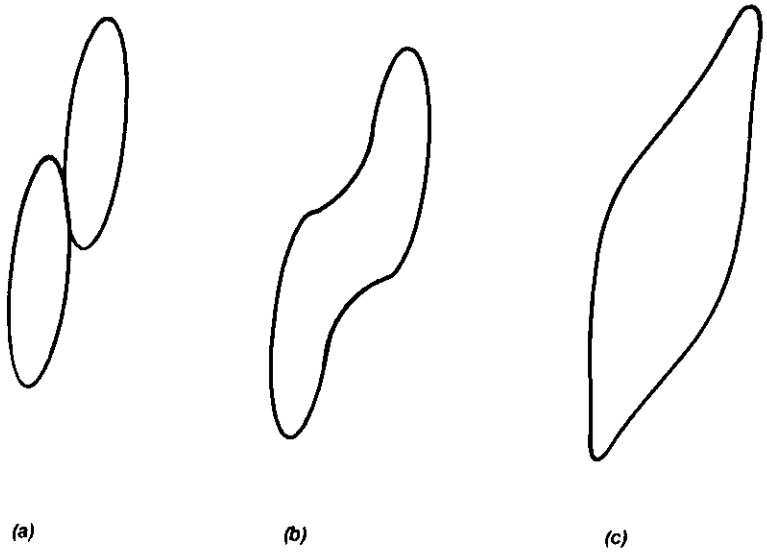

Figure 9.13. Union of two delaminations which are not exactly side by side or end to end.

$$d\mathcal{G} \sim \frac{2ab^2\tau_0^2}{\mu}$$

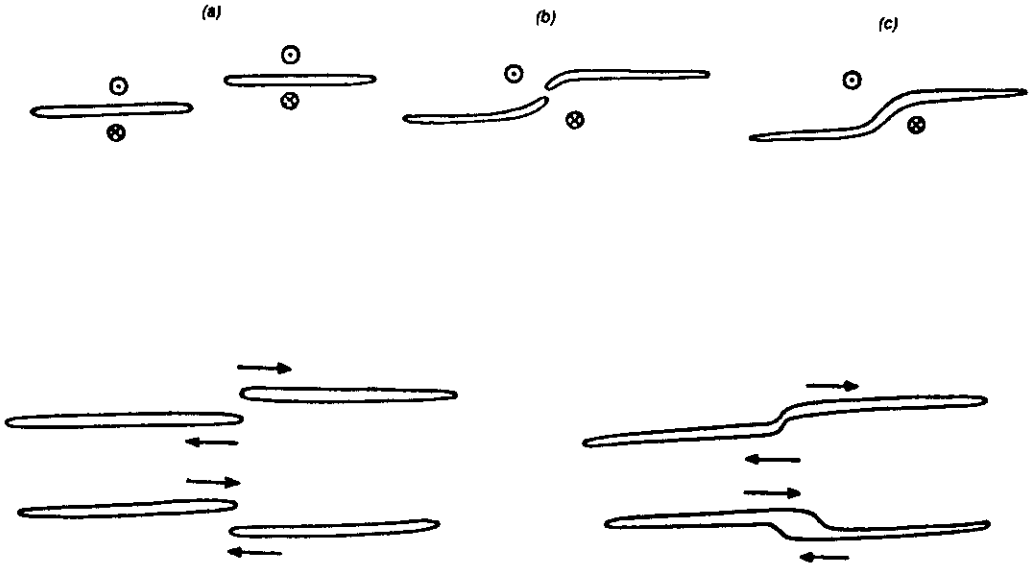

Figure 9.14.

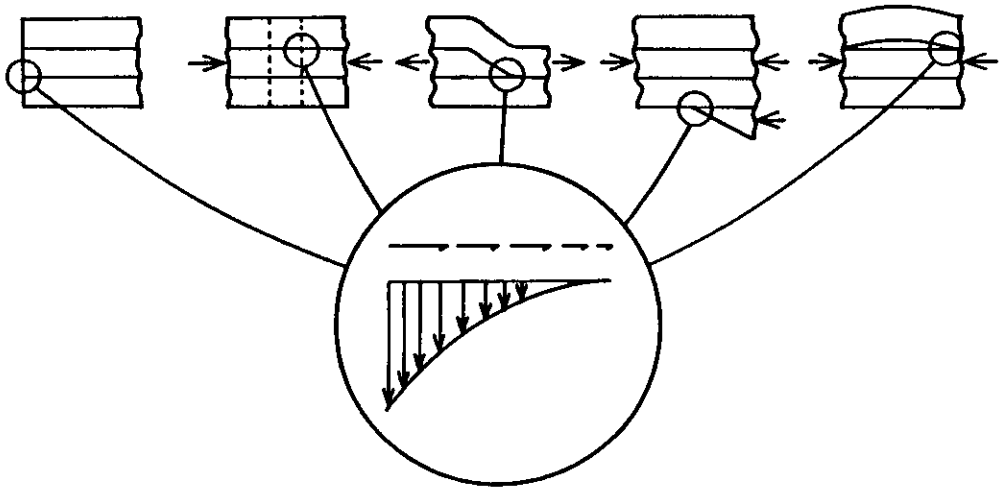

Figure 9.15. Sources of out-of-plane stresses (after K.T. Kedward).

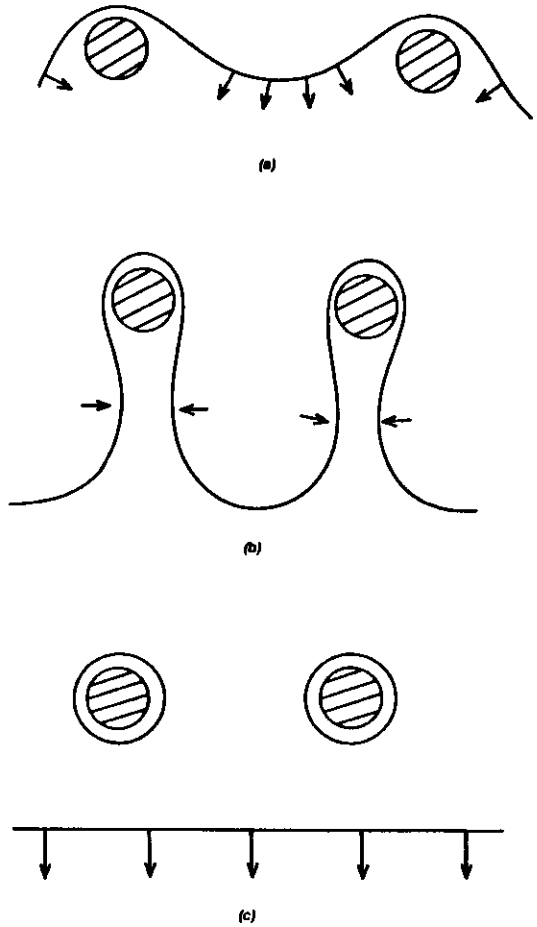

Figure 9.16. (a) A dislocation, gliding from top to bottom, begins to bow out between two fibers. (b) The segments of dislocation line with opposite sign begin to attract each other (arrowed). (c) The dislocation escapes leaving an Orowan loop around each fiber.

$$\frac{dD}{dN} \propto (\sigma_m)^{3.71}$$

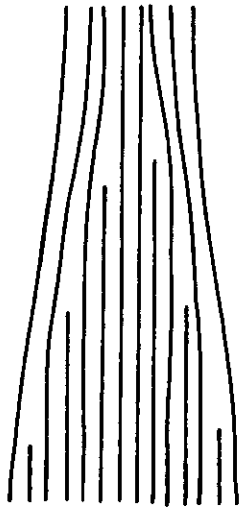

Figure 9.18. Illustrating ply drops in a tapered laminate.

Hostile environments

Degradation in the Earth's atmosphere

UV degradation

10μm

corrosion of metal matrix composites

Swelling due to water uptake

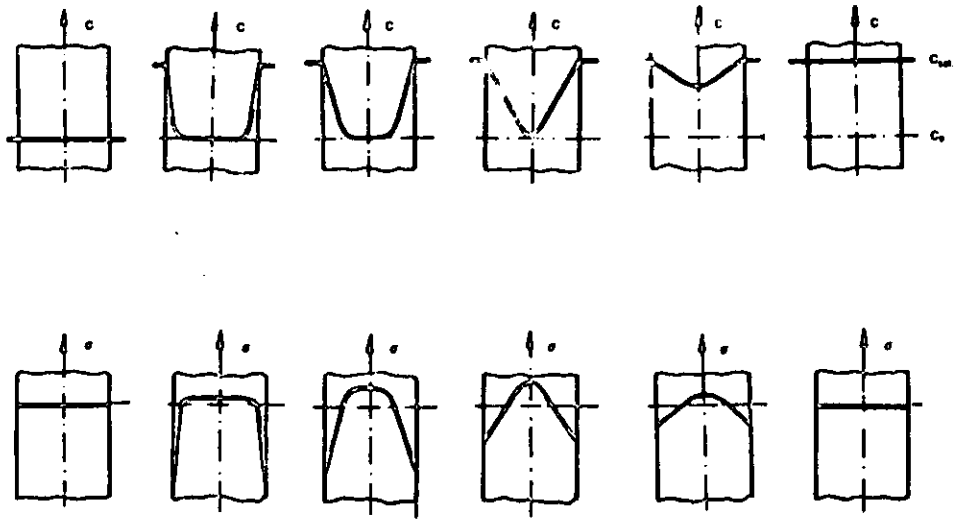

Figure 10.1. Water uptake through the thickness (upper row) and associated in-plane stress distribution (lower row) for a slab of neat resin, as a function of time of exposure to aqueous environment (after D. Putz).

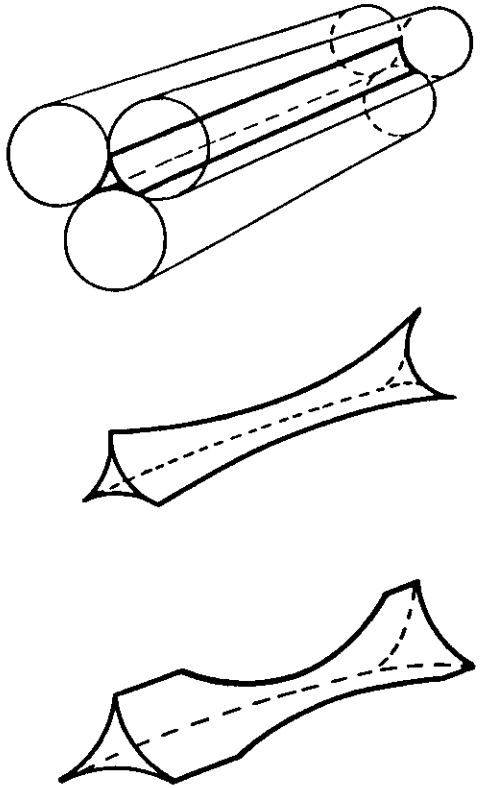

Figure 10.3. Dimensional changes that the resin between fibers would like to undergo during water uptake.

$$\frac{j_{\text{drift}}}{j_{\text{diffusion}}} \sim \frac{\Delta E}{kT}$$

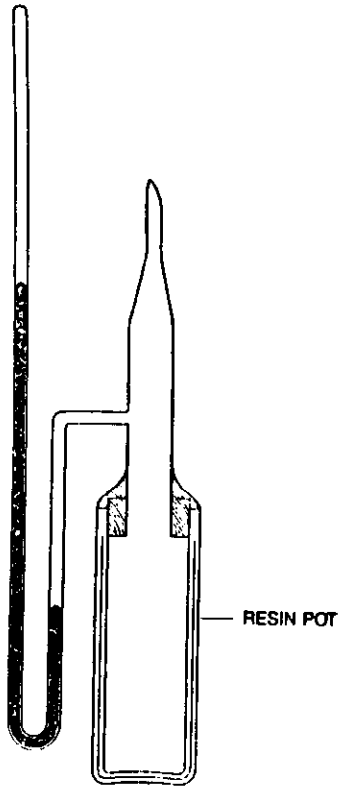

Figure 10.4.

$$P = \frac{RT}{V}$$

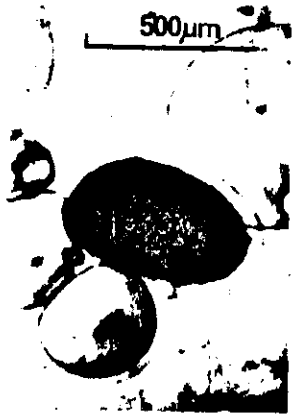

Figure 10.6. Transmission optical micrograph of disc-shaped cracks in neat polyester resin. Note the total internal reflection from the central (air-filled) portion of one of these cracks.

Figure 10.18. Polyester resin cracks accompanying debonding of fibers treated with a coupling agent. Specimens immersed in boiling water for 20 hours: (a) E glass, (b) C glass.

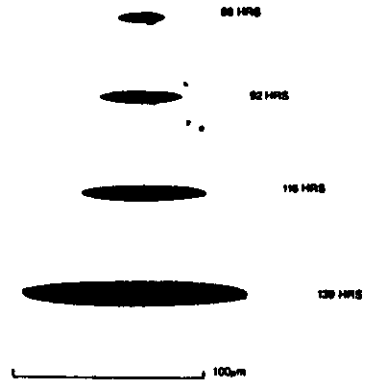

Figure 10.21(a). Edge-on view of growth of single penny-shaped crack ~ 0.2 mm below the surface in epoxy resin.

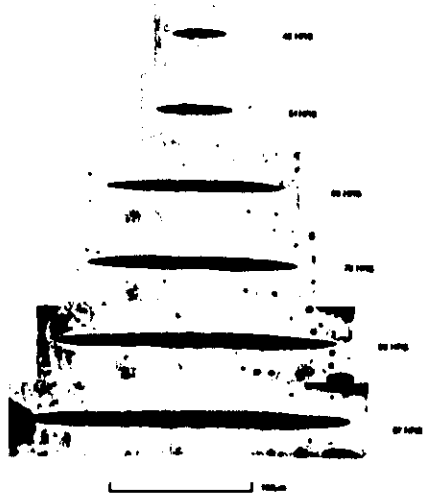

Figure 10.21(b). Edge-on view of growth of single penny-shaped crack ~ 0.2 mm below the surface in polyester resin.

equilibrium shape of pressure-filled voids

$$a^* = \frac{\pi E \gamma}{2(1 - \nu^2)p^2}$$

magnitude of osmotic pressures

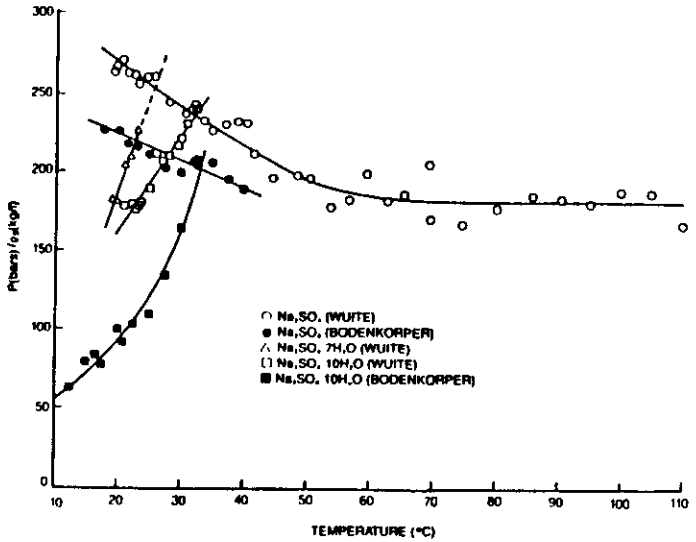

Figure 10.9. Osmotic pressures for solutions of Glauber's salt.

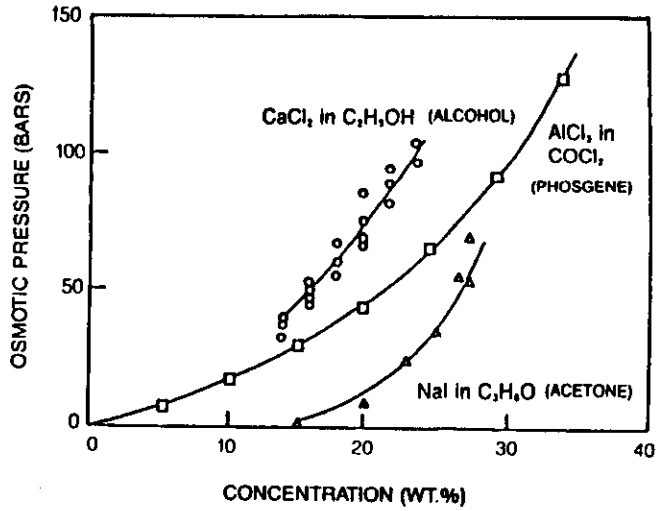

Figure 10.10. Osmotic pressures for solutions of inorganic salts in organic solvents.

— 500 bars

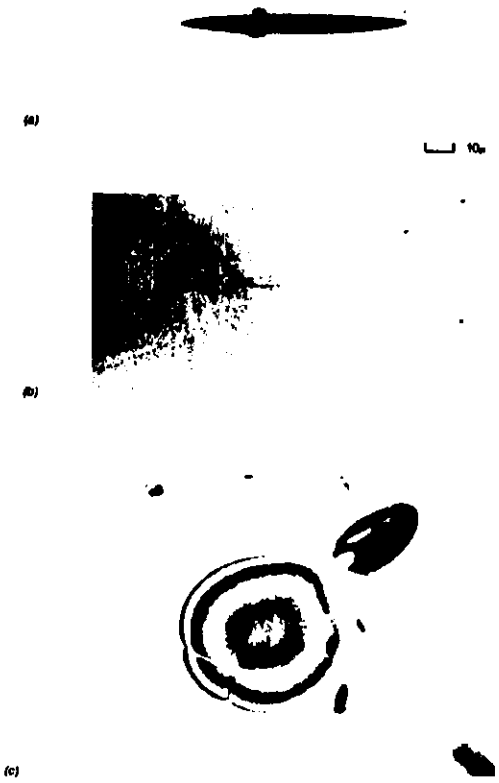

Figure 10.19. (a) Penny-shaped crack in KCl-doped epoxy resin photographed edge-on, 140 h immersion in water at 94 °C. (b) Same crack after drying in air for 1 h at 80 °C. (c) Face-on view after drying showing only three interference fringes, that is a permanent opening in the middle of the crack of only three half wavelengths.

$\mathscr{K}_I$ = 0.23 to 0.79 Mn m$^{-3/2}$

v = 5 pms^{-1} to 1 nms^{-1}

tection of loss of load transfer due to osmosis at fiber/matrix interface

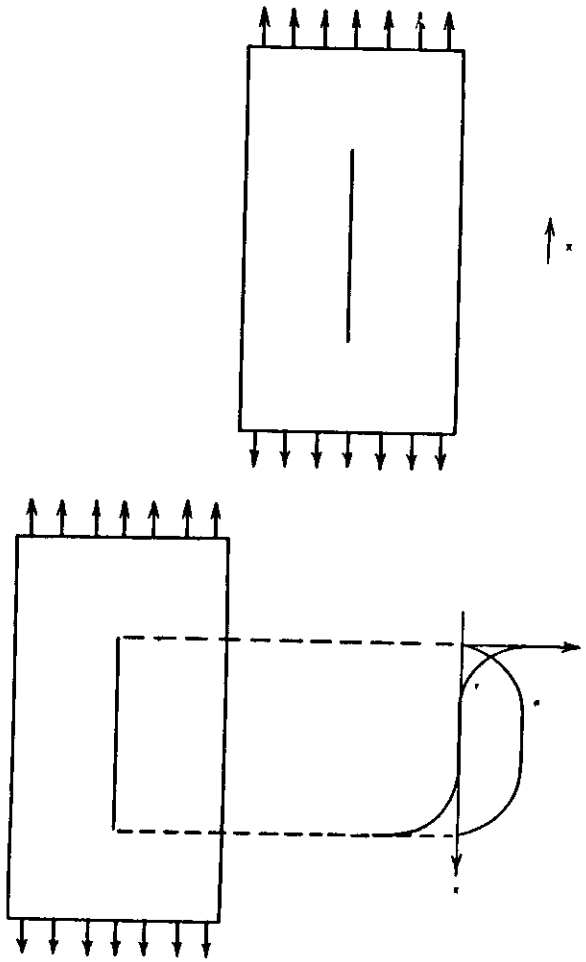

Figure 10.11.

$$\sigma = E_f e \left\{ 1 - \frac{\cosh \beta \left(\frac{l}{2} - z \right)}{\cosh \beta} \right\}$$

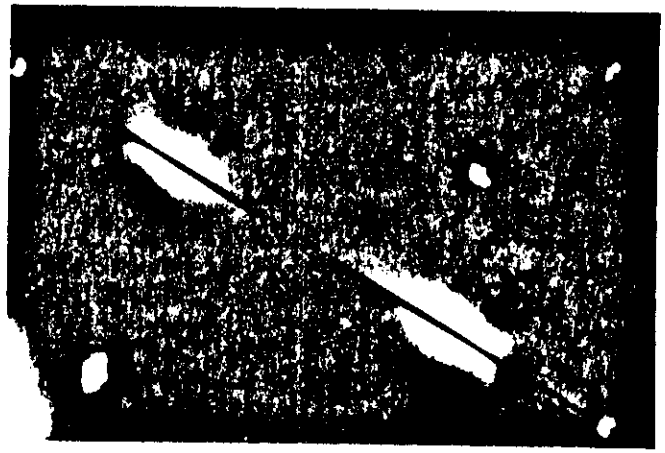

Figure 10.12. Graphite fiber in epoxy resin matrix after hot water exposure showing two regions of migrating resin birefringence (arrowed). Courtesy of E. Walter.

solutes responsible for osmosis

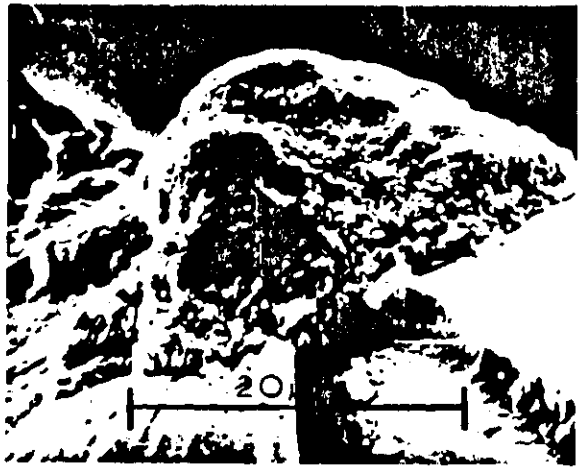

Figure 10.7. Impurity deposit left after drying, on one surface of a disc-shaped crack in polyester resin [50].

UCT TN-5400 Trials/Materials Engineering TUE 03-DEC-85 11:09
Cursor: 0.000keV = 0

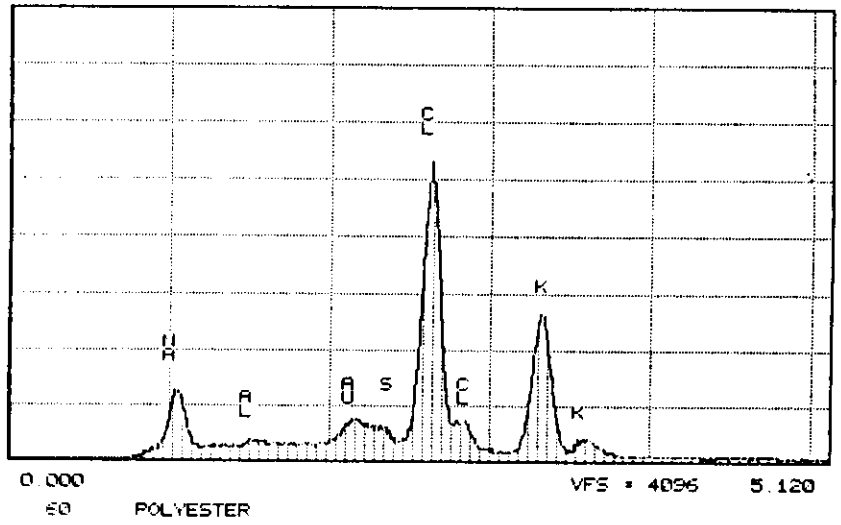

SETUP SSQ

SSQ: SSQ

SEMI-QUANTITATIVE ANALYSIS: POLYESTER
EL NORM. K-RATIO

NA-K 0.13111 +- 0.00184
K -K 0.33167 +- 0.00269
CL-K 0.53721 +- 0.00315

ZAF CORRECTION 15.00 KV 50.00 Degs

No. of Iterations 2

----	K	[Z]	[A]	[F]	[ZAF]	ATOM.%	WT.%	
NA-K	0.131	0.948	1.529	0.997	1.434	24.23	16.75	*
K -K	0.331	1.024	1.148	1.000	1.175	29.63	34.73	
CL-K	0.537	1.004	1.031	0.978	1.014	46.13	48.52	

* - High Absorbance

Figure 10.8. Energy dispersive analysis of the deposit shown in Figure 10.7.

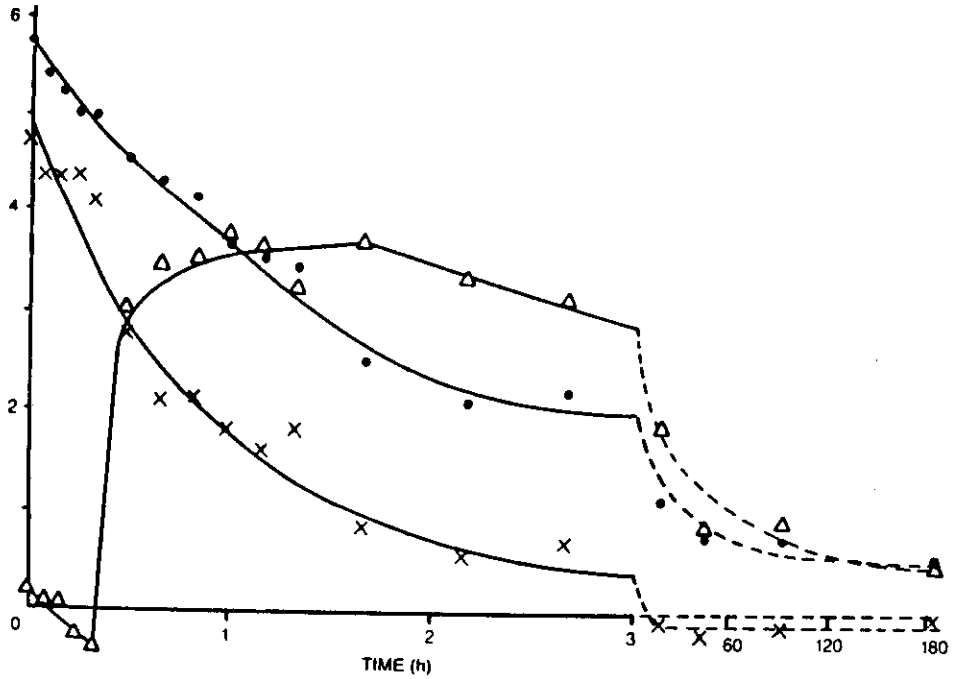

Figure 10.14. Optical retardation changes during immersion in water at 20°C. Untreated E glass fiber in polyester resin. × load transfer index, . . . retardation in resin adjacent to fiber ends, ● retardation through fiber center.

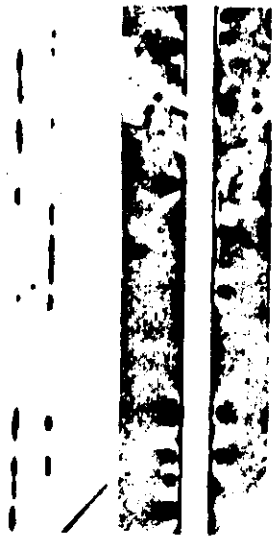

Figure 10.17. Transmission optical micrographs showing discontinuous debonding of an E glass fiber treated with a coupling agent: (a) ordinary light, (b) between crossed polaroids with compensator set to enhance the difference in birefringence.

Clapeyron's equation

$$\frac{dp}{dT} = \frac{\Delta S}{\Delta V}$$

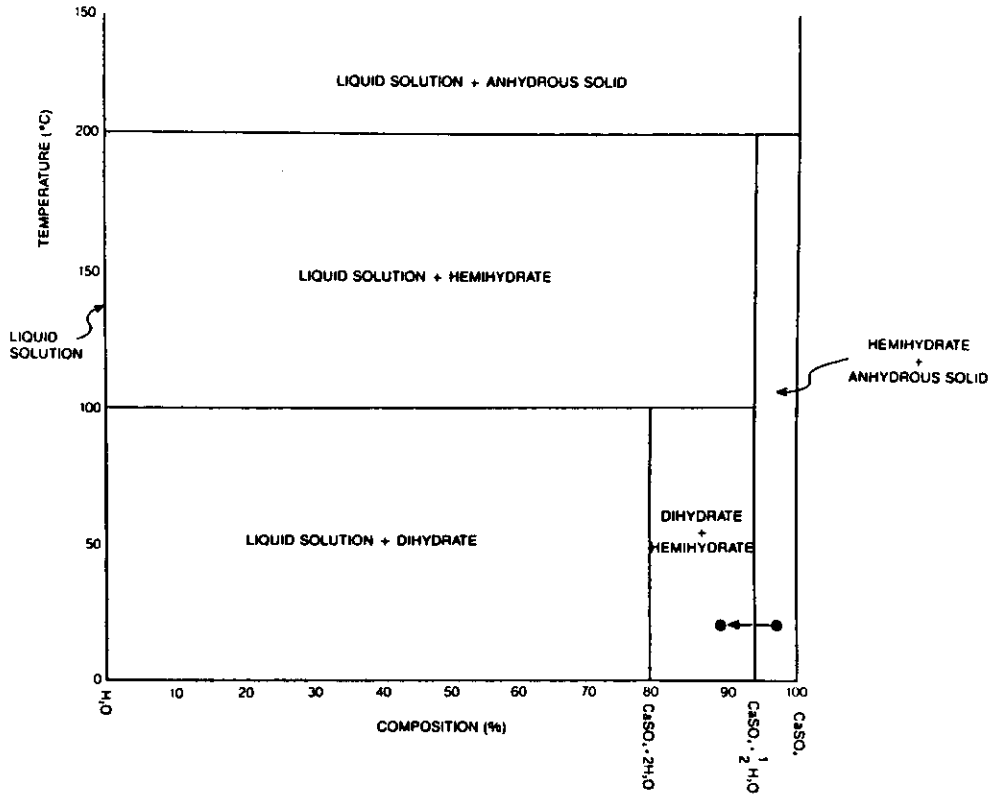

Figure 10.22. Equilibrium diagram for the system H_2O-$CaSO_4$.

timation of water of hydration pressures at impurity inclusions

~ 500 bars

t heaving

$p \sim 270$ bar at $-20°C$

behavior of water occlusions during thermal spike

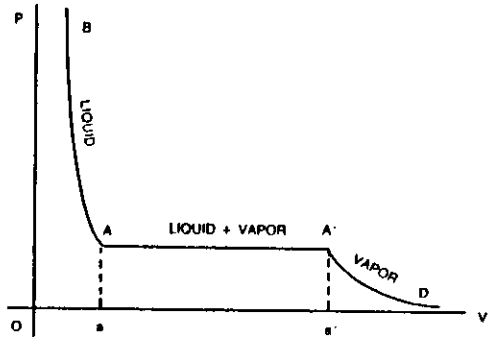

Figure 10.23.

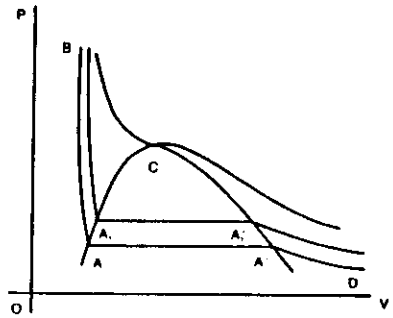

Figure 10.24.

silane coupling agents

Figure 10.25. Growth of indentation cracks following debonding of short fibers. Untreated E glass fiber/polyester resin composite [52].

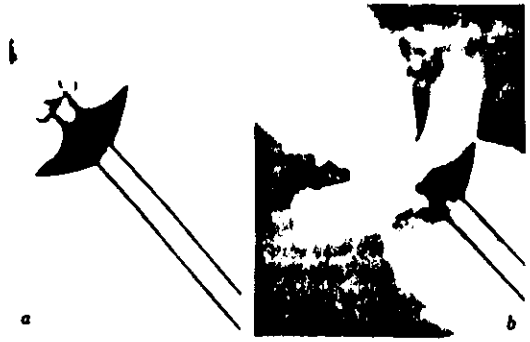

Figure 10.26. Transmission optical micrographs of indentation cracking: (a) ordinary light, (b) between crossed polaroids showing high birefringence in adjacent resin due to extensive plastic deformation.

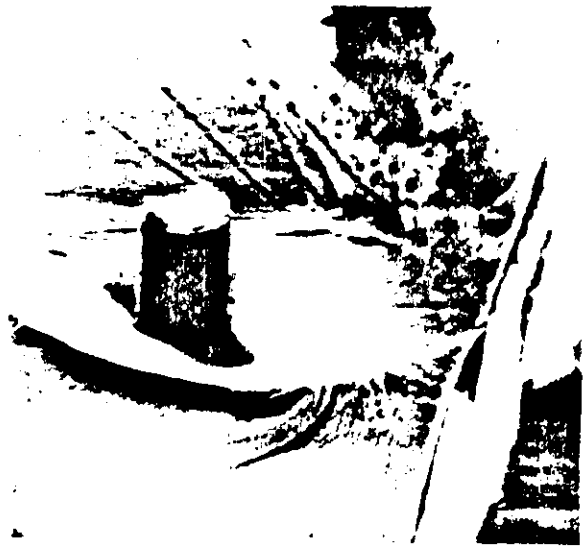

Figure 10.27. Scanning electron micrograph of a 10μm diameter fiber protruding through the inner surface of an indentation crack. Untreated E glass fiber/polyester resin composite exposed to boiling water for 400 hours [52].

inefficiency of joints

evolution of joint designs

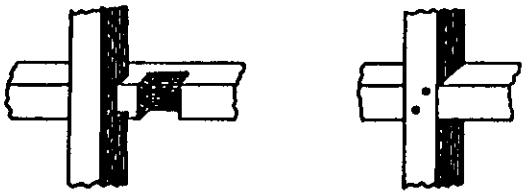

Figure 11.1. Halved and notched joint.

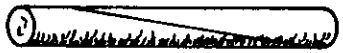

Figure 11.2. Scarfed joint.

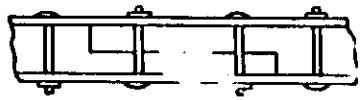

Figure 11.3. Lapped scarf joint.

Figure 11.4. Splayed scarf joint.

Figure 11.5. Tabled scarfing joints.

etal corrosion at joints involving carbon fiber composites

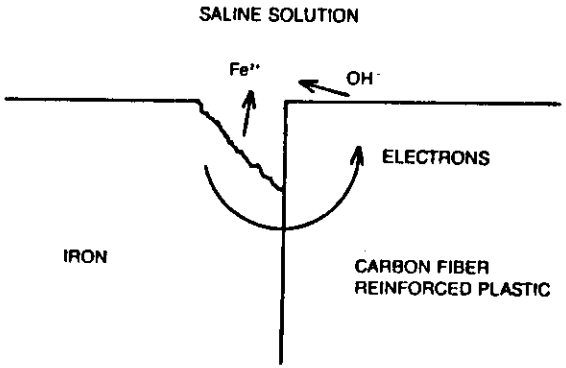

Figure 11.6. Galvanic corrosion between iron and carbon fiber reinforced plastic.

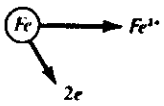

stress distribution in single lap joint

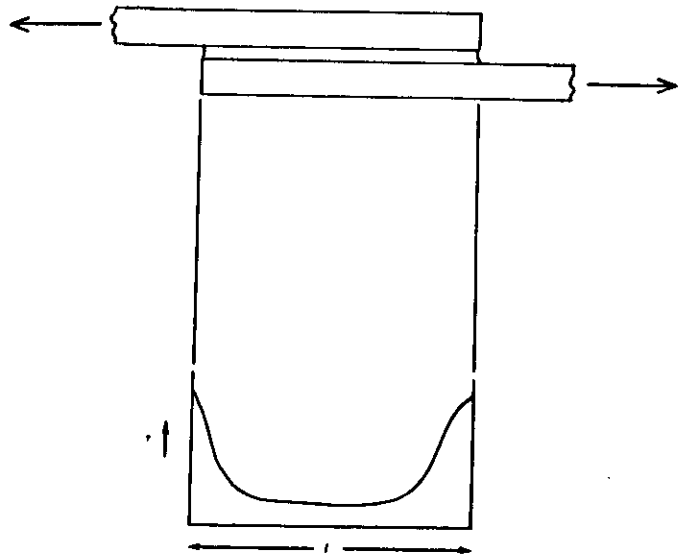

Figure 11.8. (a) Single lap joint. (b) distribution of mid-plane shear stress along the length l of (a).

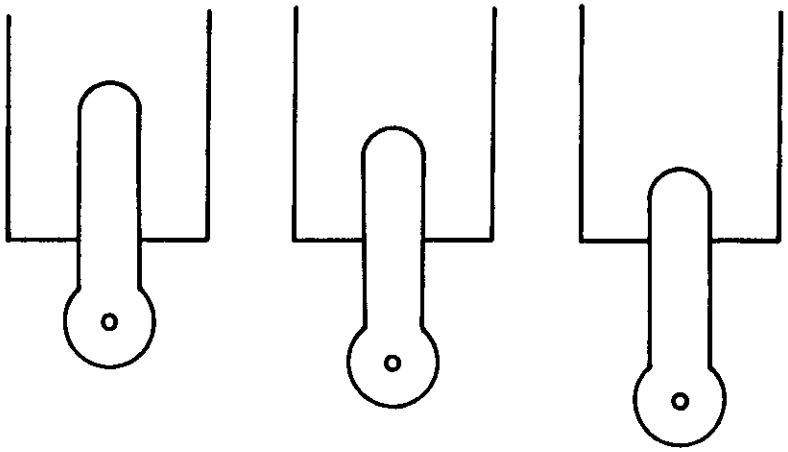

Figure 11.9. The strength of a bonded joint is independent of the depth of the bond. Each of these joints would fail at the same load.

peel strength

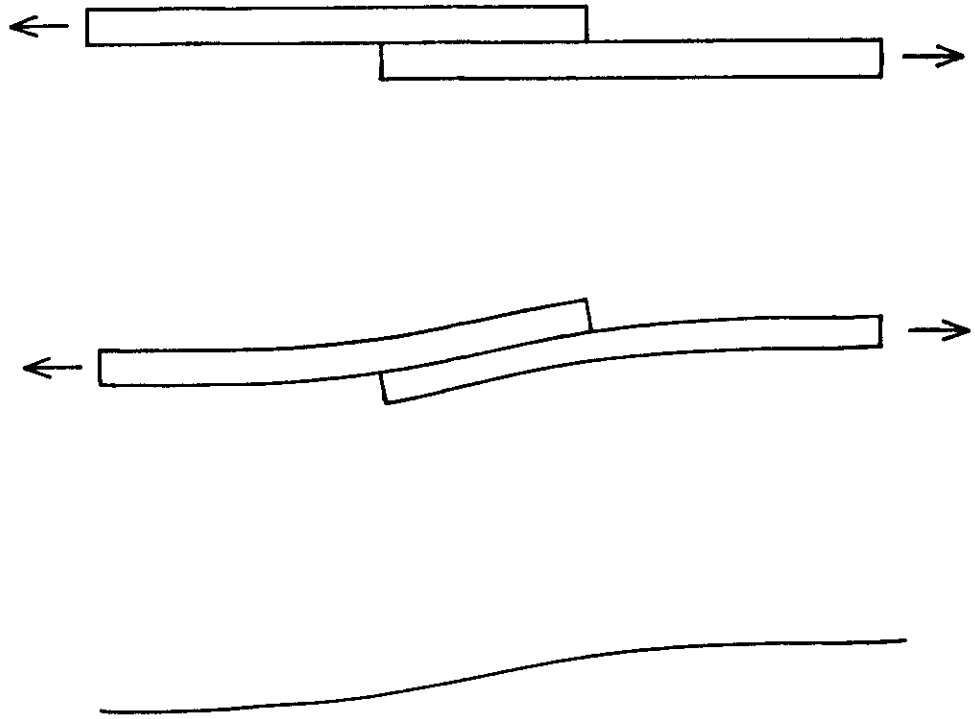

Figure 11.10. S-wise rotation in a tensioned single-lap bonded joint.

clamination below the bond-line

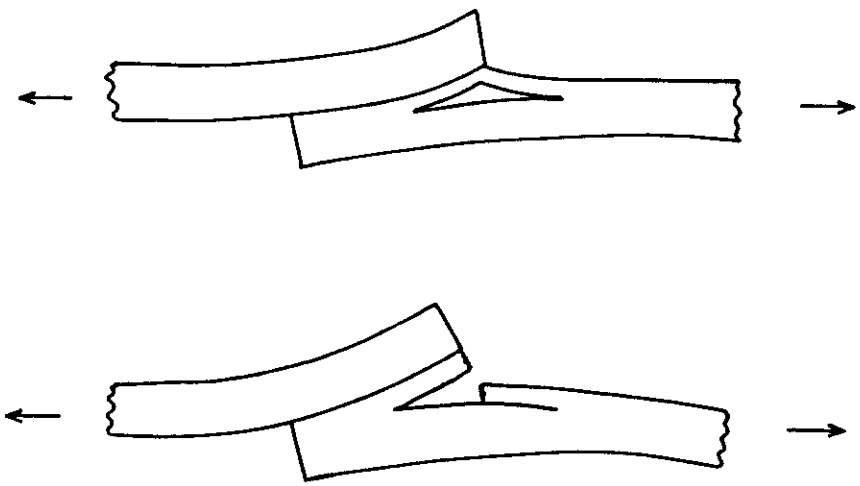

Figure 11.11. Illustrating localized delamination beneath one end of a lap joint.

inhomogeneous swelling associated with water uptake by adhesive joints

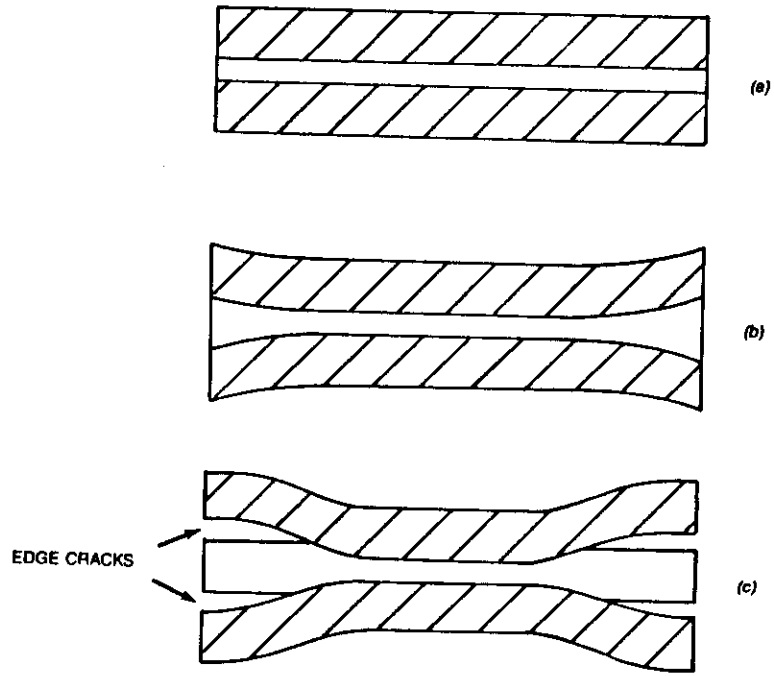

Figure 11.12. Formation of edge cracks due to inhomogeneous swelling of a butt joint.

internal stresses

van der Waals forces

Lennard-Jones potential

$$\phi(r) = 4\epsilon\left\{\left(\frac{\sigma}{r}\right)^{12} - \left(\frac{\sigma}{r}\right)^{6}\right\}$$

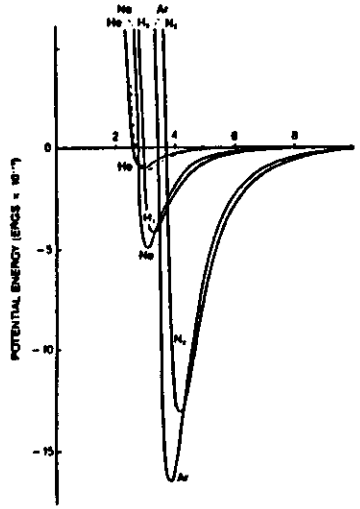

Figure 11.13. The potential energy of pairs of inert gas atoms as a function of their distance apart in Ångstroms (after Lennard-Jones [61]).

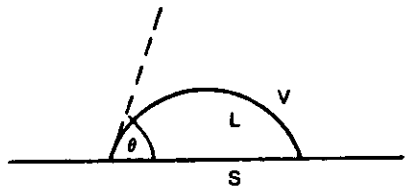

Figure 11.14.

Young's formula

$$\cos\theta = \frac{\gamma_{SV} - \gamma_{SL}}{\gamma_{LV}}$$

wetting phenomena

$$\gamma_{SV} - \gamma_{SL} < \gamma_{LV}$$

etc.

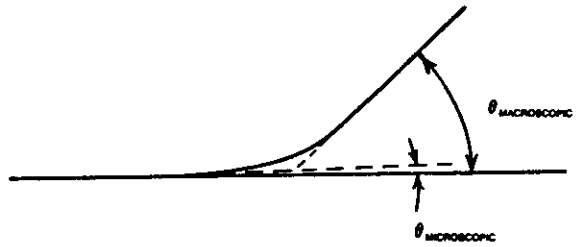

Figure 11.17. Near-field and far-field angles of contact.

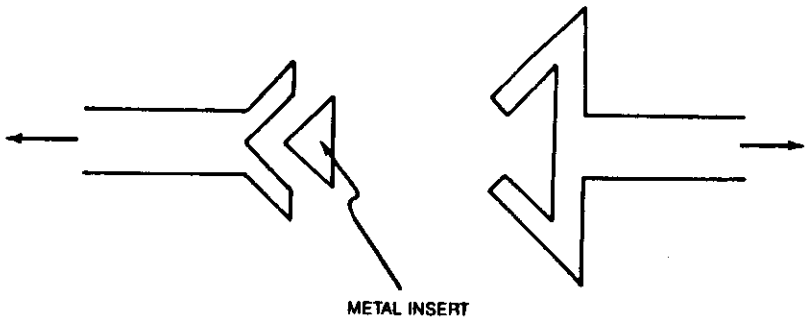

Figure 11.18a. Illustrating the use of metal inserts in joints.

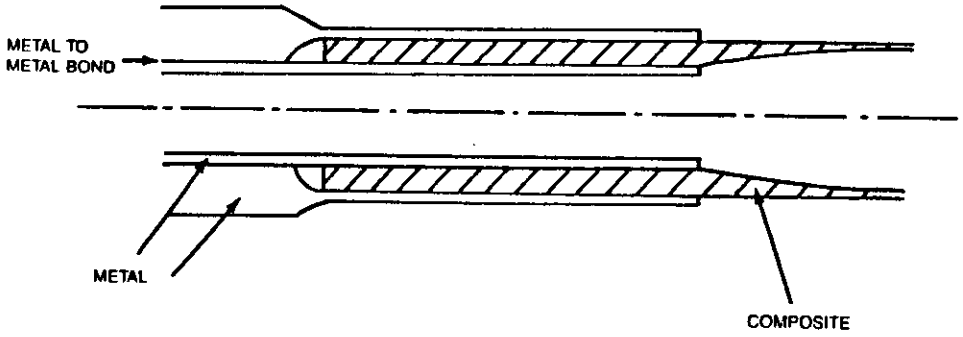

Figure 11.18b. Joint between a composite drive shaft and a metal differential.

encapsulation

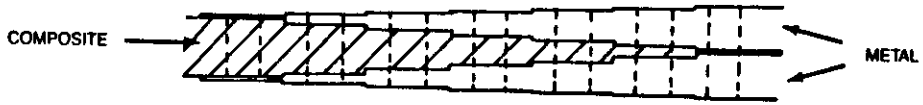

Figure 11.19. Stepped lap bonded/bolted joint.

Welding of metal matrix composites

Welding of thermoplastic matrix composites

Viscoelasticity

$$\sigma = c\epsilon + \eta\dot{\epsilon}$$

non-linear behavior

Mechanical tests

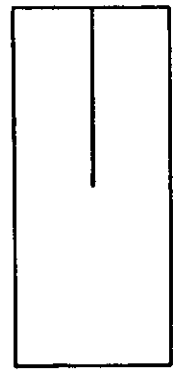

Figure 11.23. (a) Undeformed trouser test specimen.

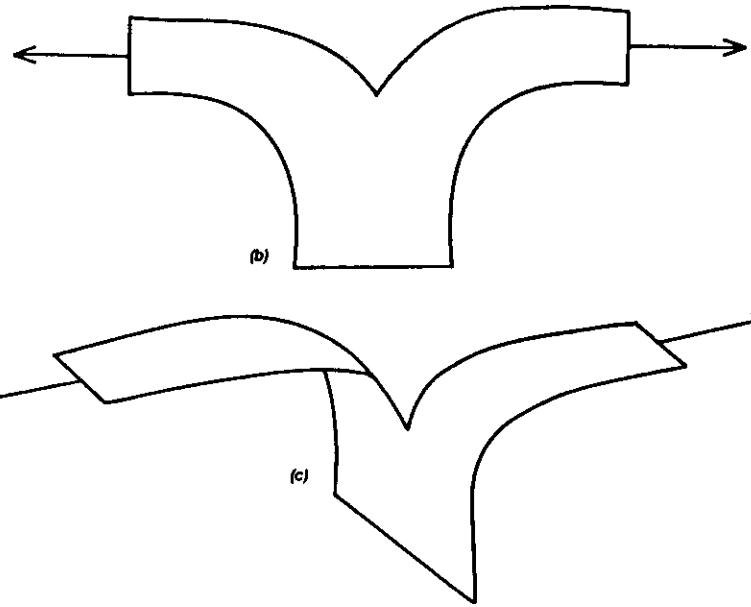

Figure 11.23. (b) and (c) Two different modes of applying tearing forces in the trouser test.

T-peel test

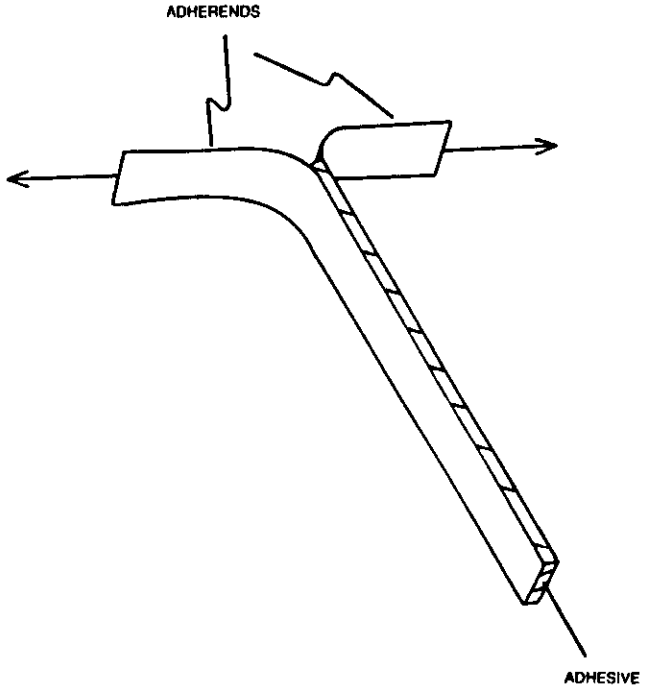

Figure 11.24. T-peel test.

Repair

cleaning of surfaces to be repaired

$$\frac{D_{\text{bnd}}}{D} = e^{-w/R}$$

physical differences between the repair and the rest of the structure

pre-cured patches

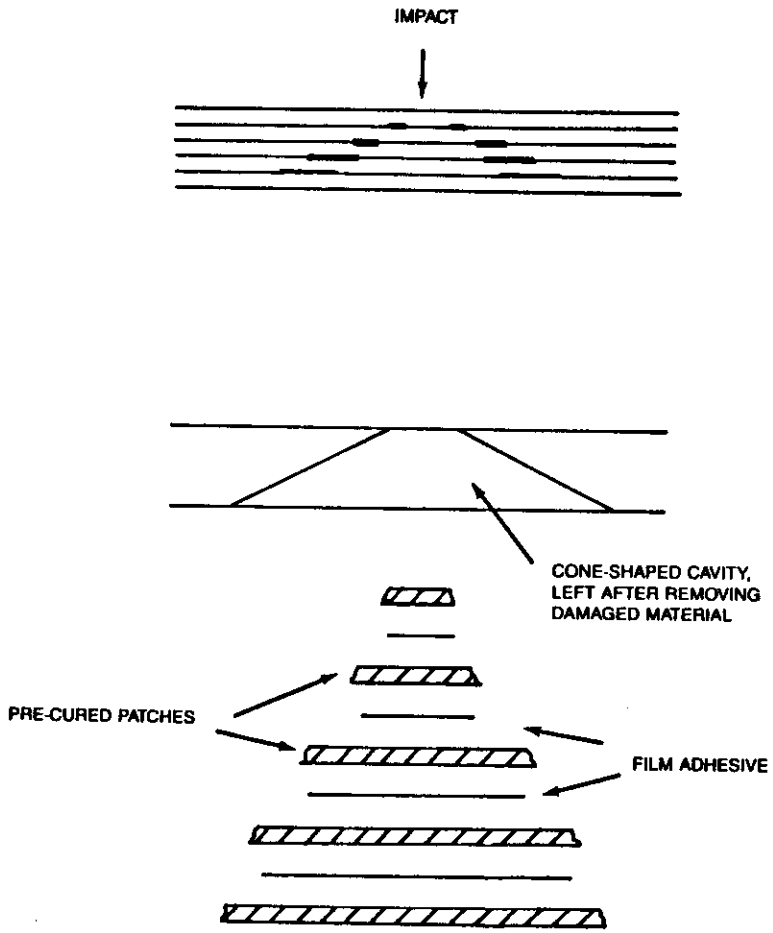

Figure 11.20. Application of adhesively bonded pre-cured laminate patches to replace the cone-shaped regions of damage produced by impact.

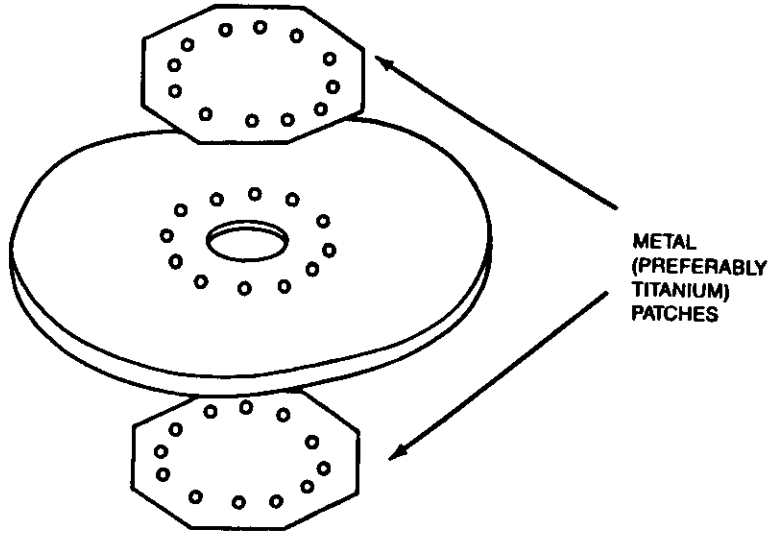

Figure 11.21. Metal patches to be riveted into position.

Visual inspection

Liquid penetrants

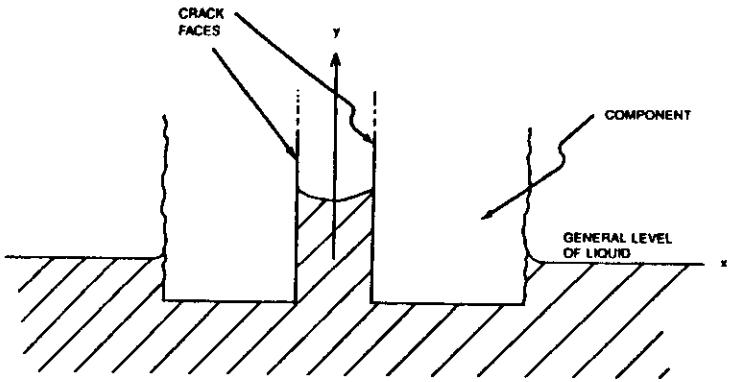

Figure 12.1. Component containing crack immersed in liquid penetrant.

$$y = \frac{2T}{x\varrho g} - \left(\frac{1}{2} - \frac{\pi}{8}\right)x$$

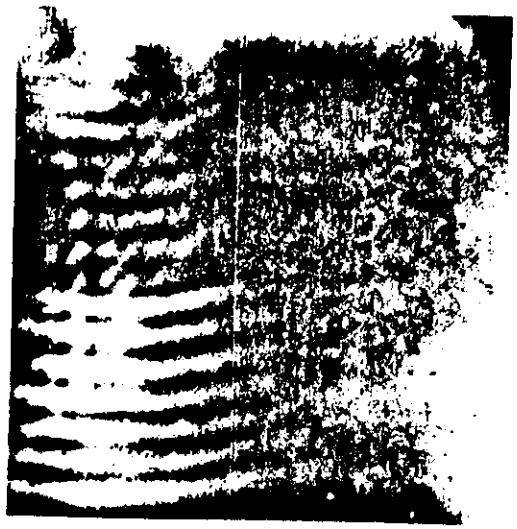

Figure 12.2. Photoelastic visualization of ultrasonic wavefronts in glass (courtesy of T. W. Turner).

V_s, V_p

pulse-echo

C-scan

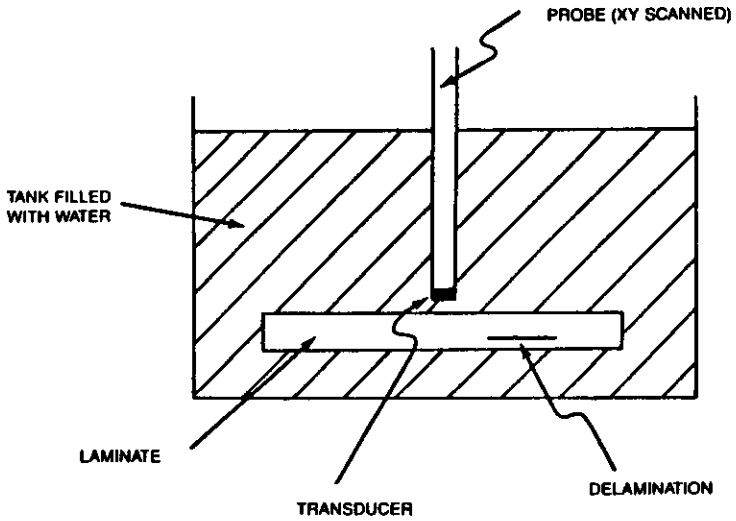

Figure 12.3. C-scan apparatus.

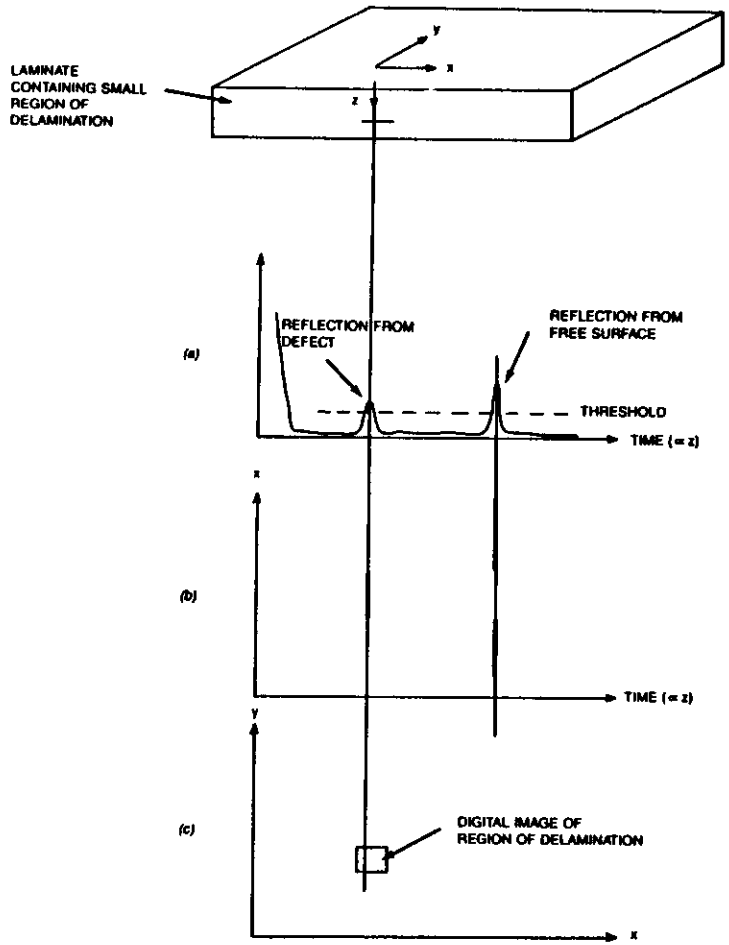

Figure 12.4. Showing the formation of (a) A-scan for which $x = y = 0$, (b) B-scan for which $y = 0$, and (c) C-scan for which $z = z_0 \pm \Delta z$.

attenuation of ultrasound

detection of cracks by velocity ratio measurement

$$\left(\frac{v_p}{v_s}\right)^2 = \frac{2(1-\nu)}{(1-2\nu)}$$

X-radiography, γ-radiography and neutron radiography

absorption coefficients

$$\frac{dI}{I} = -\mu dx$$

half-thickness

$$x_{1/2} = \frac{0.69}{\mu}$$

penetrant enhanced radiography

liquid crystals

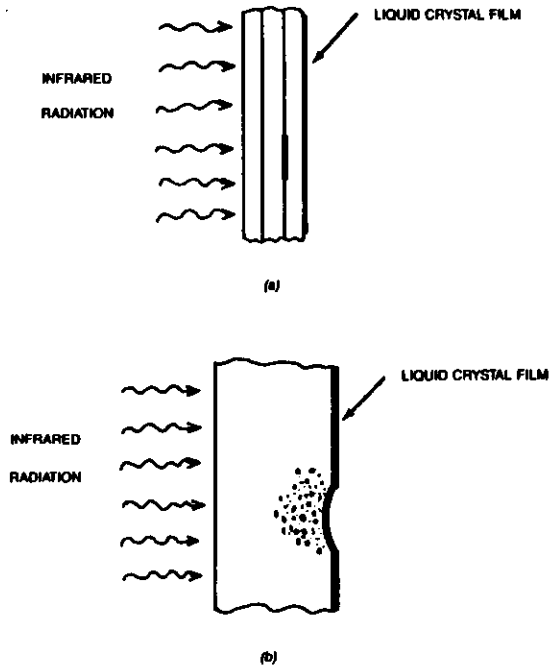

Figure 12.5. (a) and (b) Application of liquid crystal thermography to composite materials. The liquid crystal film has to be held in close proximity to the surface remote from the incident heat.

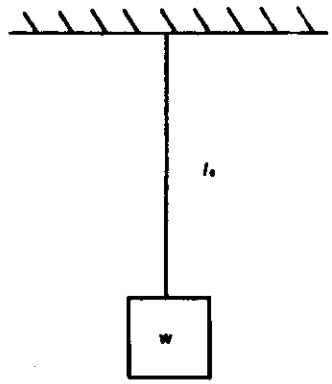

Figure 12.6. Illustrating adiabatic heating of a fiber.

$$\left(\frac{dT}{d\sigma}\right)_a = -\frac{\alpha T}{\varrho_0 c_p}$$

Fiber optics